

UNIVERSIDADE DE LISBOA
FACULDADE DE CIÊNCIAS
DEPARTAMENTO DE BIOLOGIA VEGETAL



**Remote sensing for water quality studies: test of
Suspended Particulate Matter and turbidity
algorithms for Portuguese transitional and inland
waters**

Giulia Sent

Mestrado em Ciências do Mar

Dissertação orientada por:
Doutora Carolina Garcia Vieira de Sá e Doutora Ana Inés Dogliotti

2020

ACKNOWLEDGMENTS

I would like to thank a number of friends, colleagues and institutions for different types of support without which the elaboration of this dissertation would not have been possible.

First of all, I am sincerely thankful to my advisors, Dr. Carolina Sá and Dr. Ana Dogliotti for their guidance, trust, valuable suggestions and all the scientific knowledge I have gained. Thank you for all the incredible opportunities that came up by working with you. You have been great contributors to my development, both personal and scientific, as well as of great inspiration.

I would like to thank the MARE Centre (Marine and Environmental Science Centre, ULisboa) where I have developed the majority of this dissertation. I am specifically thankful to Prof. Vanda Brotas, for the trust and for all the opportunities given. I am really grateful for all the enriching multidisciplinary experiences I had the chance to participate in. I also would like to sincerely thanks the teams of the different sampling programs (AQUASADO, GAMEFISH, NIPOGES, PLATAGUS, VALOR SUL) for the field work in the different study areas.

Also, a special thanks goes to all the people from the Marine Botany Laboratory team at MARE centre for the constant encouragement and support. Thank you for all the help with the laboratory and field work and sharing your expertise. A special thanks goes to Mara Gomes and Beatriz Biguino. The elaboration of this dissertation would have been much harder without your friendship, constant support and motivation.

A special thanks goes also to Dr. Juancho Gossn for the help with Python scripts and to the Platagus project team for the opportunities given. Thank you for all your valuable scientific knowledge, for the good mood and for the friendship.

I am also thankful to all the AMT29 team. Being in the middle of the ocean for 47 days surrounded by experienced scientists have been of great inspiration for my future career. Thank you for motivating me on keep working on my thesis onboard the RRS Discovery.

Also, a deep and sincere thanks goes to all my friends from the Portuguese climbing community. Thank you for making me fall in love with this beautiful country. I found a home 2400 km away from home.

To my flatmate Roberta, I would like to express a very special thanks. Thank you for your infinite support, for the laugh and the good food we share. Without you this path would have been much more complicated and boring.

Finally, the biggest thanks goes to my family. Thank you for understanding my need to leave my home country to enrich my life with new experiences. Without your support, all of this wouldn't have been possible.

This study was performed in the framework of different projects that are duly acknowledged:

Samplings in the Tagus estuary were performed in the framework of:

NIPOGES project, (MAR-01.03.02-FEAMP-0013) - Current status of the Manila clam populations of the Ria de Aveiro, Óbidos lagoon and the Tagus and Sado estuaries - scientific bases for a sustainable resource management. Funded by Programa Mar 2020.

Website: <https://ameijoajaponesa.com/projects/nipoges/>

Cofinanciado por:



PLATAGUS project – Water turbidity from space: satellite products validation for monitoring Río de la Plata and Tagus estuaries. A bilateral cooperation between Portugal and Argentina funded by Dirección Nacional de Cooperación e Integración Institucional (DNCEII) and Fundação para a Ciência e Tecnologia (FCT).

Website: <https://platagus.wordpress.com>



VALOR SUL - Programa de monitorização dos ecossistemas terrestre e estuarino na envolvente à CTRSU.

Website: n/a

Sampling in the Sado estuary was performed in the framework of AQUASADO Project (MAR - 02.01.01-FEAMP-0051) – Promoting sustainable aquaculture in the Sado estuary. Funded by Programa Mar2020.

Website: <https://aquasado.pt>



Cofinanciado por:



Sampling in inland waters was conducted in the framework of GAMEFISH Project (ALT20-03-0145-FEDER-000016) - Management of Mediterranean Reservoirs for the Promotion of Recreational Fishing Activities. Funded by the European Union - European Regional Development Fund, within the ALENTEJO 2020 Regional Operational Program.

Website: <http://www.gamefish.uevora.pt>

Cofinanciado por:



This work was also supported by PORTWIMS Project - Portugal Twinning for Innovation and Excellence in Marine Science and Earth Observation, Grant n° 810138 and CERTO Project - Copernicus evolution – Research activities in support of cross-cutting applications between Copernicus services, Grant n° 870349.



RESUMO

As partículas em Suspensão (SPM) é um dos principais constituintes da água nos estuários e, juntamente com a turbidez (T), é um parâmetro chave para a avaliação da qualidade da água. Através da absorção e difusão da luz, a concentração de SPM reduz a penetração da irradiância solar na coluna de água e limita a radiação fotossinteticamente disponível (PAR) para os produtores primários. Uma vez que a turbidez é altamente correlacionada com a concentração de SPM, para fins de monitorização da qualidade da água, a turbidez é listada como parâmetro obrigatório a ser medido pelos estados membros da União Europeia na Diretiva-Quadro Estratégia Marinha. Portanto, a quantificação destes dois parâmetros, a sua distribuição geográfica e o modo como se relacionam são de interesse crucial para o estudo dos ecossistemas, assim como para a investigação de diferentes processos, como transporte de sedimentos, produção primária e funcionamento de comunidades bentónicas.

A monitorização dos parâmetros da qualidade da água, é geralmente alcançado através de programas de amostragem *in situ*. No entanto, a realização regular de amostragens exige trabalho intensivo e é dispendioso. Além disso, é necessário assumir que as amostras analisadas, que estão limitadas em termos espaciais e temporais, são representativas da área total de interesse. Neste âmbito, a deteção remota da cor do oceano é uma ferramenta eficiente para monitorizar os parâmetros da qualidade da água. O crescente interesse em entender o potencial desta técnica é impulsionado pelos custos reduzidos e pela alta resolução espacial que permite obter resultados para grandes áreas, mas também pela grande frequência temporal dos dados. No entanto, a complexidade das águas costeiras, transitórias e interiores dificulta a deteção das variáveis de interesse devido à proximidade da terra e aos elevados níveis de reflectância causados pela alta concentração de SPM nas regiões espectrais do visível e infravermelho próximo. Não obstante, algoritmos têm vindo a ser desenvolvidos para estimar a concentração de SPM e turbidez, que são geralmente calibrados regionalmente para as características óticas dos diferentes locais.

Neste contexto, a presente dissertação teve como foco o teste de diferentes algoritmos com aplicabilidade global para estimar o SPM e a turbidez, bem como a avaliação de diferentes modelos de correção atmosférica. O principal objetivo deste trabalho foi determinar o esquema de processamento mais apropriado para quantificar o SPM e a turbidez em águas de transição e interiores em Portugal, determinando as incertezas associadas aos algoritmos de aplicabilidade global (Nechad et. al. (2009) para o SPM e Dogliotti et. al. (2015) para a turbidez) quando aplicados fora da sua região de calibração.

Para este fim, o estuário do Tejo e do Sado e cinco albufeiras na região do Alentejo em Portugal, foram utilizados como casos de estudo para testar o uso de imagens de satélite na monitorização da turbidez e SPM. A base de dados *in situ* foi adquirida no contexto de diferentes projetos (PLATAGUS, NIPOGES, Valor Sul, AQUASado, GAMEFISH) entre julho de 2017 e julho de 2019, dependendo do projeto. Os dados de satélite testados foram obtidos pelos Sentinel-2 *MultiSpectral Instrument* (S2-MSI) e o Sentinel-3 *Ocean and Land Colour Instrument* (S3-OLCI), missões do programa de Observação da Terra da Comissão Europeia - Copernicus.

No estuário do Tejo, as medições radiométricas *in situ* realizadas no contexto do projeto PLATAGUS permitiram também testar diretamente diferentes processadores para a correção atmosférica, nomeadamente o Acolite (S2-MSI), C2RCC (S2-MSI e S3-OLCI), L2 padrão MSI (Sen2Cor), L2 padrão OLCI (BAC / BPAC) e Polymer (S2-MSI e S3-OLCI). Tendo-se obtido melhores resultados com o Polymer e o C2RCC utilizando dados do S2-MSI, e resultados inconclusivos na avaliação dos dados com o S3-OLCI devido ao reduzido número de dados disponíveis.

Na avaliação dos algoritmos de SPM e turbidez, os resultados obtidos sugerem que o produto de turbidez é mais fácil de estimar com menores incertezas associadas. Em relação à estimativa do SPM através dos dados S2-MSI e S3-OLCI, as correlações e erros associados indicam que ainda há uma forte necessidade de desenvolvimento de novos algoritmos, com uma calibração regional específica para as características óticas das áreas de estudo ou para encontrar uma relação local entre SPM e turbidez, como já sugerido anteriormente na literatura. Além disso, o sensor S3-OLCI, que apresentou resultados satisfatórios para o estuário do Tejo, mostrou resultados discordantes para o estuário do Sado, sugerindo uma menor adequação da resolução espacial do OLCI (300 m) para estuários de menor dimensão.

No território português, as técnicas de deteção remota para monitorização da qualidade da água já estão em uso, mas têm sido testadas e aplicadas principalmente em águas costeiras. Este trabalho é um primeiro esforço para validar produtos de qualidade da água em águas de transição e interiores em Portugal. A importância destes ecossistemas, assim como o papel crucial da validação de produtos de deteção remota para monitorização ambiental e a principal motivação deste trabalho, e determinantes na definição das principais questões abordadas.

Palavras-chave: Qualidade da água, deteção remota, águas de transição, águas interiores, turbidez, SPM, Sentinel-2, Sentinel-3.

ABSTRACT

Suspended particulate matter (SPM) is one of the main water constituents in estuaries and along with turbidity (T), which is highly correlated with SPM concentration, are key parameters to evaluate water quality. Through light absorption and scattering, the SPM concentration reduces the penetration of solar irradiance within the water column and limits the photosynthetically available radiation (PAR) for primary producers making it a relevant indicator for water quality monitoring. In fact, regarding water quality monitoring, turbidity is listed as a mandatory parameter to be measured by EU member states in the Marine Strategy Framework Directive. Therefore, the quantification of these two parameters, their geographical distribution and their relationship are of crucial interest for ecosystems studies and to understand different processes such as sediment transport, primary production and the functioning of benthic communities.

Monitoring water quality parameters is usually achieved through field sampling programs. However, conducting regular field sampling is labor intensive and expensive and it is often necessary to assume that field samples, which are limited both spatially and temporally, are representative of the total area of interest. Satellite Ocean Colour Remote Sensing is an efficient tool to monitor these two parameters and the incrementing interest on understanding the potential of this technique is driven by the reduced costs and the high spatial and temporal resolution that allows obtaining results for large areas. However, remote sensing of coastal, transitional and inland waters is a complicated issue due to the proximity of the land and the high levels of reflectance caused by high SPM concentration in the visible and near infrared spectral regions. Many algorithms to retrieve SPM and T already exist and are often calibrated regionally for the optical characteristics of the different sites.

In this context, this thesis focuses on the test of different algorithms with global applicability for SPM and turbidity retrieval, as well as different atmospheric corrections. The main aim of the present work is to determine the most appropriate processing scheme to retrieve SPM and turbidity for Portuguese transitional and inland waters and to determine the accuracy of retrieval algorithms with global applicability (Nechad et. al, 2009 for SPM retrieval and Dogliotti et. al., 2015 for turbidity) outside their calibration region.

For this purpose, Tagus and Sado estuary, and five small water reservoirs in the Alentejo region in Portugal have been used as case-studies to test satellite imagery capability to monitor SPM and turbidity products. The *in situ* data for reference has been collected within the context of different projects (PLATAGUS, NIPOGES, Valor Sul, AQUASado, GAMEFISH) from July 2017 to July 2019 depending on the project. The satellite data used were obtained from the Sentinel-2 MultiSpectral Instrument (S2-MSI) and the Sentinel-3 Ocean and Land Colour Instrument.

(S3-OLCI), missions from the European Commission Earth Observation program, Copernicus.

In the Tagus estuary, *in situ* radiometric measurements conducted within the context of the PLATAGUS project allowed also to directly test different atmospheric corrections processors, namely (S2-MSI), C2RCC (S2-MSI and S3-OLCI), L2 standard MSI (Sen2Cor), L2 standard OLCI (BAC/BPAC) and Polymer (S2-MSI and S3-OLCI). Being Polymer and C2RCC the best performing algorithms for S2-MSI, while no definite results was found for S3-OLCI given the low number available data.

Results suggested that turbidity is easier to retrieve with smaller uncertainties associated. Regarding the SPM retrieval from S2-MSI and S3-OLCI data, the associated correlations and errors indicate that there is still a strong need of algorithms development perhaps with a regional calibration specific for the optical characteristics of the study areas or finding a local relationship between SPM and turbidity as has been previously suggested. Moreover, the S3-OLCI sensor, which gave satisfactory results for the Tagus estuary, showed discordant results for the Sado estuary suggesting a poor suitability of the OLCI spatial resolution (300m) for smaller estuaries.

In the Portuguese territory, remote sensing techniques have been tested and are in place for water quality monitoring mostly for coastal application. This work is a first effort to validate satellite-derived water quality products for monitoring transitional and inland waters in Portugal. The well-known importance of such ecosystems and the crucial role of satellite-data validation for reliable monitoring activities through remote sensing techniques drove the motivations and helped defining the main questions addressed in the present work.

Keywords: Water-quality, remote sensing, transitional waters, inland waters, turbidity, SPM, Sentinel-2, Sentinel-3.

INDEX

ACKNOWLEDGMENTS	II
RESUMO	V
ABSTRACT.....	VII
INDEX.....	IX
Tables index.....	XI
Figures Index	XIII
List of acronyms.....	XVI
Chapter 1: Introduction	1
1.1 Scope and objectives of the thesis.....	4
Chapter 2: Theoretical background.....	5
2.1 Ocean Colour remote sensing.....	5
2.2 OC sensors	7
2.2.1 Sentinel-2.....	8
2.2.2 Sentinel-3.....	9
2.3 SPM and turbidity from space	10
2.3.1 SPM and turbidity algorithms.....	10
Chapter 3: Study areas	15
3.1 Transitional waters (estuaries).....	15
3.1.1 TAGUS ESTUARY	15
3.1.2 SADO ESTUARY	16
3.2 Inland waters	17
Chapter 4: : Sampling and methods	20
4.1 In situ sampling.....	20
4.1.1 SPM and Organic Matter	21
4.1.2 Turbidity	22
4.1.3 Radiometric measurements	22
4.2 Remote sensing data (processors and algorithms).....	24
4.2.1 Atmospheric correction approach.....	24
4.2.2 Water quality algorithms approach.....	26
4.2.3 Statistics analysis	29
Chapter 5: Results	30
5.1 In situ measurements.....	30
5.1.1 SPM versus turbidity: sites variability.....	30
5.1.2 Radiometry	42
5.2 Remote sensing algorithms test	43
5.2.1 Atmospheric correction comparison	43
5.2.2 Water-quality algorithms comparison: SPM	45
5.2.3 Water-quality algorithms comparison: turbidity.....	53
Chapter 6: Discussion	62

6.1	In situ data	62
6.1.1	Suspended Particulate Matter and Turbidity	62
6.1.2	Radiometric measurements	65
6.2	Remote sensing algorithms evaluation	66
6.2.1	Atmospheric correction comparison	66
6.2.2	Water-quality algorithms test	67
6.2.3	Number of match-ups: limitations	71
Chapter 7:	Conclusions	73
	<i>References</i>	76
	<i>ANNEX A 1</i>	83
	<i>ANNEX A2</i>	85

Tables index

Table 2.1 - Current Earth-Observation satellite sensors, which may be used for inland and coastal water-quality studies	7
Table 2.2 - Spectral bands characteristics for the Sentinel-2 MSI sensor (ESA, 2015).....	8
Table 2.3 - OLCI bands characteristics. (ESA, OLCI User Guide).....	9
Table 2.4 - Examples of SPM and turbidity (T) existing algorithms.....	12
Table 3.1 - Main characteristics of the inland water bodies under study. (Adapted from: Almeida et. al., 2017) 19	19
Table 4.1 - Summary of data collected for the different study areas. Colors highlight the different projects sampling programs. Red cells indicate samplings performed within PLATAGUS project; dark blue correspond to NIPOGES project; green correspond to Valor Sul project; yellow correspond to AQUASADO project and light blue correspond to GAMEFISH project.	21
Table 4.2 - Summary of AC processors available for each sensor, S2-MSI and S3-OLCI.	25
Table 4.3 - Flags used from C2RCC and Polymer.....	26
Table 4.4 – A^λ (gm^{-3}), B^λ (gm^{-3}) and C^λ coefficients for the semi-analytical algorithms and the wavelengths under investigation. Coefficients for all the wavelength ranging between 500.00 to 885.00 nm are available in Nechad et al., 2009 and 2010.....	27
Table 4.5 - Wavelengths tested for the different algorithms.....	28
Table 5.1 - Summary of SPM and turbidity statistics for the three sections of the Tagus estuary.....	31
Table 5.2 - Summary of seasonal variation of SPM versus turbidity for the different areas of the estuary. For the outer stations only data corresponding to summer is available. The best R^2 and SPM:T ratio are highlighted in bold.....	32
Table 5.3 - Summary of SPM and turbidity statistics when taking into account tides and percentage in OM.	34
Table 5.4 - Summary of SPM and turbidity statistics for the three sections of the Sado estuary.....	36
Table 5.5 - Summary of seasonal variation on SPM versus turbidity for the different areas of the Sado estuary. The best R^2 and SPM:T ratio are highlighted in bold.....	37
Table 5.6 - Summary of SPM and turbidity statistics when considering tides and percentage in OM.....	39
Table 5.7 – Sampling period and in situ results of SPM (SPIM and SPOM) for the studied reservoirs.....	41
Table 5.8 - Summary of statistics of S2-MSI reflectance match-up analysis processed using different AC processors. Numbers in bold represent the best value for that statistics.....	44
Table 5.9 - Summary of statistics of S3-OLCI reflectance match-up analysis Rrs processed with C2RCC. Results from BPAC and Polymer didn't allow to perform any statistical analysis, therefore results are not presented....	45
Table 5.10 - Summary of statistics for SPM S2-MSI match-ups results for the Tagus estuary. Bolded number show the best value of each statistics for all processors.....	46
Table 5.11 - Summary of statistics for SPM S3-OLCI match-ups for the Tagus estuary. Numbers in bold show the best value of each statistics for all processors.....	48
Table 5.12 - Summary of statistics for SPM S2-MSI match-ups for the Sado estuary. Numbers in bold show the best value of each statistics for all processors.....	50
Table 5.13 - Summary of statistics for SPM S3-OLCI match-ups for the Sado estuary. Numbers in bold show the best value of each statistics for all processors.....	51
Table 5.14 - Summary of statistics for SPM S2-MSI match-ups for the inland waters. All the water bodies have been considered as a whole. Numbers in bold show the best value of each statistics for all processors.....	53
Table 5.15 - Summary of statistics for turbidity S2-MSI match-ups for the Tagus estuary. Numbers in bold show the best value of each statistics for all processors.....	55

Table 5.16 - Summary of statistics for turbidity S3-OLCI match-ups for the Tagus estuary. Numbers in bold show the best value of each statistics for all processors. 57

Table 5.17 - Summary of statistics for turbidity S2-MSI match-ups for the Sado estuary. Bolded numbers show the best value of each statistics for all processors. 59

Table 5.18 - Summary of statistics for turbidity S3-OLCI match-ups for the Sado estuary. Numbers in bold show the best value of each statistics for all processors. 61

Figures Index

Figure 2.1 - Pathways of light that reaches the sensors. (a) Light scattered by atmosphere. Multiple scattering is possible. It is also possible that some of the light that reaches the sensor is reflected at the sea surface before or after atmospheric scattering; (b) Specular reflection of direct sunlight at the sea surface; (c) Upwelling light leaving the water surface towards the direction of the satellite sensor. Adapted from (Sathyendranath, 1986). .6	
Figure 2.2 - Simplified schematic diagram of the forward and inverse models used in model based approaches (Matthews, 2011).....	14
Figure 3.1 - Estuarine waters study area. A) Tagus estuary and B) Sado estuary.....	15
Figure 3.2 - Tagus estuary bathymetry (MSL - Mean Sea Level). Data source: Rodrigues et al., 2017.	16
Figure 3.3 - Inland waters study area (source: Almeida et. Al., 2017). The location of each reservoir is indicated by a red star.....	17
Figure 4.1 - Sampling stations in the Tagus region (A) and Sado region (B). In figure A, the blue stations correspond to the Nipoges Project (SPM and turbidity), green to the Valor Sul project (SPM and turbidity) and red to the Platagus project (SPM, turbidity and radiometry). Sampling in Sado was conducted within the framework of AQUASado project.....	20
Figure 4.2 - Water sample filtering procedure.	21
Figure 4.3 - (A) Lovibond TB 210 NR and (B) HACH 2100Q portable turbidimeters.	22
Figure 4.4 - TriOS/RAMSES hyperspectral radiometers as installed on the pontoon rail.	23
Figure 4.5 - Processing chains applied to S2-MSI products (left) and S3-OLCI (right).	28
Figure 5.1 - Tagus estuary divided in three sections. “Inn” correspond to the upstream region, “mid” is middle region and “out” the downstream region. Stations highlighted in blue correspond to NIPOGES project, in green Valor Sul project and in red PLATAGUS project.	30
Figure 5.2 - Scatter plot of in situ SPM versus turbidity for the three sections of the estuary. The black dashed line shows the 1:1 relationship. The solid lines are the best linear fit to the data. The corresponding error statistics are shown in Table 5.1.....	31
Figure 5.3 - Scatterplot of the SPM:T variability over the seasons. The dashed black lines represent the 1:1 relationship. The solid lines show the best linear fit to the data in log space. The seasonal variation of the outer stations in not presented since it has been collected only in summer.....	32
Figure 5.4 - Scatterplots of SPM versus turbidity for the different tidal conditions (a, b) and percentage in organic matter (c, d). The dashed black lines show 1:1 relationship, the solid lines are the best linear fit to the data in log space.	33
Figure 5.5 - Organic and inorganic fractions obtained for each station. The level of inorganic matter reflects the tide level of the station, with higher values on low tide conditions (yellow background) and lower values with high tide (blue background).	34
Figure 5.6 - Sado estuary divided in three sections. “Inn” correspond to the upstream region, “mid” is middle region and “out” the downstream region.	35
Figure 5.7 - Scatter plot of in situ SPM versus turbidity for the three sections of the Sado estuary. The black dashed line shows the 1:1 relationship. The solid lines are the best linear fit to the data in log space. The corresponding error statistics are shown in Table 5.1.....	36
Figure 5.8 - Scatterplot of the SPM:T variability over the seasons for the Sado estuary. The dashed black lines represent the 1:1 relationship. The solid lines show the best linear fit to the data in log space.....	37
Figure 5.9 - Scatterplots of SPM versus turbidity for the different tidal conditions (A, B) and percentage in organic matter (C, D). The dashed black lines show 1:1 relationship, the solid lines are the best linear fit to the data in log space.	38
Figure 5.10 - Organic and inorganic fractions obtained for each station. The level of inorganic matter reflects the tide level of the station, with higher values on low tide conditions (yellow background) and lower values with high tide (blue background). The black dashed lines separate the sampling dates.	40

Figure 5.11. - Scatterplot representing the turbidity versus SPM for the inland waters. (a) shows the scatterplot when considering all the data available. In (b) only the Póvoa e Meadas reservoir (P1) has been considered. ... 42

Figure 5.12 - Average in situ water reflectance (R_{how}) for each sampling station. On the left (a) the stations collected during the first campaign (blue lines) and on the right (b) the second campaign (orange lines). In both plots, the intensity of the line color reflects the tidal conditions, with darker colors for samples collected during low tide (higher reflectance) and lighter colors for samples collected during high tide (lower reflectance). 42

Figure 5.13 - Atmospheric correction performance per sensor, S2-MSI (a) and S3_OLCI (b). Symbols are referred to the different wavelengths. Circles for 665nm (MSI and OLCI); triangles for 705nm (MSI) and 709nm (OLCI); squares for 740nm (MSI) and 754 (OLCI); pluses for 783nm (MSI) and 779nm (OLCI); stars for 865nm (MSI) and 620nm (OLCI). The black dashed lines represent the 1:1 relationship. 44

Figure 5.14 - Comparison of in situ and S2-MSI-derived SPM estimates at different wavelengths for the Tagus estuary in log space. Data represent match-ups for the concurrent satellite and field measurements collected during several research projects. The dashed black lines show 1:1 relationship, the solid lines are the best linear fit to the data in a log space. 45

Figure 5.15 - Comparison of in situ and S3-OLCI-derived SPM estimates at different wavelengths. Data represent match-ups for the concurrent satellite and field measurements collected during several research projects. The dashed black lines show 1:1 relationship, the solid lines are the best linear fit to the data in log space. 47

Figure 5.16 - Comparison of in situ and S2-MSI-derived SPM estimates at different wavelengths For the Sado estuary. The dashed black lines show the 1:1 relationship, the solid lines are the best linear fit to the data in log space. 49

Figure 5.17 - Comparison of in situ and S3-OLCI-derived SPM estimates at different wavelengths for the Sado estuary in log space. The dashed black lines show the 1:1 relationship, the solid lines are the best linear fit to the data in log space. 51

Figure 5.18 - Comparison of in situ and S2-MSI derived SPM at different wavelengths for inland waters. The black dashed lines show the 1:1 relationship. The solid lines represent the best fit to the data in log space. All the data available from the different reservoirs have been used. The corresponding error statistics are shown in Table 5.14. 52

Figure 5.19 - Comparison of in situ and S2-MSI derived turbidity at different wavelengths. The black dashed lines show the 1:1 relationship. The solid lines represent the best fit to the data in log space. The corresponding error statistics are shown in Table 5.15. 54

Figure 5.20 - Comparison of in situ and S3-OLCI-derived turbidity at different wavelengths. The dashed black lines show 1:1 relationship, the solid lines are the best linear fit to the data in log space. The corresponding error statistics are shown in Table 5.16. 56

Figure 5.21 - Comparison of in situ and S2-MSI-derived turbidity estimates at different wavelengths. Data represent match-ups for the concurrent satellite and field measurements collected during several research projects. The dashed black lines show 1:1 relationship, the solid lines represent the best linear fit to the data in log space. The corresponding error statistics are shown in Table 5.17. 58

Figure 5.22 - Comparison of in situ and S3-OLCI-derived turbidity estimates at different wavelengths. Data represent match-ups for the concurrent satellite and field measurements collected during several research projects. The dashed black lines show 1:1 relationship, the solid lines is the best linear fit to the data in log space. The corresponding error statistics are shown in Table 5.18. 60

Figure 6.1 - In situ SPM and turbidity spatial variability for the two estuaries under investigation (Tagus estuary on the left and Sado estuary on the right). Maps produced using the mean values of samples collected at similar tide conditions for each sampling point. 63

Figure 6.2 - In situ Suspended Organic Particulate Matter (SPOM) spatial variability for the two estuaries under investigation (Tagus estuary on the left and Sado estuary on the right). Maps produced using the mean values of samples collected at similar tide conditions for each sampling point. 63

Figure 6.3 - Boxplot representing the suspended organic percentages for each study area. 64

Figure 6.4 - OLCI-derived spectra corresponding to three different locations in the estuary. Inn (red dashed line) correspond to a pixel located in the inner basin, mid (yellow dashed line) is located in the middle region and out (blue dashed line) is located just outside the mouth of the estuary. Spectra derived from L2 S3A-OLCI image acquired on 31/08/2018, same day of in situ sampling. 66

Figure 6.5 – Examples of turbidity maps processed using Polymer AC and Nechad et. al. (2009) turbidity algorithm. (a) and (b) represent images processed from S2-MSI imagery (60m spatial resolution). (c) and (d) shows S3-OLCI processed images (300 m spatial resolution). On the left side (a and c) the Tagus estuary (both images sensed on the 31/08/2018 from S2A and S3A respectively). On the right side (b and d) the Sado estuary (both images sensed on the 15/05/2018 from S2B and S3A respectively). Purple color on images represent negative (invalid) values. 68

Figure 6.6 - Example of C2RCC processed SPM data: Sequence obtained for Póvoa e Meadas reservoir (P1). 69

Figure 6.7 - Percentage of sun-glint contaminated images over the Tagus estuary. Both Sentinel-2A and Sentinel-2B have been considered. 72

Figure 6.8 - Example of RGB S2-B image contaminated by a strong sun-glint. On the right, the Tagus estuary is completely covered by the reflection of sun which masks the water features. RGB image captured by S2-B satellite on the 28-05-2019. 72

List of acronyms

AC	Atmospheric Correction
AOP	Apparent Optical Properties
APA	Portuguese Environmental Agency
APD	Absolute Percentage Difference
BAC	Baseline Atmospheric Correction
BOA	Bottom-Of-Atmosphere
BPAC	Bright Pixel Atmospheric Correction
C2RCC	Case 2 Regional CoastColour
CDOM	Coloured Dissolved Organic Material
Chl-a	Chlorophyll-a
CZCS	Coastal Zone Colour Scanner
EO	Earth Observation
ESA	European Space Agency
EU	European Union
FNU	Formazin Nephelometric Unit
IOCCG	International Ocean Colour Coordination Group
IOP	Inherent Optical Properties
ISO	International Organization Standardization
MERIS	Medium Resolution Imaging Spectrometer
MSI	Multispectral Instrument
MWR	Microwave Radiometer
NIR	Near Infra-Red
NTU	Nephelometric Turbidity Units
OC	Ocean Colour
OLCI	Ocean Land Colour Instrument
OM	Organic Matter
OWT	Optical Water Types
PAR	Photosynthetically Available Radiation
RMSE	Root Mean Squared Error
RPD	Relative Percentage Difference
RRS	Remote Sensing reflectance
RTE	Radiative Transfer Equation
S2	Sentinel-2
S3	Sentinel-3
Sen2Cor	Sentinel 2 Correction
SNAP	Sentinel Application Platform
SNR	Signal-to-Noise Ratio
SPIM	Suspended Particulate Inorganic Matter
SPM	Suspended Particulate Matter
SPOM	Suspended Particulate Organic Matter
SRAL	SAR Radar Altimeter
T	Turbidity
TOA	Top-Of-Atmosphere
WFD	Water Framework Directive

Chapter 1: Introduction

The water quality from estuarine and inland waters has become an important matter for the society as about 50% of the worldwide population resides within 100 km from the coast and around 90% lives within 10 km from a freshwater body (UNEP, 2002, 2007; Wilson and Fischetti, 2010; Kummur *et al.*, 2011). The population growth, the expanding anthropogenic activities and the changing land-use practices, can all lead to a stress in the water quality in such sensitive environments (IOCCG, 2018). Therefore, a continuous monitoring of the water quality parameters is crucial for a sustainable use of the water bodies.

Monitoring water quality indicators and their consequent effects is usually achieved through field sampling programs. Although the high accuracy of the *in situ* measurements, it is often necessary to assume that the samples, which are limited both spatially and temporally, are representative of the total area of interest (Liu *et al.*, 2017). Moreover, conducting regular field samplings can be labour intensive, time consuming and expensive.

During the last decades, with the progress of technology and the advance in Space Sciences, new techniques for Earth Observation (EO) have been developed, which are resulting to be useful for monitoring water quality over water bodies.

The use of satellite remote sensing to monitor water bodies started in 1970s with the assumption that the colour of the water conveyed information on its water constituents, as it is determined by the electromagnetic interaction of light with the various components in the water (and the water itself) via absorption or scattering processes (Jerlov, 1968, 1975). This would allow oceanographers to remotely monitor the optical properties of water constituents, such as phytoplankton, coloured dissolved organic matter (CDOM) and Suspended Particulate Matter (SPM) (Ogashawara, Mishra and Gitelson, 2017), and to obtain a global perspective of its variability.

Satellite remote sensing offers many advantages over traditional monitoring methods, mainly because of the temporal and spatial consistency of the data.

Water quality indicators such as Chlorophyll-*a* (Chl-*a*), SPM, CDOM and turbidity can be estimated using remote sensing techniques because of their optical properties (references in Toming *et al.*, 2016). In the present study, we focused on SPM and turbidity.

SPM is used to describe the concentration of the total suspended matter in a water body. This parameter is the one generally required for sediment transport applications and along with turbidity are key parameters describing water quality. Through light absorption and scattering, the SPM concentration reduces the penetration of solar irradiance within the water column and limits the Photosynthetically Available Radiation (PAR) for primary producers (like phytoplankton cells).

Regarding water quality monitoring, turbidity is defined as the reduction of transparency of liquids caused by the presence of SPM (ISO 7027) and is listed as a mandatory parameter to be measured by EU member states in the Marine Strategy Framework Directive (European Union, 2008). The level of turbidity is highly dependent on the amount of particles suspended in a water body. The more particles are suspended in the water, the more difficult will be for the light to penetrate into the water column,

therefore the higher the water turbidity. Moreover, turbidity is a measure of scattering, which is directly related to the concentration of SPM (Bowers and Binding, 2006; Bukata *et al.*, 2018).

Therefore, the quantification of these two parameters and their geographical distribution, are essential for understanding processes such as sediment transport, deposition, resuspension, primary production and the functioning of benthic communities (Fettweis and Nechad, 2011).

Satellite remote sensing tools can provide efficient methods to monitor both parameters, however, some constraints need to be taken in consideration.

The first challenge is performing the atmospheric correction (AC), a crucial step when using remote sensing imagery as it removes the signal coming from the atmosphere from the total signal received by the satellite-sensor, allowing to isolate the signal coming from just below the water surface. The AC in such mutable and complex environments requires different approaches from the ones used for land and open ocean applications.

Moses *et al.*, 2017, indicated three main issues that make the AC challenging in optically complex waters: i) the proximity to terrestrial sources of atmospheric pollution may result in optically heterogeneous atmosphere which is difficult to model; ii) the adjacency effect which is the contamination of the signal received at the sensor by the contribution of the adjacent land pixels; iii) the non-negligible reflectance of water in the near infrared (NIR) region of the spectra due to high sediment concentrations preventing the use of the AC schemes adopted for open oceans.

Once the signal is retrieved, the complexity of the waters poses another challenge: to retrieve the different parameters contributing to the optical signal. A high range of optical variability can be found among water reservoirs and estuaries. These waters can be a mixture of optically shallow and optically deep waters, with different optically active compounds (*i.e.* phytoplankton, CDOM, SPM) interacting between them. Such aquatic systems can present short spatial and temporal gradients of clear to turbid waters as well as oligotrophic to hypertrophic productive waters. For example, an inland water body receives and recycles organic and inorganic substances from its watershed (Giardino *et al.*, 2019) and can be subject of accelerated eutrophication, proliferation of toxic-algae and extreme turbidity. This optical variability challenges the application of standard optical algorithms for water quality monitoring and therefore the validation of such products by performing comparisons with *in situ* data is a crucial step for reliable analysis.

Moreover, most of the algorithms for SPM and turbidity retrieval are often calibrated regionally for the optical characteristics of the different sites. Thus, the performance of such algorithms outside their calibration region is also a key question.

To address this question, semi-analytical models have been developed by Nechad *et al.*, (2009 and 2010) and Dogliotti *et al.*, (2015) with the aim to study whether a single algorithm to retrieve SPM or T from water reflectance can be applied globally, regardless the geographical region, particle size and composition, concentration, *etc.*

Semi-analytical algorithms to estimate SPM concentration directly from water reflectance are widely in use and they rely on the assumption that particulate backscatter is assumed proportional to SPM concentration via de constant b_{bp}^* (mass-specific backscattering of the particle) (Nechad, Ruddick and Park, 2010). However, the general hypothesis of such algorithms is that SPM varies within space and

time but not the mass-specific backscattering of the particles (b_{bp}^*). Hence, in most of the semi-analytical SPM retrieval algorithms, the b_{bp}^* parameter is considered constant.

However, different studies demonstrate the seasonal variability of such parameter in coastal, transitional and inland waters (Berthon *et al.*, 2007; Snyder *et al.*, 2008; Martinez-Vicente *et al.*, 2010; Nekermans *et al.*, 2012; Jafar-Sidik *et al.*, 2017) as well as the yearly cycle of the SPM: b_{bp}^* which is expected to be closely related to SPM:T ratio (Jafar-Sidik *et al.*, 2017). Jafar-Sidik *et al.*, (2017) showed that such ratio varied significantly through the seasons with results suggesting a direct effect of phytoplankton blooms on the SPM:T ratio, likely due to cells aggregation, and then a variability of SPM algorithms performance along the seasons. Because of this and since turbidity is in fact the parameter tightly related to backscattering (b_{bp}), Dogliotti *et al.*, (2015) suggest the use of a semi-analytical algorithm to retrieve turbidity from marine reflectance and only in a second step derive SPM from turbidity, where SPM:T regional and temporal variations can be taken into account.

Other algorithms for coastal remote sensing exist and they rely on a more complex inversion model and/or neural-networks approaches (Doerffer and Schiller, 2007). These models are used to retrieve SPM concentration in optically complex waters where the optical signal of SPM doesn't necessary co-vary with the Chl-*a* concentration (Kari *et al.*, 2017).

From the above-mentioned challenges it is easy to understand how crucial the validation procedure in ocean colour remote sensing in optically complex waters is. It is important to have quantitative evaluations and comparisons of the performance of different AC processors (IOCCG, 2010) and water parameters retrieval algorithms to derive water quality from remote sensing techniques with accuracy and known errors associated. In this specific work, it is also important to characterize and quantify the SPM:T ratio variability and consider it when testing SPM or turbidity retrievals through remote sensing techniques, particularly in such type of waters.

In the Portuguese territory, remote sensing techniques for water monitoring are already in use but it mostly concern coastal application (Cristina *et al.*, 2009; Goela *et al.*, 2013; Brito *et al.*, 2015; Sá *et al.*, 2015) and the Alqueva reservoir as inland water (Potes *et al.*, 2011, 2018; Potes, Costa and Salgado, 2011; Rodrigues *et al.*, 2020). To our knowledge, this work is a first effort of water quality products validation in transitional and inland waters in Portugal, specifically focused on SPM and turbidity. The well-known importance of such ecosystems and the crucial role of products validation for reliable monitoring activities through remote sensing techniques drove the motivations and helped drawing the main questions of the present work.

In this context, this thesis focuses on the test of different algorithms with global applicability for SPM and turbidity retrieval, as well as different atmospheric corrections, for Portuguese transitional and inland waters.

The two satellite sensors tested here were both developed by the European Space Agency (ESA) and are part of the European Commission (EC) Copernicus program: The Multispectral Instrument (MSI) mounted onboard Sentinel-2 satellites, and the Ocean and Land Colour Instrument (OLCI) onboard Sentinel-3.

1.1 Scope and objectives of the thesis

This work mainly focuses on satellite-based optical remote sensing. The main aim of this thesis is to evaluate the performance of different algorithms for SPM and turbidity by comparing *in situ* collected data with satellite-derived water products for Portuguese transitional waters (estuaries) and small inland water bodies.

A test of different global algorithms is performed in the Tagus and Sado estuaries and 5 small reservoirs in the Alentejo region. Over the Tagus estuary, *in situ* radiometric data allowed also the test of different atmospheric correction schemes.

To fulfil the above-mentioned aims, three specific objectives were defined:

- a) *In situ* characterization of the regions under investigation based on SPM and turbidity variability considering the main drivers of the SPM:T ratio variability;
- b) Evaluate different atmospheric correction processors over the Tagus estuary (*i.e.* Acolite, BPAC, C2RCC, Polymer, Sen2cor);
- c) Test of different algorithms for SPM and turbidity retrieval, specifically Nechad et. al. 2010, C2RCC-NN and L2 standard algorithms for SPM retrieval and Dogliotti et. al., 2015 and Nechad et. al., 2009 for turbidity retrieval.

In the next chapter, the principles of Ocean Colour remote sensing are given followed by a description of the satellite-sensors used for the present work and a state-of-the-art of the Ocean Colour algorithms for SPM and turbidity retrieval. Proceeding in the document, the study area and the methods used in this study are described in Chapter 3 and 4, respectively, followed by the presentation and discussion of the results (Chapter 5 and 6). Conclusions, which includes some considerations and future work, are presented in the final chapter, Chapter 7.

Chapter 2: Theoretical background

2.1 Ocean Colour remote sensing

Earth remote sensing is defined as the use of electromagnetic radiation to retrieve information about the oceans, land and atmosphere without being in contact with the parameter under investigation (Campbell & Wynne, 2011). By the assumption that the dissolved and particulate components of the water bodies interact with the light in the visible part of the spectrum via absorption or scattering processes, oceanographers started to remotely monitor the oceans with the launch of the first dedicated Ocean Colour (OC) sensor in 1978, the Coastal Zone Colour Scanner (CZCS). This proof-of-concept mission was the start of the OC satellites era.

Satellite remote sensing refers to the acquisition of information via satellite-mounted sensors that measure the intensity of radiation in a specific region of the electromagnetic spectrum. The sensors used for OC remote sensing are called passive sensors. This means that the light measured by the instrument is naturally emitted or reflected by the water body (*Ocean Optics Book*, 2015), as opposed to the active sensors which emit a signal of known characteristics.

The functioning of passive sensors relies on the principle that the sunlight, when enters a water body, changes its spectral character and amplitude depending on the absorption and scattering properties of the optical components dissolved in the water. The altered sunlight, carrying information of the water constituents, is reflected out of the water and can be detected by the sensor onboard a satellite.

Based on this principle, the distribution and concentration of oceanic substances that are optically active such as phytoplankton, SPM and CDOM can be detected from space. By knowing how the different optically active components alter the light, it could be possible to deduce which components are present in the water and their concentration.

The optical information of the water bodies is contained in the water-leaving radiance, L_w , but it is also dependent on the incident sunlight that has reached the water and the downwelling irradiance, E_d , at the surface. In order to retrieve this information, the optical sensors mounted on satellites record those photons that have reached the water surface after travelling through the atmosphere, that interacted with the components dissolved in the water body and were finally backscattered through the atmosphere and reached the satellite sensor (Figure 2.1) (Beltrán-Abaunza, 2015). However, 90% of the signal that arrives at the sensor is due to the atmospheric interaction with the light and must be removed through Atmospheric Correction (AC) in order to retrieve the signal related to the water substance.

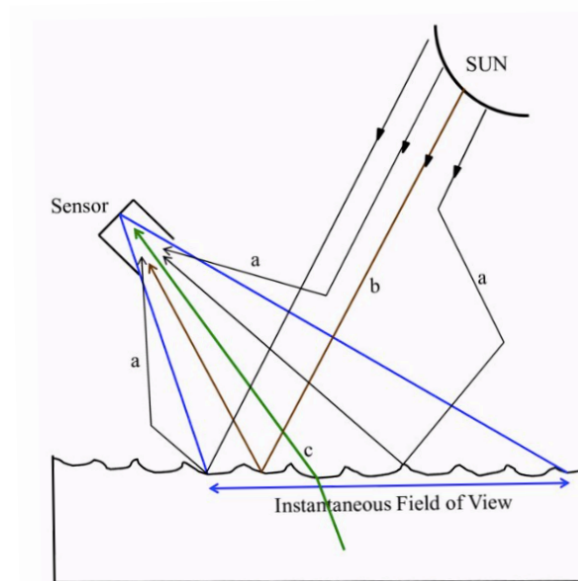


Figure 2.1 - Pathways of light that reaches the sensors. (a) Light scattered by atmosphere. Multiple scattering is possible. It is also possible that some of the light that reaches the sensor is reflected at the sea surface before or after atmospheric scattering; (b) Specular reflection of direct sunlight at the sea surface; (c) Upwelling light leaving the water surface towards the direction of the satellite sensor. Adapted from (Sathyendranath, 1986).

Absorption and scattering are Inherent Optical Properties (IOPs) of optically active substances such as phytoplankton, SPM and CDOM. Since these properties are not affected by the distribution of the light field but are just dependent on the concentration, type and morphology of the substances, a key objective of OC remote sensing is the estimation of the IOPs to retrieve the concentration of the substances of interest. However, the optical properties that are directly measured by the sensors, *i.e.* the reflectance at a specific wavelength, are Apparent Optical Properties (AOPs), which depend not only on the IOPs but also on the light distribution, *i.e.* L_w and E_d . Through the use of algorithms (see section 2.3) it is possible to convert the AOPs into IOPs and the associated water parameters of interest. In this context, for sensors such as OLCI mounted onboard the Sentinel-3 satellites, that are specifically designed for ocean colour remote sensing, the concentration of different substances such as SPM, Chl-*a* or IOPs are available as standard products. Nevertheless, sensors that were not specifically designed for water monitoring purposes such as Sentinel-2 MSI have been shown to be useful for this scope by applying algorithms that allows to retrieve water constituents (*e.g.* Pahlevan *et al.*, 2017).

In oceanic waters, where the optical properties are dominated by phytoplankton and associated materials, also known as optical Case 1 waters (Morel and Prieur, 1977), there is already a wide range of successful remote sensing applications. This is mainly because in the open ocean there are few substances that affect the optical signal coming from the water surface. However, remote sensing applications for coastal and inland waters still remains a challenge. In fact, in this type of waters (also called optical Case 2 waters), a wide array of substances such as suspended sediment and/or yellow substances play a major role in the optical properties that turn the development of algorithms a more complicated matter.

This complex interactions in the coastal areas can lead to a large optical variability with consequent uncertainties in the application of remote sensing models. Furthermore, progress in these optically complex waters has been hampered by the complications in atmospheric correction because of the proximity of the land that can lead to uncertainties on such algorithms (Hu, Carder and Muller-Karger,

2000). A good knowledge of the optical properties is therefore crucial for the development and application of algorithms for the retrieval of water constituents.

2.2 OC sensors

Different Earth-Observation satellite sensors specifically designed for Ocean Colour studies may be used for water quality assessments of coastal and inland waters (Table 2.1). Understanding the characteristics of the various sensors is important in order to choose the most appropriate instrument for the objectives of the study. Differences in the spectral, spatial and temporal resolutions are the main features that characterize the different sensors.

The spatial resolution describes how much detail is visible to the human eye in a photographic image. The spatial resolution of images acquired by satellite sensors is usually expressed in meters and it is the equivalent width of a pixel. The higher the spatial resolution, the more details will be visible in the image. In coastal and inland waters studies, where the study area is often defined by a small region, the spatial resolution is an important criterion to take into account when choosing the sensor to use for the study.

The temporal resolution refers to the time interval that the sensor takes to revisit the same spot on Earth. For the same sensor, the revisit time may change with the latitude, having shorter revisit time at higher latitudes and longer revisit time at the equator.

The various sensors may also differ in spectral resolution. This consists in the number and width of the spectral bands of a sensor. This characteristic of the sensors is what makes them specifically designed for the different purposes, *i.e.* Ocean Colour sensors have a spectral resolution optimized for the retrieval of biological features in water. However, other satellites not specifically developed for water studies such as Sentinel-2 from ESA, can also be useful to monitor small water areas as coastal and inland waters.

Table 2.1 - Current Earth-Observation satellite sensors, which may be used for inland and coastal water-quality studies

Satellite	Sensor	Spectral resolution	Spatial resolution	Temporal resolution
<i>Proba-1</i>	CHRIS	415-1050 nm (19 bands)	18 m	~7 days
<i>Landsat-7</i>	ETM+	450-2345 nm (8 bands)	30 m	16 days
<i>Landsat-8</i>	OLI	435-1384 nm (9 bands)	30m	16 days
<i>Terra/Aqua</i>	MODIS	620-876 nm (2 bands)	250 m	1-2 days
<i>Sentinel 3</i>	OLCI	413-1020 nm (16 bands)	300 m	1-2 days
<i>Sentinel 2</i>	MSI	443-1020 nm (13 bands)	10, 20, 60 m	5 days
<i>GCOM-C</i>	SGLI	375-1250 nm (19 bands)	250 m	-

Considering the above-mentioned criteria, two different satellites were chosen for the present study. Sentinel-2 and Sentinel-3 are constellations of satellites developed by ESA within the EC - Copernicus Earth Observation program. The motivation behind the choice of these two satellites was driven by the potential of the applicability of its sensors for coastal and inland water studies. Sentinel-3 carries a dedicated ocean colour sensor, OLCI, with a medium spatial resolution (300 m) and an almost daily revisit time. On the other hand, the Sentinel-2 has a spatial resolution of 10 m, 20 m, 60 m depending on the band, that makes it particularly useful in monitoring even small inland water bodies, despite the main application of the MSI sensor onboard this satellite is land monitoring.

Each Sentinel mission is based on a constellation of two satellites orbiting 180° apart to optimize the revisit time, that results in 5 days at medium and low latitudes for the Sentinel-2 (however at higher latitudes is every second day because of the overlapping orbits) and almost every day for the Sentinel-

3. These missions carry technologies such as multi-spectral imaging instruments for land, ocean and atmospheric monitoring.

2.2.1 *Sentinel-2*

The main application of the Sentinel-2 mission is land-monitoring, but some of the bands of the MSI onboard Sentinel-2 have shown to be also useful for monitoring coastal and inland waters.

The imagery has bands with 10 m, 20 m and 60 m spatial resolution, where the 60 m bands are used for the atmospheric correction, which makes this sensor a useful tool for monitoring small estuaries or inland water bodies. Data are acquired in 13 spectral bands (Table 2.2) and radiometric resolution of the sensor is 12-bit (ESA, 2015). Sentinel-2A was launched on 23 June 2015 and Sentinel-2B followed on 7 March 2017.

Table 2.2 - Spectral bands characteristics for the Sentinel-2 MSI sensor (ESA, 2015).

Band number	Central wavelength (nm)	Bandwidth (nm)	Spatial resolution (m)
1	443	20	60
2	490	65	10
3	560	35	10
4	665	30	10
5	705	15	20
6	740	15	20
7	783	20	20
8	842	115	10
8a	865	20	20
9	945	20	60
10	1380	30	60
11	1610	90	20
12	2190	180	20

Data products

Products are a compilation of elementary granules of fixed size, along with a single orbit. A granule is the minimum indivisible partition of a product containing all possible spectral bands (ESA, 2015), and the Sentinel-2 data products available for users are listed as follows:

- Level 1C products are composed of 100 km² tiles. Per-pixel radiometric measurements are provided as Top Of Atmosphere (TOA) reflectance with all parameters to transform them into radiances.
- Level 2 products provide Bottom Of Atmosphere (BOA) reflectance images derived from the associated Level-1C products. Therefore, each Level-2A product is also composed of 100 km² tiles in cartographic geometry. Level-2A with standard ESA processing can be downloaded and alternative processing can be performed by the user through the Sentinel-2 Toolbox (SNAP software) using as input the associated L1C product.

2.2.2 *Sentinel-3*

Sentinel-3 is a multi-instrument mission aiming to measure sea-surface topography, sea- and land-surface temperature, ocean colour, and land colour with high accuracy and reliability. It carries four main instruments, OLCI, previously mentioned, SLSTR (Sea and Land Surface Temperature Instrument), SRAL (SAR Radar Altimeter) and MWR (Microwave Radiometer). OLCI has 21 spectral bands (400 – 1200 nm) with a swath width of 1270 km and a spatial resolution of 300 m (Table 2.3).

Table 2.3 - OLCI bands characteristics. (ESA, OLCI User Guide).

Band number	Central wavelength (nm)	Bandwidth (nm)	Function
<i>Oa01</i>	400	15	Aerosol correction, improved water constituent retrieval
<i>Oa02</i>	412.5	10	Yellow substances and detrietal pigments (turbidity)
<i>Oa03</i>	442.5	10	Chlorophyll absorption maximum, biogeochemistry, vegetation
<i>Oa04</i>	490	10	High Chlorophyll
<i>Oa05</i>	510	10	Chlorophyll, sediments, turbidity, red tides
<i>Oa06</i>	560	10	Chlorophyll minimum
<i>Oa07</i>	620	10	Sediment loading
<i>Oa08</i>	665	10	Chlorophyll (2 nd Chlorophyll absorption maximum), sediment, yellow substances, vegetation
<i>Oa09</i>	673.75	7.5	For improved fluorescence retrieval
<i>Oa10</i>	681.25	7.5	Chlorophyll fluorescence peak, red edge
<i>Oa11</i>	708.75	10	Chlorophyll fluorescence baseline, red edge transition
<i>Oa12</i>	753.75	7.5	O2 absorption/clouds, vegetation
<i>Oa13</i>	761.25	2.5	O2 absorption band, aerosol correction
<i>Oa14</i>	764.375	3.75	Atmospheric correction
<i>Oa15</i>	767.5	2.5	O2A used for cloud top pressure, fluorescence over land
<i>Oa16</i>	779.75	15	Atmospheric correction/Aerosol correction
<i>Oa17</i>	865	29	Atmospheric correction/Aerosol correction, clouds, pixel co-registration
<i>Oa18</i>	885	10	Water vapor absorption reference band
<i>Oa19</i>	900	10	Water vapor absorption, vegetation monitoring (maximum reflectance)
<i>Oa20</i>	940	20	Water vapor absorption, atmospheric correction/Aerosol correction
<i>Oa21</i>	1020	40	Atmospheric correction/aerosol correction

Data products

The OLCI products that are distributed to users are divided into three main types (ESA & EUMETSAT, 2018) :

- Level-1B products, which are output from the OLCI Level-1 processing. The Level-1 product provides TOA reflectance for each pixel in the instrument grid, each view and each OLCI channel, plus annotation data associated to OLCI pixels. It can be obtained at full resolution of 300 m (OL_1_EFR) or reduced resolution of 1200 m (OL_1_ERR).
- Level-2 land products, output from the OLCI Level-2 processing. The level-2 land product provides land and atmospheric geophysical parameters computed for full and reduced resolution.
- Level-2 water products, output from the OLCI Level-2 processing. The Level-2 water product provides water and atmospheric geophysical parameters computed for full and reduced resolution.

2.3 SPM and turbidity from space

Remote sensing techniques have been widely used to estimate SPM and turbidity and to study their spatial and temporal variation. As it has already been mentioned in Chapter 1, the level of turbidity is highly dependent on the number of particles suspended in a water body. The more particles are suspended in the water, the more difficult will be for the light to penetrate into the water column, therefore the higher the water turbidity. Suspended sediments are responsible for most of the scattering, whereas the organic particles (*e.g.* phytoplankton) and coloured dissolved matter (CDOM) controls most of the absorption of the light in the water bodies (Myint and Walker, 2002).

In remote sensing studies, SPM is estimated via the optical properties of suspended particles, assuming a constant relationship between particle mass and particulate scattering or absorption. It is well-known that this relationship between particle mass and optical properties, in reality varies as a function of particle size and composition (refractive index) (Babin *et al.*, 2003), giving an important limit on the generality and accuracy of remote sensing algorithms for estimating SPM (Ruddick *et al.*, 2008). The literature for SPM remote sensing is quite developed but it mostly concerns oceanic waters and often the sensors used have low spatial resolution which is unsuitable for transitional and inland waters. Moreover, remote sensing in Case 2 waters is a complicated matter because of the interaction between the constituents and the proximity of the land that can lead to uncertainties in the atmospheric correction and the development of algorithms to retrieve the water parameters.

Therefore, it is necessary to choose an appropriate sensor for the objectives of the study, as well as the atmospheric correction and water parameter retrieval algorithms.

In the next sections of this chapter the satellite sensors used for the present study are described, and a state-of-the-art of the ocean colour algorithms for SPM and turbidity retrieval are given.

2.3.1 SPM and turbidity algorithms

As we already discussed before, remote sensing in Case 2 waters is a complicated matter because of the interaction between the constituents and the proximity of the land that can lead to uncertainties in the

atmospheric correction and the development of algorithms to retrieve the water parameters. Furthermore, in order to provide an evaluation of the overall reliability of remote sensing retrieved data, an *in situ* validation is fundamental to establish the uncertainty which should be associated with the estimated values.

In transitional waters where the dynamic and variation of SPM and turbidity is driven by semidiurnal tides, as is the case of the Portuguese estuaries under investigation in the present study, the remote sensing validation can be particularly challenging. In fact, in these water bodies the SPM and turbidity varies rapidly with the tide, leading to more turbid waters during low tide, and clear and organic materials-enriched waters during high tide. Since the satellites passages over the same site intercept different tidal conditions, which corresponds to different Optical Water Types (OWT), this can lead to big uncertainties in the algorithms performance.

In order to retrieve quantitative information about a water quality parameter, after removing the effects of the atmosphere, the application of appropriate algorithms is required. In this scope, many algorithms for the retrieval of water constituents already exist and they can be divided in different classes when compared, but their general operation is driven by variations in the spectral shape and/or magnitude of the water leaving radiance signal in response to the water quality parameter of interest (IOCCG, 2018).

Different nomenclatures may be applied to classify existing algorithms and approaches. Two types of classification commonly used can be distinguished considering the number of bands used or the method used for the development of the algorithm. The empirical approaches and model-based (analytical) approaches are the two major groups of algorithms (IOCCG, 2000) and are briefly described in the following sections.

Considering the number of bands used, algorithms for quantification of SPM and turbidity from water leaving reflectance fall roughly into one of three families (Ruddick *et al.*, 2008): single band, band ratio or multispectral.

Many algorithms have been developed to estimate SPM from reflectance at a single band. For low and moderate reflectance the detection of SPM is related to the almost linear relationship between SPM and reflectance at any given wavelength (Althuis and Shimwell, 1995), while at higher reflectance this relationship becomes non-linear. That is why the performance of single band algorithms is generally best for low to moderate levels of reflectance. The requirement of low to moderate reflectance suggests that the optimal wavelength will depend on concentration and fixed wavelength algorithms will typically be limited to a certain range of concentrations. The suitability of single band algorithms for SPM estimation means that SPM mapping can be made not just with dedicated ocean colour sensors such as OLCI but also with a very wide range of optical remote sensors (*e.g.* Sentinel-2). However, single band algorithms are highly sensitive to backscatter and can be subject of uncertainties if the mass-specific backscatter coefficient has high natural variability (Ruddick *et al.*, 2008). A type of algorithms that is less sensitive to this natural variability are the band-ratio algorithms since these effects are largely cancelled when a ratio is taken.

With Ocean Colour Sensors many more bands are available, and the use of this extra information can improve algorithm performance. Such algorithms are called multispectral and are generally based on a forward model (see Section 2.2.2, Fig. 2.1), defining reflectance as a function of IOPs and an inversion procedure to find the model reflectance spectrum that best fits the measured reflectance (Ruddick *et al.*, 2008).

Turbidity data are by far the most frequent data set related to SPM provided to the scientific community and managers of the coastal environment. For this reason, and as turbidity is tightly related to backscattering, Dogliotti *et al.*, 2015 suggested making use of a semi-analytical relation to estimate turbidity from marine reflectance and, in a second step, derive SPM from turbidity. Because of the strong correlation between SPM and turbidity, many of the considerations of SPM algorithm design apply equally to turbidity algorithms with the simplification that the last one is not affected by variation of the mass density of particulate material (Nechad *et al.*, 2009). Studies specifically on remote sensing of turbidity are less numerous compared with SPM studies.

In the Table 2.4 some examples of algorithms are given.

Table 2.4 - Examples of SPM and turbidity (T) existing algorithms.

Case of studies	Algorithms type	Bands used	Derived property	SPM/T Range
<i>Binding, et al., 2003</i>	Empirical	Single-band	SPM	1-24 mgL ⁻¹
<i>Dogliotti et al., 2015</i>	Semi-analytical	Single-band	T	1.8-988 FNU
<i>Eleveld et al., 2008</i>	Analytical	Single-band	SPM	-
<i>Gohin et al., 2005</i>	Semi-analytical	Single-band	SPM	1.0-25 mgL ⁻¹
<i>Han et al., 2016</i>	Semi-analytical	-	SPM	0.15-2626 mgL ⁻¹
<i>Nechad et al., 2009</i>	Semi-analytical	Single-band	T	0.59-83.63 FNU
<i>Nechad et al., 2010</i>	Semi-analytical	Single-band	SPM	1.24-110.27 mgL ⁻¹

The choice of approach, or combination of approaches, depends largely on the level of optical complexity of the waters under consideration, the optically-active constituent concentration ranges, the spectral characteristics of the sensor to which they will be applied, the amount of information available regarding inherent optical properties, and computation time/resources (IOCCG, 2018).

Empirical algorithms

The empirical and semi-empirical approaches are distinguished from the bio-optical model-based approaches by directly relating the remote-sensed signal to the parameter of interest using statistical techniques (IOCCG, 2000). All empirical algorithms establish a relationship between the optical measurements and the concentration of constituents based on *in situ* data, *i.e.*, water leaving reflectance (or radiance) and coincident *in situ* concentrations measurements.

The formulae used in empirical approaches are based on a combination of reflectance, or remote sensing reflectance R_{rs} , at different wavelengths, which will provide the best correlation between reflectance data and the concentration of the optically active water parameter.

The most common relationship makes use of the colour ratio as described by Equation 2.1 (IOCCG, 2000):

Equation 2.1:

$$p = \alpha \left(\frac{R_1}{R_2} \right)^\beta + \gamma,$$

where p is the physical quantity to be estimated, and R_i is the reflectance at the spectral channel i . The coefficients are derived from regressions between the radiance ratios and the desired property and are based on experimental data sets.

These types of models typically use statistical techniques (Ogashawara, Mishra and Gitelson, 2017) to extract the best relationship between R_{rs} and constituent concentration. The selection of spectral bands does not follow any physical or optical principles of the IOPs and AOPs.

Semi-empirical models, on the contrary, are based on specific spectral features of absorption and scattering of the constituents governing reflectance.

The relatively low accuracy usually found in Case 2 waters conditions using this type of algorithms, can be improved by using different bands to cover a wider range of variability. The advantages of empirically-derived algorithms are that they are simple, easy to derive even from a limited number of measurements, and easy to implement and test. They have a short computing time due to their mathematical simplicity and they yield stable results. By their very nature, empirical algorithms for Case 2 waters are always regional in scope and might not always work if natural variability is not included in the calibration dataset.

Model-based approaches (Analytical)

The model-based approaches (or analytical), aim to model the remote sensing reflectance R_{rs} in terms of the water IOPs through radiative transfer¹ modelling. The ‘forward’ model (Figure 2.2) derives R_{rs} from the water IOPs using a bio-optical model and an approximation of the radiative transfer equation (RTE) or through direct solution of the RTE, while the ‘inverse’ model solves the IOPs from reflectance measured at the top of the atmosphere by satellites or from *in situ* measurements of R_{rs} . The inversion problem may be solved using any of a variety of mathematical optimization or multiple non-linear regression procedures, such as artificial neural networks, to produce analytical or inversion algorithms (IOCCG 2000, 2006).

¹ The radiative transfer is the physical phenomenon of energy transmission through electromagnetic radiation.

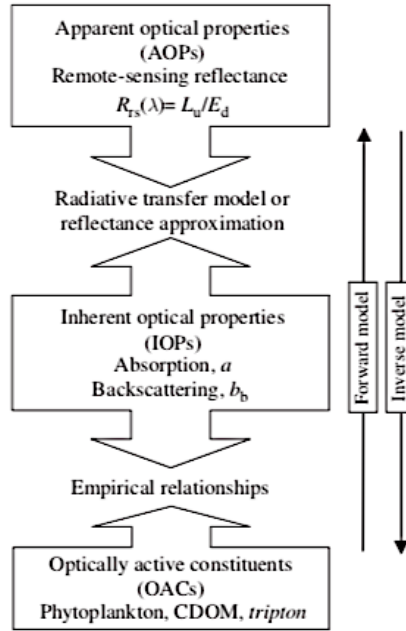


Figure 2.2 - Simplified schematic diagram of the forward and inverse models used in model based approaches (Matthews, 2011).

The analytical approach is generally complex and ideally requires measurements and knowledge of local/regional IOPs to develop a robust forward model. This often requires substantial fieldwork and algorithm training and computing time (Matthews, 2011).

Closely related to analytical models, are the semi-analytical and quasi-analytical approaches. These models rely on the inversion of the RTEs to establish relationships among AOPs and IOPs, which is computed through several analytical and empirical steps. Inverse models use AOPs, such as reflectance (Equation 2.2), to derive IOPs (Gordon, Brown and Jacobs, 1975):

Equation 2.2:

$$Rrs(\lambda) = \frac{L_u(0^-, \lambda)}{E_d(0^-, \lambda)} = g_1 \left(\frac{b_b(\lambda)}{a(\lambda) + b_b(\lambda)} \right) + g_2 \left(\frac{b_b(\lambda)}{a(\lambda) + b_b(\lambda)} \right)^2,$$

where: $Rrs(\lambda)$ is the remote sensing reflectance, $a(\lambda)$ is the total spectral absorption coefficient, $b_b(\lambda)$ is the total spectral backscattering coefficient, $L_u(0^-, \lambda)$ and $E_d(0^-, \lambda)$ are upwelling radiance and downwelling irradiance, respectively, g_1 and g_2 are geometrical factors (Ogashawara, Mishra and Gitelson, 2017). The outputs from semi-analytical and quasi-analytical models, estimated IOPs, are validated using IOPs derived from water samples via analytical methods.

Chapter 3: Study areas

The study areas analysed in this study can be divided into estuarine or transitional and inland waters. The estuarine waters consist in two estuaries in the central coast of Portugal (Figure 3.1): The Tagus and the Sado estuaries, described in the following section.

As a case study for inland waters, 5 small reservoirs in the Alentejo region in Portugal (Figure 3.3) have been chosen within the context of the GAMEFISH project - *Gestão e promoção da Pesca Recreativa em Albufeiras da Região Mediterrânica*. General characterization of the reservoirs is provided in section 3.2.

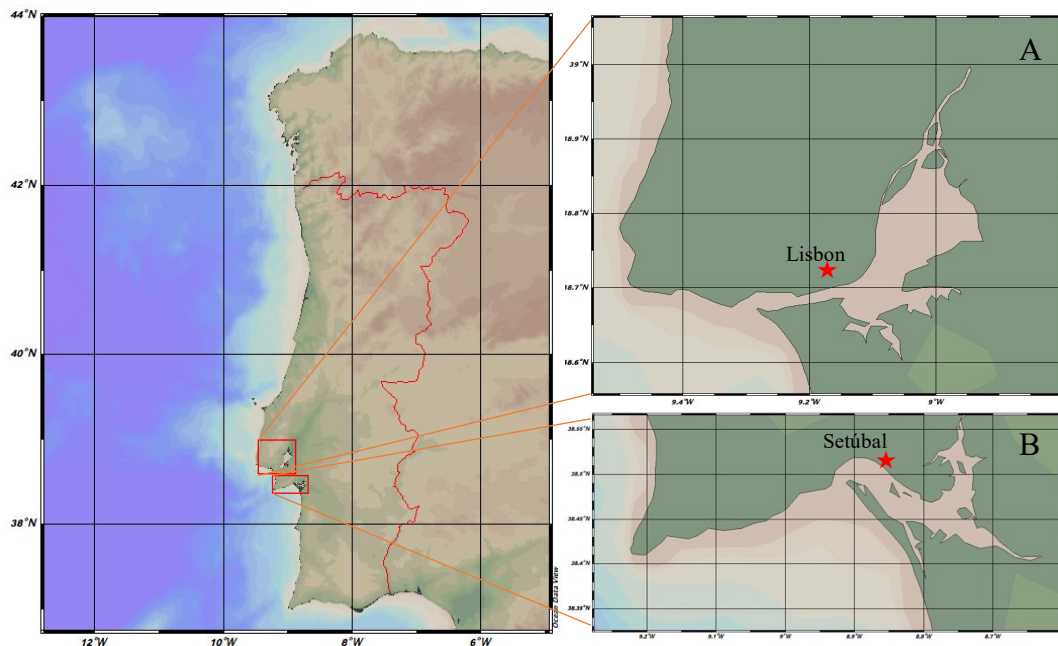


Figure 3.1 - Estuarine waters study area. A) Tagus estuary and B) Sado estuary. Maps produced with ODV (version 5.2.1).

3.1 Transitional waters (estuaries)

3.1.1 TAGUS ESTUARY

The estuary of the Tagus river (Figure 3.1A) is the largest wetland in Portugal and one of the main estuaries in Europe with an area of about 320 km² (APA, 2016). In the context of the European Water Framework Directive (WFD) (European Commission, 2003), it is classified as a transitional water of the typology A2 – mesotidal well-mixed estuary with irregular river discharge (Bettencourt *et al.*, 2003).

The morphology of the Tagus estuary is characterized by a deep, long and narrow inlet that connects the Atlantic Ocean to the interior of the estuary, which consists in a shallow basin that has extensive tidal flats and marshes.

Morphologically, the Tagus estuary can be divided into three regions (Rodrigues *et al.*, 2017): i) the upstream region, characterized by low depths (average depth of 2 m); ii) the middle section, with an average depth of 7 m; and iii) the downstream section, which represents the main navigation channel and can reach depths of 40-50 m. The estuary width varies between about 500 m, in the upstream section, and 15 km, in the inner bay. The bathymetry of the estuary is presented in Figure 3.2.

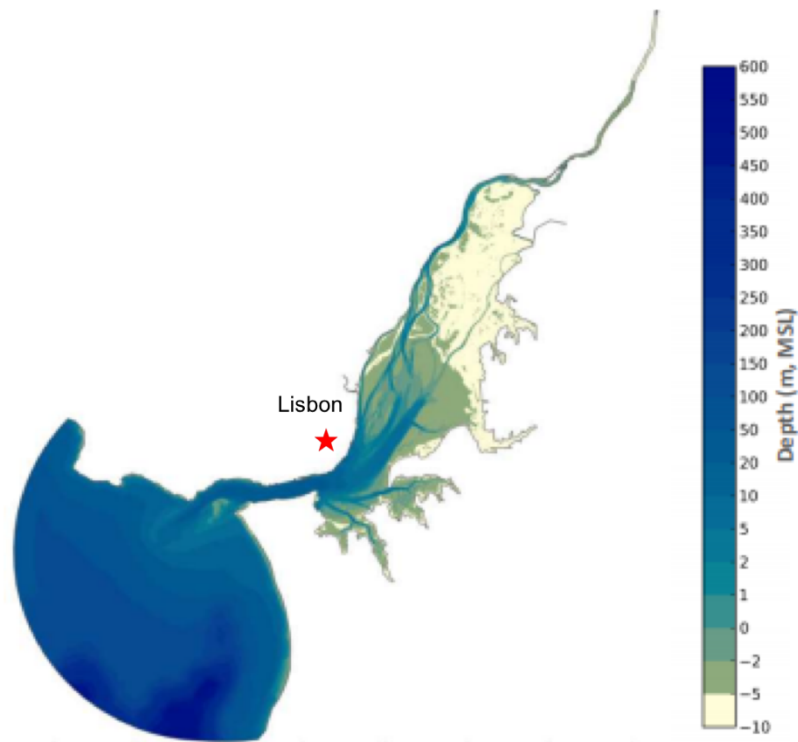


Figure 3.2 - Tagus estuary bathymetry (MSL - Mean Sea Level). Data source: Rodrigues *et al.*, 2017.

The drainage in the Tagus Estuary is primarily forced by the tides (semidiurnal, as in the whole Portuguese coast), but the circulation is also influenced by the river flow, wind, atmospheric pressure and surface waves. The maximum tidal speeds are registered at the mouth of the estuary, with values around 2 m/s, decreasing towards the interior of the estuary (APA, 2016).

River discharge may significantly influence water levels, but only farther than 40 km upstream of the mouth (Vargas *et al.*, 2008). Downstream, the water levels are mainly controlled by tides and storm surges. The Tagus river is the main affluent of the Tagus estuary. The mean river discharge is $336 \text{ m}^3 \text{ s}^{-1}$ (APA, 2012). Other characteristic discharge values are: maximum (10 days/year), $828 \text{ m}^3 \text{ s}^{-1}$; median (180 days/year), $239 \text{ m}^3 \text{ s}^{-1}$; minimum (355 days/year), $102 \text{ m}^3 \text{ s}^{-1}$. Two other rivers contribute significantly to the water inflow to the estuary: the Sorraia and the Trancão Rivers.

Different studies (*e.g.* Martins & Duffiner, 1982; Silva *et al.*, 1986; Valença *et al.*, 2011) showed that salinity presents seasonal patterns and spatial gradient, varying between 1.0 – 37.0 (Gameiro, Cartaxana, & Brotas, 2007), both dependent on the combined role of the river flow and tide. Water temperature also presents a seasonal variation, varying between 8 – 26 °C (Gameiro *et al.*, 2007), with the higher temperatures occurring during summer, as expected (Rodrigues *et al.*, 2017).

3.1.2 SADO ESTUARY

The Sado estuary (Figure 3.1B), located in the Setúbal peninsula, is one of the most important wetlands in Portugal being part of an important natural reserve (Arrábida Natural Park) and being the second largest estuary in the country with an area of approximately 240 km^2 (Caeiro, 2004).

As the estuary of the Tagus river, the Sado estuary is also classified as a transitional water of the typology A2 – mesotidal well-mixed estuary (Ferreira *et al.*, 2005) in the context of the WFD.

The Sado estuary is characterized by a complex morphology and can be divided into two main regions: i) the lower estuary, the Setubal Bay, 5 km wide and 20 km long with complex topography and an average depth of 10 m; and the ii) upper estuary, composed by two main channels: the Alcácer channel (35 km long and 700 m wide, with an average depth of 5 m and about 80% of the total freshwater inflow) and the Marateca channel on the North side (about 10% of the total freshwater inflow). The two channels are partially separated through intertidal sandbanks (Caeiro, 2004).

The connection to the ocean is made through a deep and narrow channel (maximal depth of 50 m) located between the Tróia peninsula and the right margin of the estuary.

The low average depth, strong tidal currents, and low freshwater discharge make the Sado estuary a well-mixed, mesotidal estuary.

The annual river discharge is approximately $40 \text{ m}^3 \text{ s}^{-1}$ with high season variability (OSPAR, 2002), varying from $1 \text{ m}^3 \text{ s}^{-1}$ in summer to $60 \text{ m}^3 \text{ s}^{-1}$ in winter and showing large interannual fluctuations. The circulation is mainly tidally driven (Martins et al., 2001) by a semi-diurnal tide with an average spring tidal range of 2.7 m. The residence time of the water, in each part of the estuary, is of the order of one week, resulting into strong mixing between the zones of the estuary, with deposition and mineralization of the particulate organic matter in the shallow intertidal areas (OSPAR, 2002).

The primary production is limited by nutrients and by the interaction between phytoplankton and zooplankton. The highest values of Chl-*a* concentration are found in the upstream zone, Alcácer channel, where nutrient availability is higher (OSPAR, 2002).

3.2 Inland waters

The selection of the reservoirs used in this work has been made during the first task of the GAMEFISH project (Almeida *et al.*, 2017). The study area includes 5 reservoirs (Table 3.1) in three hydrographical regions (*i.e.* the hydrographical basins of Tagus river, Sado river, and Guadiana river), Figure 3.3.

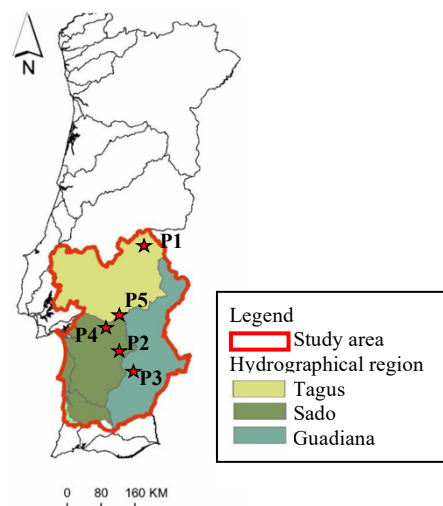


Figure 3.3 - Inland waters study area (source: Almeida *et. Al.*, 2017). The location of each reservoir is indicated by a red star.




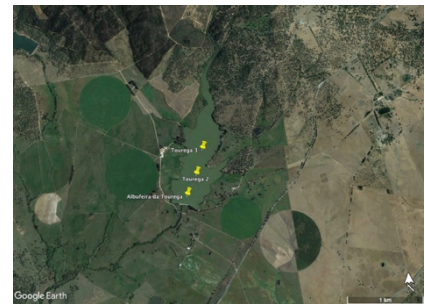

In terms of climate, the region is characterized by a temperate (mesothermic) climate, with a rainy winter and a dry summer associated with the months of July and August. Rainy months occur during the autumn-winter period and lead to a drastic increase in river flow, which contrasts with the driest two

months where precipitation is almost zero and there is a marked reduction in the flow of water. Consequently, a high intra-annual flow variability is observed, where during the summer period a minimum percentage of the annual flow occurs (Almeida *et al.*, 2017). Considering a North – South orientation, an increase of annual average temperatures and a decrease of annual average precipitation is observed.

In addition to their importance as water supply, the present lentic water bodies are preferred places for sport or professional fishing, thus operating as a valuable socio-economic and cultural resource. However, during the dry period these ecosystems undergo drastic variations related to the reduction of water volume (high water level fluctuation) and nutrient increase, which consequently result in increased primary productivity, eutrophication, oxygen depletion and alteration of their biological communities (Navarro *et al.*, 2009).

The characteristics of each reservoir are described in Table 3.1.

Table 3.1 - Main characteristics of the inland water bodies under study. (Adapted from: Almeida et. al., 2017)

Reservoir ID	Characteristics	
Póvoa e Meadas (P1)		
	Coordinates	X: 7° 32' 34.9''W Y: 39° 28' 4,5''N
	Hydrographic basin	Tagus
	Main affluent	Nisa stream
	Total Area	225,8 ha
	N° tributaries	7
	Average temperature	16,1 C°
	N° Sampling points	6
Penedrão (P2)		
	Coordinates	X: 8° 4' 21.752''W Y: 38° 0' 12.507''N
	Hydrographic basin	Guadiana
	Main affluent	Canhestros stream
	Total Area	86,6 ha
	N° tributaries	2
	Average temperature	16,6 C°
	N° Sampling points	3
Serpa (P3)		
	Coordinates	X: 7° 34' 54.3'' W Y: 37° 59' 42,6'' N
	Hydrographic basin	Guadiana
	Main affluent	Enxoé stream
	Total Area	148 ha
	N° tributaries	7
	Average temperature	16,9 C°
	N° Sampling points	2
Tourega (P4)		
	Coordinates	X: 8° 01' 42.4'' W Y: 38° 20' 25.5'' N
	Hydrographic basin	Sado
	Main affluent	Valverde stream
	Total Area	64,8 ha
	N° tributaries	5
	Average temperature	16,4 C°
	N° Sampling points	3
Divor (P5)		
	Coordinates	X: 7° 55' 22.986'' W Y: 38° 41' 25.762'' N
	Hydrographic basin	Tagus
	Main affluent	Divor stream
	Total Area	189,2 ha
	N° tributaries	8
	Average temperature	16,2 C°
	N° Sampling points	3

Chapter 4: : Sampling and methods

4.1 *In situ sampling*

Sampling in the various study areas was conducted between 2017 and 2019, depending on the site, profiting from different projects field campaigns (Table 4.1). When possible, dates of sampling were adjusted to guarantee coincident S2 and/or S3 satellite passages.

In the Tagus Estuary, 12 sampling points from 3 different on-going projects have been considered, namely NIPOGES (SPM and turbidity), PLATAGUS (SPM, turbidity, radiometry) and Valor Sul (SPM and turbidity), allowing to cover a large area of the estuary (Figure 4.1A). For the Sado estuary, monthly campaigns over 7 sampling points have been conducted within the AQUASADO project (SPM and turbidity), starting in March 2018 (Figure 4.1B).

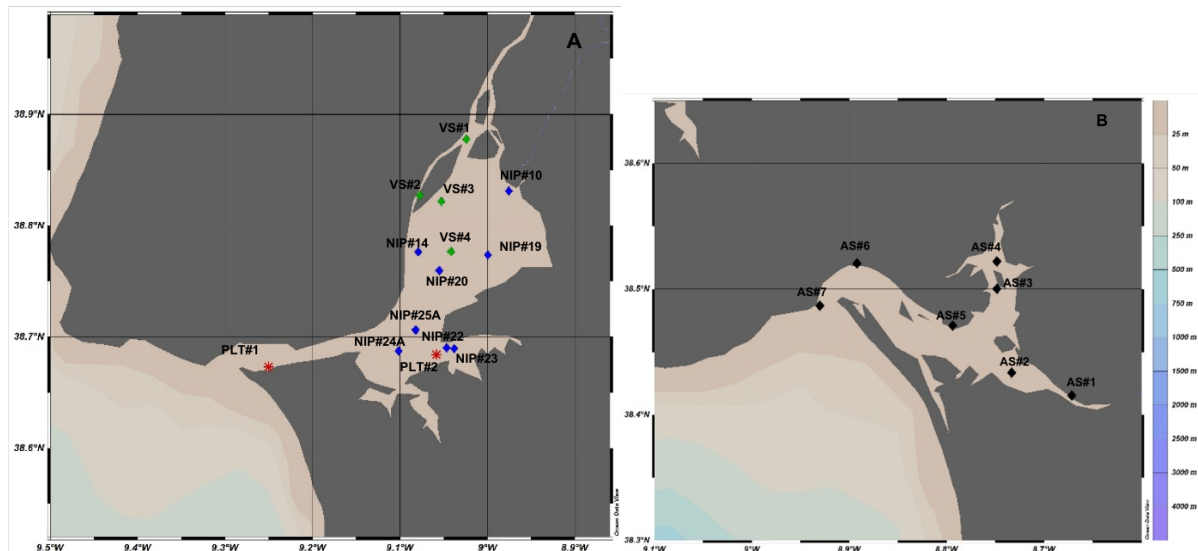


Figure 4.1 - Sampling stations in the Tagus region (A) and Sado region (B). In figure A, the blue stations correspond to the Nipoges Project (SPM and turbidity), green to the Valor Sul project (SPM and turbidity) and red to the Platagus project (SPM, turbidity and radiometry). Sampling in Sado was conducted within the framework of AQUASado project.

Regarding the inland water bodies, the sampling campaigns have been conducted in the framework of the GAMEFISH project. In this context, a total of 6 sampling points in Póvoa e Meadas reservoir (P1), 3 in Penedrão (P2), 2 in Serpa (P3), 3 in Tourega (P4) and 3 in Divor (P5) have been considered (See Table 3.1).

For all the sampling sites, SPM and turbidity data have been collected, while the radiometry measurements (ρ_w) have been performed only in the Tagus estuary area within the context of the PLATAGUS project (stations in red in Figure 1A). A summary of the data collected is presented in Table 4.1.

Table 4.1 - Summary of data collected for the different study areas. Colors highlight the different projects sampling programs. Red cells indicate samplings performed within PLATAGUS project; dark blue correspond to NIPOGES project; green correspond to Valor Sul project; yellow correspond to AQUASADO project and light blue correspond to GAMEFISH project.

		2017												2018												2019											
		1	2	3	4	5	6	7	8	9	10	11	12	1	2	3	4	5	6	7	8	9	10	11	12	1	2	3	4	5	6	7	8	9	10	11	12
Tagus	T																																				
	SPM																																				
	ρ_w																																				
Sado	T																																				
	SPM																																				
Reservoirs	T																																				
	SPM																																				

4.1.1 SPM and Organic Matter

SPM concentration (mg L^{-1}) was determined following the method described in (Van Der Linde, 1998). In summary, a volume of water sample is filtered through pre-ashed pre-weighted GF/F filters (nominal pore size $0.7 \mu\text{m}$ and 47 mm diameter), with volume dependent on the amount of material present in the water and considering that it should be sufficient to detect weights to 5 significant digits. After each sample filtration, 20 mL of MilliQ water have been filtered through the filtration apparatus to remove any salt, and other 10 mL of MilliQ have been used to wash the outer edge (unfiltered area) of the filter. To quantify sample variability, all the samples have been taken in triplicate Figure 4.2.



Figure 4.2 - Water sample filtering procedure.

Finally, the filters are stored in petri dishes at -20°C in the dark.

Before weighing, the filters are defreeze and dried in a hot air oven at 50°C for 2 hours and stored in a desiccator. The weight of each sample is measured three times and the mean is used for the calculation of the SPM concentration. The drying process is done twice to ensure the dryness of the filters through weight stability.

The SPM concentration (mg L^{-1}) is deduced from the difference between original filter weight and the sample filter weight (in mg) divided by the filtration volume (in L).

For the determination of the particulate organic matter fraction (SPOM), the same sample filters used to determine SPM concentration are placed in the muffle at 450 °C for 4 hours and the weight is registered. Another weight measurement is made after 2 hours in hot air oven at 50 °C to check weight stability. The SPOM concentration (mg L^{-1}) is deduced from the difference between the filter weight before and after muffle divided by the filtration volume.

4.1.2 Turbidity

The standard method to measure turbidity is using a turbidity meter. For the present study the Lovibond infrared turbidimeter TB 210 IR has been used (Figure 4.3A).

A 10 mL vial is filled with water sample and illuminated by an infrared light emission. The instrument quantifies the turbidity by measuring the light scattered at an angle of 90°, as stipulated in EN ISO 7027 (ISO, 1999).

Turbidity is reported in Nephelometric Turbidity Units (NTU) with an accuracy of $\pm 2,5\%$ of reading.

The instrument calibration was checked before each sampling campaign using the calibration standards provided with the instrument (<0.1 , 20, 200 and 800 NTU) and track the instrument stability.

The turbidity was always recorded in triplicate from the same water sample and averaged. Within the PLATAGUS field campaigns, a second turbidimeter has been also used in order to perform a comparison between the two instruments. The instrument used is the HACH 2100Q Portable turbidimeter (Figure 4.3B), which measures turbidity via the ratio of light scattered at an angle of 90° to forward-transmitted light as compared to the same ratio for a standard suspension of formazin (Knaeps *et al.*, 2018). Turbidity is reported in FNU (Formazin Nephelometric Unit) with an accuracy of $\pm 2\%$ of reading.



Figure 4.3 - (A) Lovibond TB 210 NR and (B) HACH 2100Q portable turbidimeters.

4.1.3 Radiometric measurements

Above water reflectance measurements have been obtained for the Tagus estuary within the PLATAGUS project. Sets of hyperspectral radiance and irradiance sensors (TriOS/RAMSES) were

mounted on two different pontoons, one at the mouth of the estuary in September 2018 and one in the inner bay of the estuary in June 2019 (Red stars in Figure 4.1A). The TriOS/RAMSES sets include one radiance (ARC) and two irradiance (ACC) hyperspectral radiometers with a sampling interval of approximately 3.3nm and an effective spectral resolution of 10nm covering the spectral range 400-900nm.

The instruments were mounted on a railing at the pontoons (Figure 4.4), using a metal structure that allows to adjust the inclination of the sensors and the Azimuth angle. Nadir and zenith angles of the sea- and sky-viewing radiance sensors were fixed at 40° degrees, respectively. The Azimuth pointing was adjusted before each measurement in order to ensure glint avoidance, to obtain a relative angle with the Sun of 90° degrees.

The inclination of the radiance sensors is measured with a portable inclinometer, while the Downwelling irradiance sensor tilt angle from Zenith is measured by the inclination module within the sensor.



Figure 4.4 - TriOS/RAMSES hyperspectral radiometers as installed on the pontoon rail.

Measurements were made for 15 minutes, taking a scan of the three instruments every 10 s.

The sensors measure over the wavelength range of 350-950 nm with a spectral width of about 10 nm and a sampling interval of approximately 3.3 nm.

Data were acquired with the MSDA-XE software and radiometrically calibrated using nominal calibration constants. The hyperspectral measurements have been finally integrated to the spectral response function of each sensor band.

Regarding the data processing, the following approach for calculation of the water-leaving reflectance was adopted. First, scans were discarded if any of the following cases occurred:

- inclination from Zenith exceeded 5 degrees;
- presence of unphysical spectral jumps in short spectral ranges;
- presence of sudden temporal jumps (incomplete or discontinuous spectra).

Once the above-mentioned criteria are evaluated, the first five scans passing these tests were mean-averaged and the standard deviation and coefficient of variation (CV) were computed.

The water-leaving reflectance is then calculated from the following equation (Equation 4.1):

Equation 4.1:

$$\rho_w = \pi \frac{L_{sea} - \rho_{sky} L_{sky}}{E_d}$$

Where E_d is the Downwelling irradiance; L_{sea} is the total upwelling radiance at a nadir angle of 40° ; L_{sky} is the sky radiance in the direction of the region of sky that reflects into the sea-viewing sensor at a nadir angle of 40° ; ρ_{sky} is the air-water interface reflection or Fresnel coefficient which was set as a fixed value of 0.0256 (Mobley, 1999). This coefficient is known to depend on wind speed, but was not calculated as in (Ruddick *et al.*, 2006) because surface gravity waves are not expected to be as strongly wind speed dependent as in a narrow estuary.

4.2 Remote sensing data (processors and algorithms)

Sentinel-2 (A/B) MSI data are provided by ESA processed to level 1C or level 2. For the present study images have been downloaded from Sentinel Scientific Data Hub (<https://scihub.copernicus.eu/>). For the study region, Sentinel-2 images were available every 5 days.

Level 1C and level 2 S2-MSI images with coincident field campaigns dates have been used to perform the match-ups. The images have been resampled to 60 m as part of the pre-processing and the single pixel have been used for the *in situ* comparison.

Sentinel-3 (A/B) images have been downloaded from Copernicus Open Data Access (<https://codata.eumetsat.int/>). The temporal resolution of this satellite for the Portuguese region is about 1-2 days. As done for the S2-MSI data, the S3-OLCI images (L1C and L2) with coincident field sampling dates have been downloaded and used for the match-up exercise.

It should be noted that while the S2-MSI images have been used for both coastal and inland waters, S3-OLCI data were downloaded exclusively for coastal waters due to the coarse spatial resolution of the OLCI sensor compared to the reservoirs dimension.

For the S2-MSI pixel extraction, data from a single pixel (equivalent to 60 m) have been retrieved for the *in situ* comparison. For this work the single pixel value has been used rather than the mean of 3 X 3 pixels because the resolution was already resampled from 10 and 20 m to 60 m. Regarding the Sentinel-3 pixel extraction, a single pixel value has also been used for the match-ups considering the reduced size of the sampling areas and OLCI sensor resolution (*i.e.* 300 m).

Finally, match-ups have been filtered by time between the satellite passage and the *in situ* measurement, considering a window of $\pm 2h$ for coastal waters and $\pm 24h$ for inland waters.

The number of match-ups available is dependent on the AC algorithm. The algorithms test scheme for the S2-MSI and S3-OLCI are resumed in Figure 4.5.

4.2.1 Atmospheric correction approach

Five atmospheric correction (AC) processors have been compared in this study for the Tagus area where *in situ* radiometric data have been collected.

Acolite v20190326 (RBINS), BAC/BPAC (Antoine & Morel, 1999 & Nobileau & Antoine, 2005), C2RCC v2.0 (Ruddick *et al.*, 2006), Polymer v4.12. (HYGEOS) and Sen2Cor v2.8 (Main-Knorn *et al.*, 2017). It is important to note that these processors are all under active development, but publicly available and thus considered mature and useful to compare as they rely on different principles (Warren *et al.*, 2019). Some are sensor specific, like Acolite and Sen2Cor which can be applied to S2/MSI images and BAC/BPAC to S3/OLCI, while the others can be applied to both sensors, i.e., C2RCC and Polymer (Table 4.2).

Table 4.2 - Summary of AC processors available for each sensor, S2-MSI and S3-OLCI.

	<i>Sen2Cor</i>	<i>ACOLITE</i>	<i>C2RCC</i>	<i>POLYMER</i>	<i>BAC/BPAC</i>
<i>S2-MSI</i>	X	X	X	X	
<i>S3-OLCI</i>			X	X	X

Acolite is an AC processor for coastal and inland waters developed by the Management Unit of the Mathematical Model of the North Sea (MUMM) in Belgium (RBINS). It performs atmospheric correction using the dark spectrum fitting approach by default, but it can be configured to use the exponential extrapolation approach (Vanhellemont, 2019).

BAC/BPAC is the L2 standard atmospheric correction for the OLCI sensor distribute by ESA and EUMETSAT. It combines the Baseline Atmospheric Correction (described in Antoine & Morel, 1999) and the Bright Pixel Atmospheric Correction (Moore, Aiken and Lavender, 1999).

C2RCC (Case 2 Regional CoastColour), originally developed by Doerfer and Schiller (Doerffer and Schiller, 2007) is a development of the original Case 2 Regional Processor. It relies on a database of radiative transfer simulations of water-leaving reflectance and related Top-Of-Atmosphere radiances (satellite signal) (Brockmann *et al.*, 2016). The inversion of water signal and satellite signal is performed by neural networks and fully described in Brockmann *et al.*, 2016. The current version of the processor is made available through the ESA's Sentinel Toolbox SNAP and support a number of sensors, including Sentinel 2 and Sentinel 3. It is also the default processor used to generate the Case 2 Sentinel 3 OLCI standard water products.

The Sen2Cor (Sentinel 2 Correction) algorithm is designed exclusively for Sentinel 2 land products with no water applications, but it is included in the present work because it is the default processor used to produce L2-MSI data (ESA, Sen2Cor). Its methodology is based on the Dark Dense Vegetation approach (DDV) (Kaufman and Sendra, 1988). It requires some pixels in the image corresponding to dark vegetation and once the presence of those pixels is established the algorithm uses them to derive the TOA (Top-Of-Atmosphere radiance) and corrects the image. The accuracy of this approach, is closely related to the number of dark pixels identified in the scene (Ouaidrari and Vermote, 1999).

Polymer atmospheric correction (POLYnomial based algorithm applied to MERIS) was originally developed to process MERIS data and have been extended to process multiple sensors, including MSI and OLCI. This model-based algorithm is specifically designed for considering the presence of sun-glint. This AC is not exclusively based on the NIR signal, but it applies all the available spectral bands in the visible to make the atmospheric and sun-glint corrections (Steinmetz, Deschamps and Ramon, 2009)

Each processor has been used with its default settings, as this should be the best option for general use without a priori knowledge of the water body or atmospheric conditions. To ensure a high quality of the

satellite data, different quality flags have been considered and are presented in Table 4.3. This quality flags are part of the Level 2 data and when raised they indicate that something might have gone wrong during the data processing and the retrieved product should be carefully analysed. These are generally set using either thresholds for some bands (like cloud detection) or as part of the processing scheme (like exceeding the training range of neural networks).

Table 4.3 - Flags used from C2RCC and Polymer.

<i>AC Processor</i>	<i>Sensor</i>	<i>Flag</i>	<i>Meaning</i>
C2RCC	S2-MSI S3-OLCI	Rtosa_OOS	The input spectrum to the atmospheric correction neural net was out of the scope of the training range and the inversion is likely to be wrong
	S2-MSI S3-OLCI	Rtosa_OOR	The input spectrum to the atmospheric correction neural net out of training range
	S2-MSI S3-OLCI	Rhow_OOS	The Rhow input spectrum to the IOP neural net is probably not within the training range of the neural net and the inversion is likely to be wrong.
	S2-MSI S3-OLCI	Rhow_OOR	One of the inputs to the IOP retrieval neural net is out of training range
	S2-MSI S3-OLCI	Cloud_risk LAND	High downwelling transmission indicates cloudy conditions Pixel is over Land
Polymer	S2-MSI S3-OLCI	!bitmask & 1023 = 0	Invalid pixel
L2 OLCI	S3-OLCI	LAND	Pixel is over land
	S3-OLCI	CLOUD	Cloudy pixel
	S3-OLCI	CLOUD_AMBIGUOUS	Potentially cloudy pixel
	S3-OLCI	CLOUD_MARGIN	A margin around CLOUD and CLOUD_AMBIGUOUS
	S3-OLCI	AC_FAIL	Atmospheric Correction is suspect

4.2.2 Water quality algorithms approach

To estimate SPM and turbidity with S2-MSI and S3-OLCI spectral bands, different approaches have been tested (Figure 4.5).

Regarding the SPM retrieval, C2RCC – Neural Network and the Nechad et al. (2010) semi-analytical algorithm have been tested using different bands (Table 4.5). Regarding the turbidity retrieval, Nechad et al. (2009) at different bands (presented in Table 4.5) and Dogliotti et al. 2015 semi-analytical algorithms have been tested. The choice of these algorithms was driven by their global applicability (see chapter 2).

The above-mentioned semi-analytical algorithms use the same equation (Equation 4.2) with different coefficients (Table 4.4).

Equation 4.2:

$$y(\lambda) = \frac{A^\lambda \rho_w(\lambda)}{1 - \rho_w(\lambda)/C^\lambda} + B^\lambda$$

In the Equation 4.2, y is the parameter to retrieve (SPM or turbidity); A^λ and C^λ are coefficients of calibration for the wavelength λ (available in Nechad et al. (2010)), B^λ is a third coefficient to account for measurement and model errors. The coefficients corresponding to the wavelength tested in the

present work are shown in Table 4.4. Coefficients corresponding to different wavelengths are available in (Nechad, Ruddick and Park, 2009, 2010; Dogliotti *et al.*, 2015).

In the case of Dogliotti *et al.* (2015) algorithm, the term B^λ is considered equal to zero.

Table 4.4 – A^λ (gm^{-3}), B^λ (gm^{-3}) and C^λ coefficients for the semi-analytical algorithms and the wavelengths under investigation. Coefficients for all the wavelength ranging between 500.00 to 885.00 nm are available in Nechad *et al.*, 2009 and 2010.

λ (nm)	A^λ			B^λ		$10^2 C^\lambda$	
	Nechad_SPM	Nechad_Turb	Dogliotti	Nechad_SPM	Nechad_Turb	Nechad	Dogliotti
620	213.55	174.41	-	2.42	0.39	15.33	-
645	253.51	208.41	228.1	2.32	0.36	16.41	16.41
665	355.85	282.95	-	1.74	0.23	17.28	-
705	493.65	354.20	-	1.16	0.26	18.79	-
709	561.94	403.91	-	1.23	0.26	18.92	-
740	1664.72	1149.39	-	1.14	0.002	19.73	-
754	1822.38	1254.27	-	1.28	0.01	20.00	-
783	1787.56	1287.19	-	1.50	0.06	20.54	-
779	1802.62	1304.10	-	1.57	0.05	20.50	-
865	2971.93	2109.35	3078.9	2.30	-0.02	21.15	21.12

The theoretical basis for the Nechad *et al.* (2009) algorithm for the turbidity retrieval, is based on the SPM algorithm described in Nechad *et al.* (2010). It is adapted for the SPM retrieval by replacing the backscatter/SPM relationship with the backscatter/turbidity relationship. The main difference between Nechad *et al.* (2009) and Dogliotti *et al.* (2015) turbidity algorithms is related to the algorithms calibration data set used.

The Dogliotti *et al.* (2015) algorithm have been developed through the calibration of the Nechad *et al.* (2010) algorithm with two different datasets. For the red band (645 nm), data from the Southern North Sea (SNS) with turbidity values ranging from 0.3 to 100 FNU were used, while for the NIR band (865 nm), only data for the mentioned campaigns in the SNS with $T > 10$ FNU plus two campaigns in the Scheldt river (Belgium) with turbidity values as high as 255 FNU were used. This switching algorithm uses the 645 nm band in clear waters (when $\rho_{w645} < 0.05$), the 859 nm band in more turbid waters (when $\rho_{w645} > 0.07$) and blend the two algorithms when $0.05 < \rho_{w645} < 0.07$ for a smooth transition.

For the present work, only the 645 nm algorithm has been tested because of the low to medium turbidity range of the study areas. As the two sensors tested in the present study do not have the 645 nm band, the closest bands have been used, namely the 665 nm band for MSI and the 665 nm band for OLCI.

The L2 standard products of the two sensors have also been tested. The algorithms test scheme for the S2 and S3 are resumed in Figure 4.5.

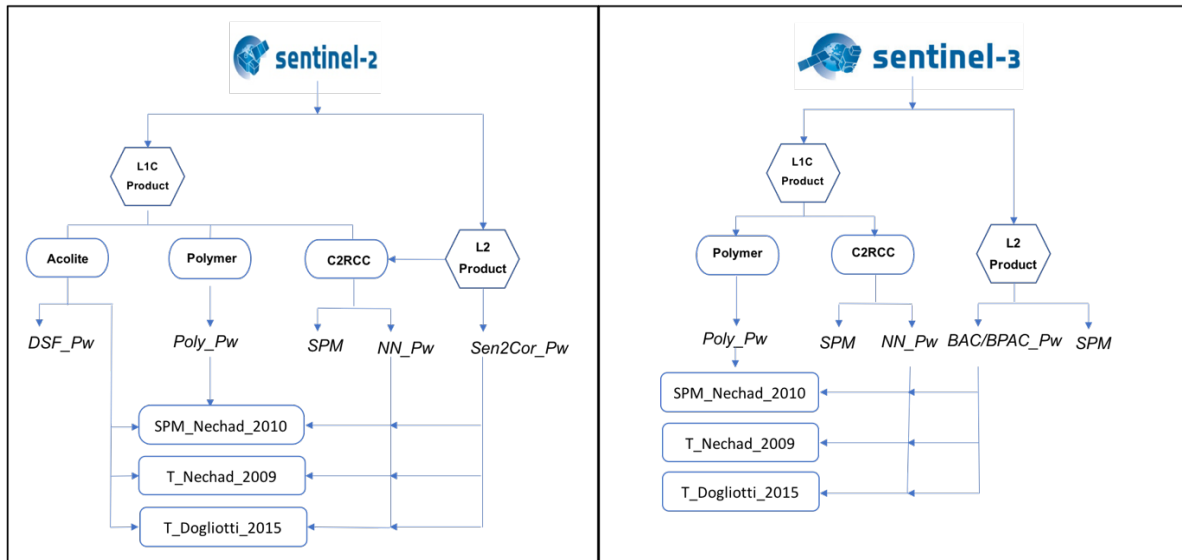


Figure 4.5 - Processing chains applied to S2-MSI products (left) and S3-OLCI (right).

Table 4.5 - Wavelengths tested for the different algorithms.

Algorithm	Sentinel 2 bands (nm)	Sentinel 3 bands (nm)
Dogliotti et al., 2015	665	655
Nechad et al., 2009	-	620
	665	655
	705	709
	740	754
	783	779
Nechad et al., 2010	865	865
	-	620
	665	655
	705	709
	740	754
	783	779
	865	865

4.2.3 Statistics analysis

For the match-ups analysis, a set of statistics to describe the differences between the satellite-derived products and the *in situ* data were calculated.

Alongside the linear regression scatterplots, a set of statistical parameters have been calculated, which includes: the slope and the intercept of the regression line, the standard error of the estimates (σ , Equation 4.3), the square of the Pearson product correlation (R^2 , the coefficient of determination (Equation 4.4), the Mean Absolute Percentage Difference (APD) (Equation 4.5) the Relative Percentage Difference (RPD) (Equation 4.6) and the Root Mean Squared Error (RMSE, ψ) (Equation 4.7).

Equations Equation 4.4 Equation 4.7) describe these metrics used to compare satellite-derived (*sat*) against field measurements (*in situ*) respectively:

Equation 4.3:

$$\sigma = \sqrt{\frac{\sum(y - y_i)^2}{N}}$$

Equation 4.4:

$$R^2 = \frac{(\sum(x_i - \bar{x})(y_i - \bar{y}))^2}{\sum(x_i - \bar{x})^2 \sum(y_i - \bar{y})^2}$$

Equation 4.5:

$$APD = \frac{1}{N} \sum_{i=1}^N \frac{|Sat_i - in\ situ_i|}{in\ situ_i} \times 100$$

Equation 4.6:

$$RPD = \frac{1}{N} \sum_{i=1}^N \frac{Sat_i - in\ situ_i}{in\ situ_i} \times 100$$

Equation 4.7:

$$\psi = \left[\frac{1}{N} \sum_{i=1}^N (sat_i - in\ situ_i)^2 \right]^{1/2}$$

Chapter 5: Results

5.1 *In situ* measurements

5.1.1 *SPM versus turbidity: sites variability*

TAGUS ESTUARY

In the Tagus estuary, water samples have been collected at similar tide conditions (± 2 h from the high tide peak) to remove the tidal influence on the SPM and turbidity variability, except for the samples collected within the PLATAGUS project, focused on getting satellite match-ups, covering therefore different tidal conditions.

The SPM and turbidity ranges (Table 5.1) suggest that there is a significant spatial variability along the estuary, with lower values in the downstream region, where there is a stronger influence of clear oceanic water, and higher values in the inner part of the estuary, where the riverine water loads sediments in the estuary.

Due to this variability, several parameters have been evaluated to better understand and assess the main drivers of the SPM:T ratio variations, namely spatial and temporal variability, tidal influence (only outer stations) and percentage in OM (only outer stations).

To evaluate the spatial variability of SPM:T dynamics, the estuary has been divided into three sections (Rodrigues et al., 2017): the inner (inn), middle (mid) and outer (out) regions (Figure 5.1). The *in situ* SPM and turbidity results for each section are shown in Table 5.1.

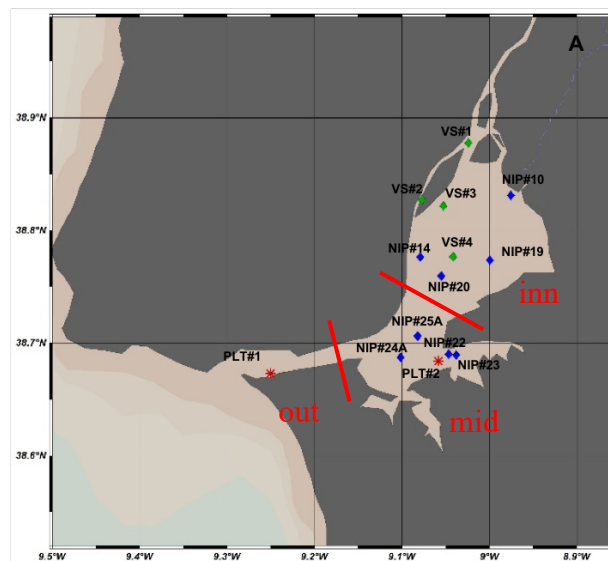


Figure 5.1 - Tagus estuary divided in three sections. “Inn” correspond to the upstream region, “mid” is middle region and “out” the downstream region. Stations highlighted in blue correspond to NIPOGES project, in green Valor Sul project and in red PLATAGUS project.

The scatterplot of SPM versus turbidity for the three different sections of the estuary is presented in

Figure 5.2. The corresponding statistics are shown in Table 5.1. The highest R^2 values are found at mid and outer stations ($R^2=0.95$ for both areas).

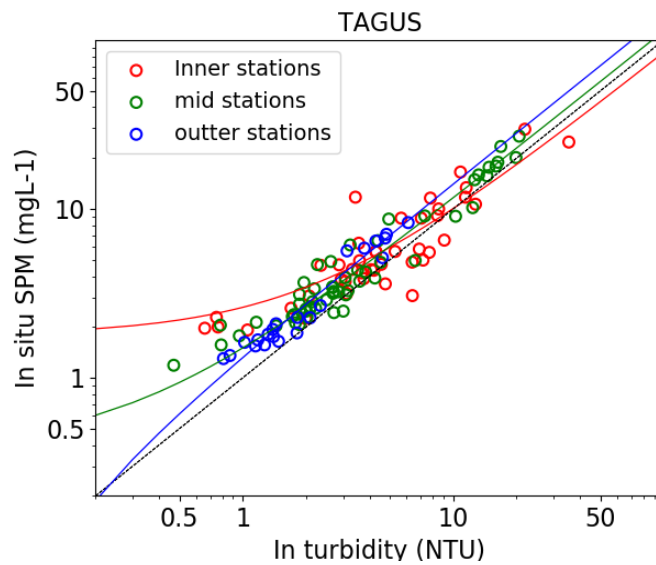


Figure 5.2 - Scatter plot of in situ SPM versus turbidity for the three sections of the estuary. The black dashed line shows the 1:1 relationship. The solid lines are the best linear fit to the data. The corresponding error statistics are shown in Table 5.1.

Analysing the SPM:T ratio for the three different section of the estuary, it is possible to see that there is an increase in the slope value of the best fitted line moving from the inner region of the basin towards the mouth of the estuary, with also an increase in the R^2 . The dispersion of the data in respect to the best fitted line also seems to decrease moving towards to the mouth of the estuary (Figure 5.2) suggesting a better correlation where there is a stronger influence of oceanic water with respect to the riverine waters which also showed higher range of variability.

Table 5.1 - Summary of SPM and turbidity statistics for the three sections of the Tagus estuary.

Region	N	SPM range (mgL ⁻¹)	Average SPM (mgL ⁻¹)	Turbidity range (NTU)	Average turbidity (NTU)	Average OM%	SPM:T ratio	R^2	Slope	Intercept
INN	41	1.92 – 29.64	6.61	0.66 – 35.43	6.22	27.00	1.37	0.77	0.827	1.787
MID	51	1.19 – 6.97	5.98	0.47 – 20.58	5.18	32.67	1.34	0.95	1.128	0.374
OUT	22	1.30 – 8.30	3.30	0.81 – 6.11	2.40	39.38	1.37	0.95	1.411	-0.094

To evaluate the seasonal effect on the SPM:T ratio, samples have been separated in 4 classes, corresponding to the astronomical seasons. The scatter plots of the SPM:T variability with season are showed in Figure 5.3 and the corresponding statistics are summarized in Table 5.2. The best R^2 and SPM:T ratio are highlighted in bold. For the outer stations, it is reminded that only summer results are available as in these stations samples were only collected during this season.

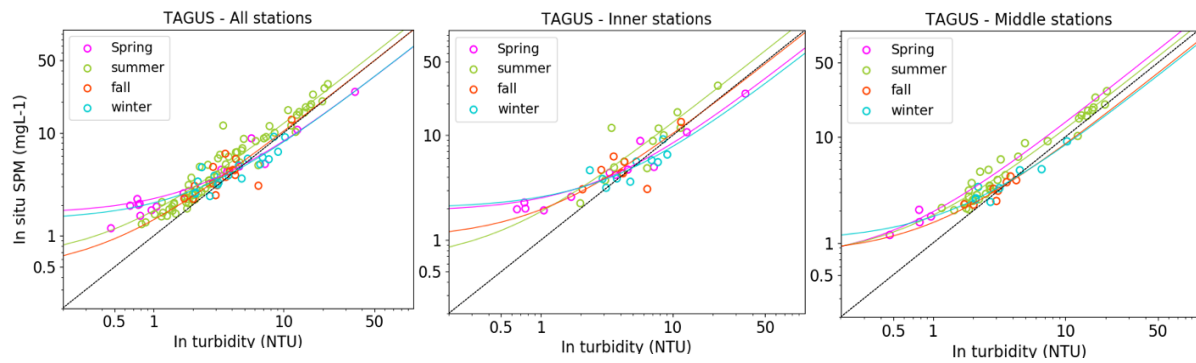


Figure 5.3 - Scatterplot of the SPM:T variability over the seasons. The dashed black lines represent the 1:1 relationship. The solid lines show the best linear fit to the data in log space. The seasonal variation of the outer stations is not presented since it has been collected only in summer.

Considering all the stations together, the highest R^2 values are found in spring and summer with a continuous decrease from spring to winter. The SPM:T ratio is closer to 1 during fall and winter with a significant increase in spring and summer.

If we separate these results for the three regions of the estuary, no particular seasonal pattern is noticed. The R^2 for the inner stations shows the highest value in spring with a progressive decrease from summer to winter. For middle region stations however, the R^2 shows the lowest value in spring and the highest in summer, being fall greater than winter (Table 5.2). Considering summer, fall and winter the mid stations show a better correlation but during spring the inner stations show a higher R^2 respect to the mid stations. As expected, the SPM:T ratio closest to 1 for the different seasons correspond to the highest R^2 values. The overall highest SPM:T ratio is found in spring at the mid stations, while the lowest value is found during winter at inner stations. It should be remarked that there is a significant variability in the amount of data for each region and season. Having similar amount of data for each group might improve the significance of the statistics and comparability of results.

Table 5.2 - Summary of seasonal variation of SPM versus turbidity for the different areas of the estuary. For the outer stations only data corresponding to summer is available. The best R^2 and SPM:T ratio are highlighted in bold.

Season	N of data	Region	Average turbidity (NTU)	Average SPM (mgL^{-1})	Ratio SPM:T ($\text{mgL}^{-1}\text{NTU}^{-1}$)	R^2
Spring	12	All stations	5.033	6.410	1.765	0.969
	8	inn	6.460	6.114	1.601	0.969
	4	mid	0.752	1.644	2.24	0.549
Summer	56	All stations	5.316	3.298	1.372	0.939
	12	inn	7.523	10.117	1.418	0.862
	34	mid	6.389	7.909	1.352	0.959
	10	Out	2.404	3.298	1.37	0.949
Fall	24	All stations	3.960	3.935	1.150	0.801
	12	inn	5,28	4.819	1.238	0.698
	12	mid	3.046	3.050	1.062	0.805
Winter	17	All stations	4.990	4.802	1.064	0.751
	10	inn	5.430	5.167	1.049	0.639
	7	mid	4.206	4.139	1.082	0.935

As already discussed before, the samples have been collected during the same tidal conditions ($\pm 2\text{h}$ from the maximum high tide peak). However, to evaluate the tidal influence on the SPM:T ratio, samples have been collected covering different tides within the PLATAGUS project (stations PLT#1 and PLT#2). The two sampling points are located at the mouth of the estuary and in the middle region.

respectively (see Figure 3.1a), allowing a better understanding of the tidal influence in the different areas of the estuary. Samples have been separated in two classes, depending if being collected during high or low tide. Moreover, to assess how the SPOM affects the SPM:T ratio, the samples have also been considered into two classes, this time depending if the SPOM percentage was greater or smaller than 50%. Results are shown in Figure 5.4.

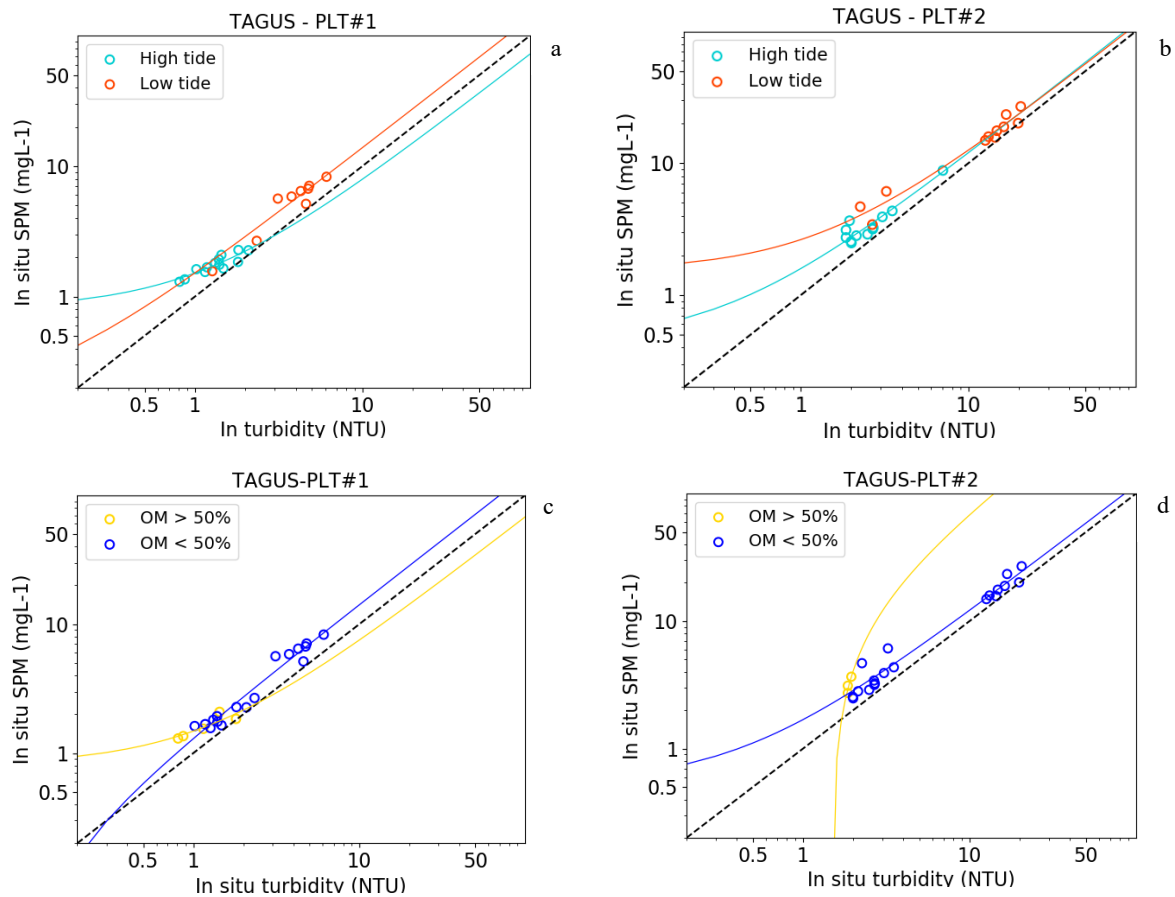


Figure 5.4 - Scatterplots of SPM versus turbidity for the different tidal conditions (a, b) and percentage in organic matter (c, d). The dashed black lines show 1:1 relationship, the solid lines are the best linear fit to the data in log space.

The highest correlations are found with low tide for both stations, with a small variability between the two tides conditions at the mouth of the estuary (PLT#1 $R^2_{\text{high tide}}=0.769$; $R^2_{\text{low tide}}=0.879$) and a more significant variability in the inner basin (PLT#2 $R^2_{\text{high tide}}=0.579$; $R^2_{\text{low tide}}=0.938$). The overall highest R^2 value is found at PLT#2 during low tide. Results of statistics when considering the tides and the percentage in OM are presented in Table 5.3. It should be remarked here that the amount of data points with SPOM >50% is very small. Because of that, results should be carefully interpreted, and no generalization considered.

Table 5.3 - Summary of SPM and turbidity statistics when taking into account tides and percentage in OM.

Station	N of data	%OM	Tide condition	Average turbidity (NTU)	Average SPM (mgL ⁻¹)	Ratio SPM:T (mgL ⁻¹ NTU ⁻¹)	R ²
PLT#1	17	< 50%	-	1.22	1.63	1.36	0.945
	5	> 50%	-	2.75	3.79	1.40	0.696
	13	-	high	1.36	1.78	1.34	0.769
	9	-	low	3.9	5.49	1.39	0.879
PLT#2	20	< 50%	-	8.67	10.56	1.29	0.969
	3	> 50%	-	1.89	3.17	1.67	0.833
	14	-	high	2.39	3.17	1.35	0.579
	9	-	low	12.44	15.26	1.34	0.938

To evaluate how the tides affect the percentage of the SPIM/SPOM in the SPM samples, Figure 5.5 present the fractions of organic/inorganic matter for the samples collected within the PLATAGUS project. The bar plots show that higher values of SPM are found at PLT#2 station (middle bay) with a bigger variability between high tide and low tide, and absolute higher SPM concentrations are found at low tide conditions for both stations. However, when considering the variation of the SPIM and SPOM fractions of the total SPM samples, it is interesting to notice that the inorganic part (blue lines in Figure 5.5) is the main driver of the SPM variability with different tides. The organic fraction (orange lines in Figure 5.5) is maintained approximately constant through the samples collected at different tide conditions suggesting that a significant percentage of the SPOM does not vary with the tides.

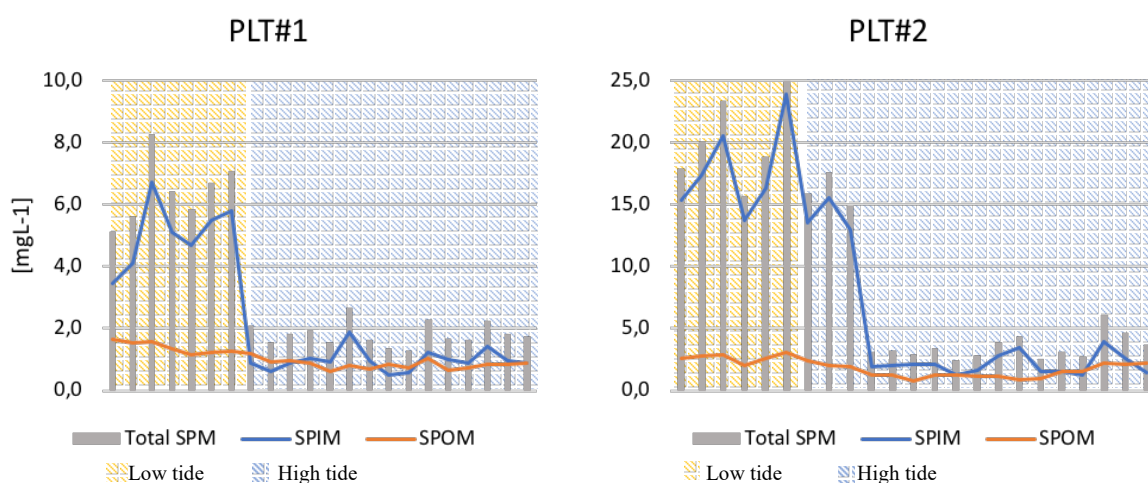


Figure 5.5 - Organic and inorganic fractions obtained for each station. The level of inorganic matter reflects the tide level of the station, with higher values on low tide conditions (yellow background) and lower values with high tide (blue background).

SADO ESTUARY

In the Sado estuary, water samples have been collected in the framework of the AQUASADO project. Sampling campaigns have been conducted monthly at similar tide conditions (high tide), and twice per year, the stations AS#5, AS#6, AS#7 and AS#8 have been sampled covering a tidal cycle.

The SPM and turbidity ranges over the estuary (Table 5.4) showed a similar distribution to the Tagus estuary, with lower ranges (clear water) at the inlet of the estuary and higher levels of suspended

sediments and turbidity in the inner region. This suggested to follow the same approach used for the Tagus and divide the estuary in three sections (Figure 5.6).

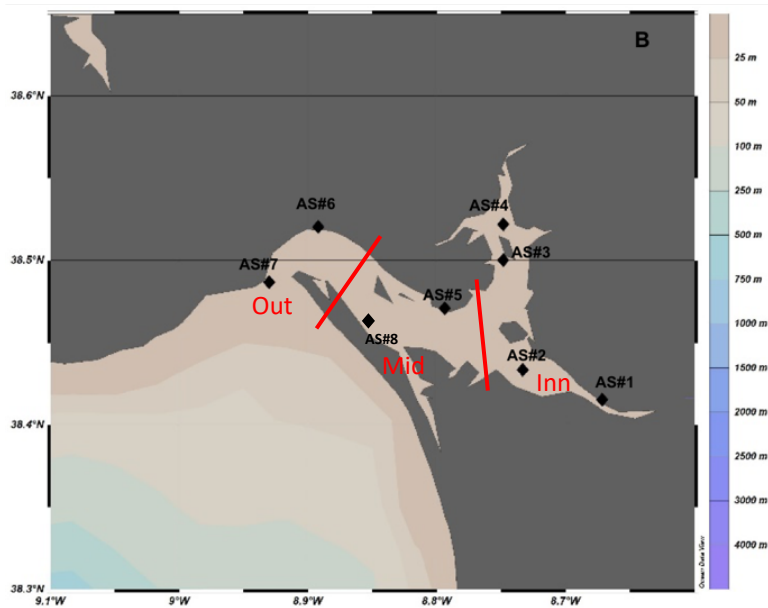


Figure 5.6 - Sado estuary divided in three sections. “Inn” correspond to the upstream region, “mid” is middle region and “out” the downstream region.

The downstream region is characterized by clear oceanic water with low ranges of SPM and turbidity, being the lowest turbidity measured 0.16 NTU at the inlet of the estuary. When moving towards the inner basin of the estuary, SPM and turbidity levels increase as expected, due to a stronger river discharge influence. As noticed in the Tagus estuary, the percentage in suspended organic matter tend to be higher at the inlet of the estuary and lower in the inner basin (Table 5.4). However, a higher percentage in organic matter in the SPM samples doesn't necessary reflect a higher concentration (mg L^{-1}). In fact, the highest concentrations of SPOM have been found in the inner bay of the estuary (Figure 6.2).

In order to study the SPM:T ratio variability, in Figure 5.7 is presented the scatterplot of SPM versus turbidity for the three different regions of the estuary considering all the data available. The corresponding statistics are showed in Table 5.4.

Sequentially, data will be separated for the different seasons of the year to study the temporal variability and finally the tidal cycles will be considered, in order to study the tidal influence on the SPM:T ratio and on the suspended organic matter percentage.

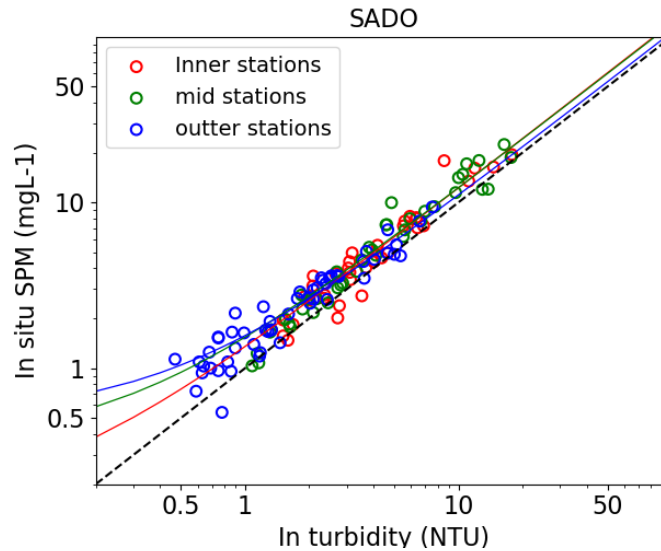


Figure 5.7 - Scatter plot of in situ SPM versus turbidity for the three sections of the Sado estuary. The black dashed line shows the 1:1 relationship. The solid lines are the best linear fit to the data in log space. The corresponding error statistics are shown in Table 5.1.

Considering the scatterplot in Figure 5.7, it is noticeable that the inner and mid stations shows very similar trend, being the best fitted line to the data almost overlapping. The highest R^2 correspond to the mid stations ($R^2 = 0.916$) even though all the three regions of the estuary presented similar R^2 values (Table 5.4).

Regarding the SPM:T ratio, inner and mid stations also presented very similar results, 1.23 and 1.25 respectively. The highest SPM:T value corresponds to outer stations.

The summary of SPM versus turbidity statistics when considering all the data for the Sado estuary is presented in Table 5.4.

Table 5.4 - Summary of SPM and turbidity statistics for the three sections of the Sado estuary.

Region	N	SPM range (mgL ⁻¹)	Average SPM (mgL ⁻¹)	Turbidity range (NTU)	Average turbidity (NTU)	Average OM%	SPM:T ratio	R ²	Slope	Intercept
Inn	36	1.47 – 34.57	6,82	1.51 – 17.80	4,85	25.15	1.228	0.902	1.208	0.143
Mid	42	1.03 – 22.37	5.562	1.08 – 17.66	5.433	34.07	1.250	0.916	1.191	0.348
Out	56	0.54 – 9.39	2.526	0.16 – 7.55	2.140	44.64	1.653	0.911	1.0590	0.515

As done for the Tagus area, the samples for the three regions of the Sado estuary have been separated in 4 classes corresponding to the seasons in order to evaluate the seasonal effect on the SPM:T ratio.

In Figure 5.8 the SPM:T relationship for the different seasons considering all the data available for the estuary (Figure 5.8a) and considering the three distinct regions of the estuary (Figure 5.8b, c, d) is presented. The corresponding statistics are shown in Table 5.5.

If considering all the stations in the estuary, the higher R^2 value is found in summer ($R^2=0.96$) and the lowest in winter ($R^2=0.70$), being spring and fall with similar results ($R^2=0.87$ for both seasons). However, the SPM:T ratio shows contrasting results (as seen for the Tagus estuary) being the value closest to 1 in winter. When separating the estuary into the three regions, the season that shows the highest R^2 values is summer, being all the R^2 values greater than 0.9. The overall highest R^2 ($R^2=0.98$)

is found during summer at inner stations. The lowest R^2 values correspond to winter for all the regions of the estuary. No particular region showed an overall better correlation respect to the others.

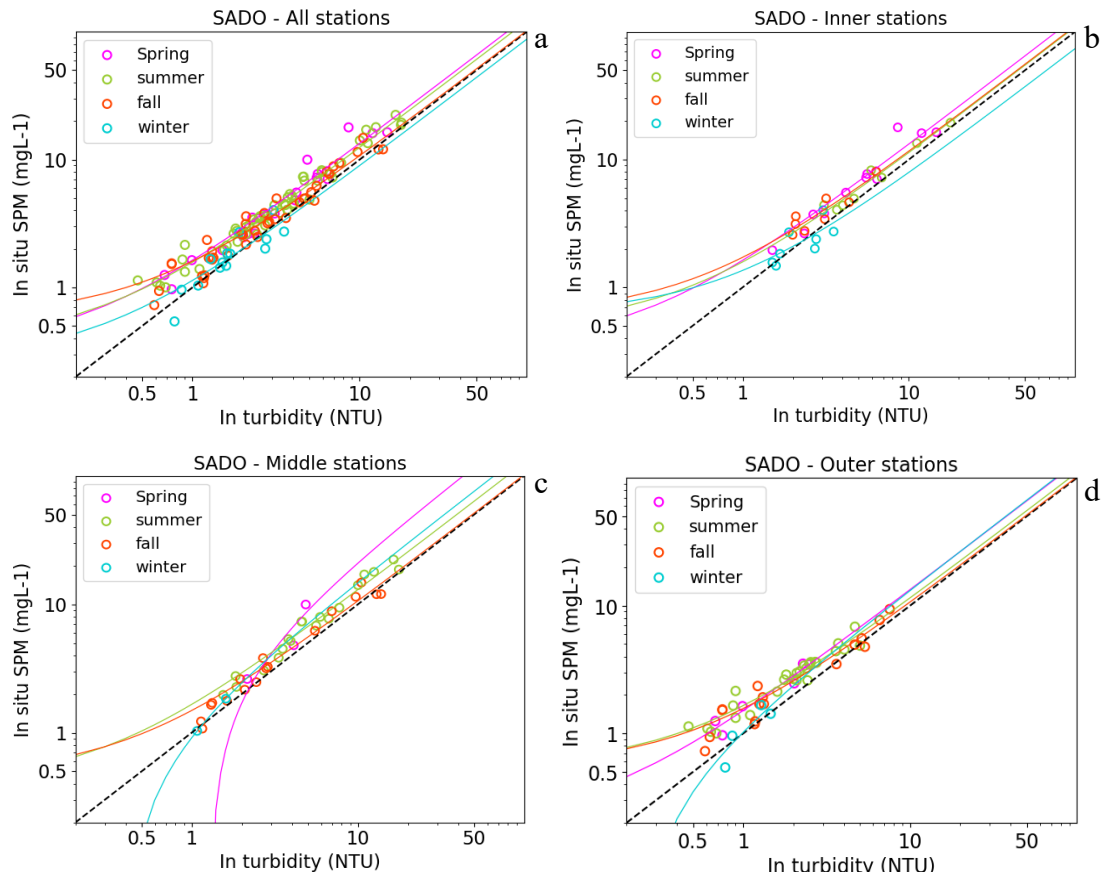


Figure 5.8 - Scatterplot of the SPM:T variability over the seasons for the Sado estuary. The dashed black lines represent the 1:1 relationship. The solid lines show the best linear fit to the data in log space.

Table 5.5 summarizes the SPM:T statistics for the Sado estuary when considering the seasonal influence on these two parameters. The best R^2 and SPM:T ratio values for each season are highlighted in bold.

Table 5.5 - Summary of seasonal variation on SPM versus turbidity for the different areas of the Sado estuary. The best R^2 and SPM:T ratio are highlighted in bold.

Season	N of data	Region	Average turbidity (NTU)	Average SPM (mgL ⁻¹)	Ratio SPM:T (mgL ⁻¹ NTU ⁻¹)	R^2
Spring	21	All stations	4.439	4.448	1.396	0.872
	12	Inn	6.073	8.169	1.330	0.843
	3	Mid	3.710	5.800	1.478	0.784
	6	Out	1.535	2.216	1.488	0.944
Summer	54	All stations	4.461	5.980	1.375	0.958
	8	Inn	7.156	8.269	1.176	0.980
	19	Mid	6.594	8.727	1.328	0.947
	25	Out	2.225	2.999	1.463	0.909
Fall	45	All stations	3.612	4.134	1.592	0.873
	8	Inn	3.195	4.141	1.334	0.878
	17	Mid	4.949	16.386	1.147	0.921
	18	Out	2.252	3.016	2.218	0.920
Winter	14	All stations	1.844	2.189	1.026	0.701
	8	Inn	2.344	2.341	1.021	0.458
	2	Mid	1.345	1.439	1.051	-
	4	Out	1.022	1.148	1.022	0.775

To evaluate the tidal influence on the SPM and turbidity relationship and variability, three campaigns have been conducted to sample different tidal conditions at four stations (AS#5, AS#6, AS#7, AS#8) in the Sado estuary. In Figure 5.9 are presented the scatterplots of the SPM:T relationship when considering two different tidal conditions (high tide and low tide) (Figure 5.9a, b) and when considering the percentage in organic matter (if greater or smaller than 50%) (Figure 5.9c, d). This analysis has been performed exclusively for mid and outer stations because no data was available for the inner stations when considering different tidal conditions.

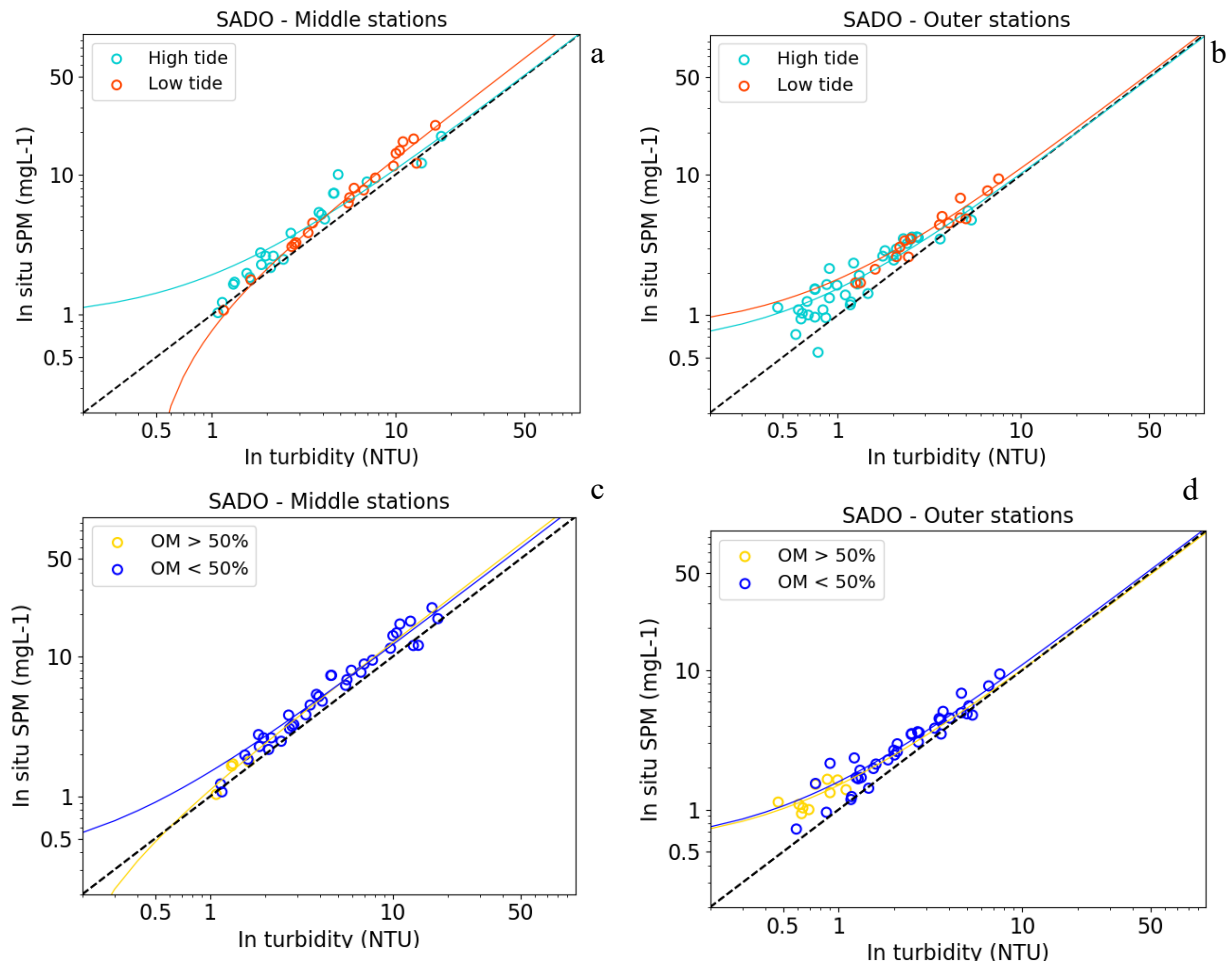


Figure 5.9 - Scatterplots of SPM versus turbidity for the different tidal conditions (A, B) and percentage in organic matter (C, D). The dashed black lines show 1:1 relationship, the solid lines are the best linear fit to the data in log space.

In both areas of the estuary, the best R^2 is found at low tide conditions (Table 5.6), behavior noticed also for the Tagus estuary. Mid stations showed a general better correlation for both tides respect to outer stations.

Regarding the SPM:T relationship, when considering the percentage in organic matter, a significant difference has been found between samples with $OM > 50\%$ and samples with $OM < 50\%$. At both mid and outer stations, the R^2 is greater when the percentage in organic matter is smaller ($R^2=0.907$; $R^2=0.898$, respectively). When the OM percentage is greater than 50% the R^2 drops down for both stations ($R^2=0.535$; $R^2=0.486$, respectively). However, it should be considered that the number of samples with $OM > 50\%$ is very small, being most samples with $OM > 50\%$ found at outer stations. Again, the same trend was found in the Tagus estuary.

Summary of the statistics is presented in Table 5.6.

Table 5.6 - Summary of SPM and turbidity statistics when considering tides and percentage in OM.

Station	N of data	%OM	Tide condition	Average turbidity (NTU)	Average SPM (mgL ⁻¹)	Ratio SPM:T (mgL ⁻¹ NTU ⁻¹)	R ²
Mid stations	22	-	High	4.16	4.59	1.28	0.904
	20	-	Low	7.318	6.837	1.203	0.938
	36	<50%	-	5.83	6.31	1.24	0.907
	3	>50%	-	1.42	1.71	1.21	0.535
Outer stations	38	-	High	1.742	2.213	1.428	0.874
	16	-	Low	3.426	3.555	2.156	0.897
	43	<50%	-	2.35	2.920	1.340	0.898
	10	>50%	-	0.77	1.25	1.71	0.486

For a better understanding of the tidal influence on the percentage in suspended organic matter, in Figure 5.10 are shown both the organic and inorganic fractions of the SPM samples collected during the tidal cycles. The black dashed boxes separate the samples per day of collection. The stations AS#5 and AS#8 are located at mid estuary while AS#6 and AS#7 are outer stations.

Examining the Figure 5.10 it can be noticed that the SPIM concentration (blue lines) in the total SPM sample (grey bars) follows the tidal trend, presenting higher values with low tide and lower values during high tide conditions at all stations. However, when considering the SPOM (orange lines), it is noticeable that it remains substantially constant at different tidal conditions. This suggests that a significant part of the suspended organic matter is not affected by the tide. The same conclusions have been attained for the Tagus estuary.

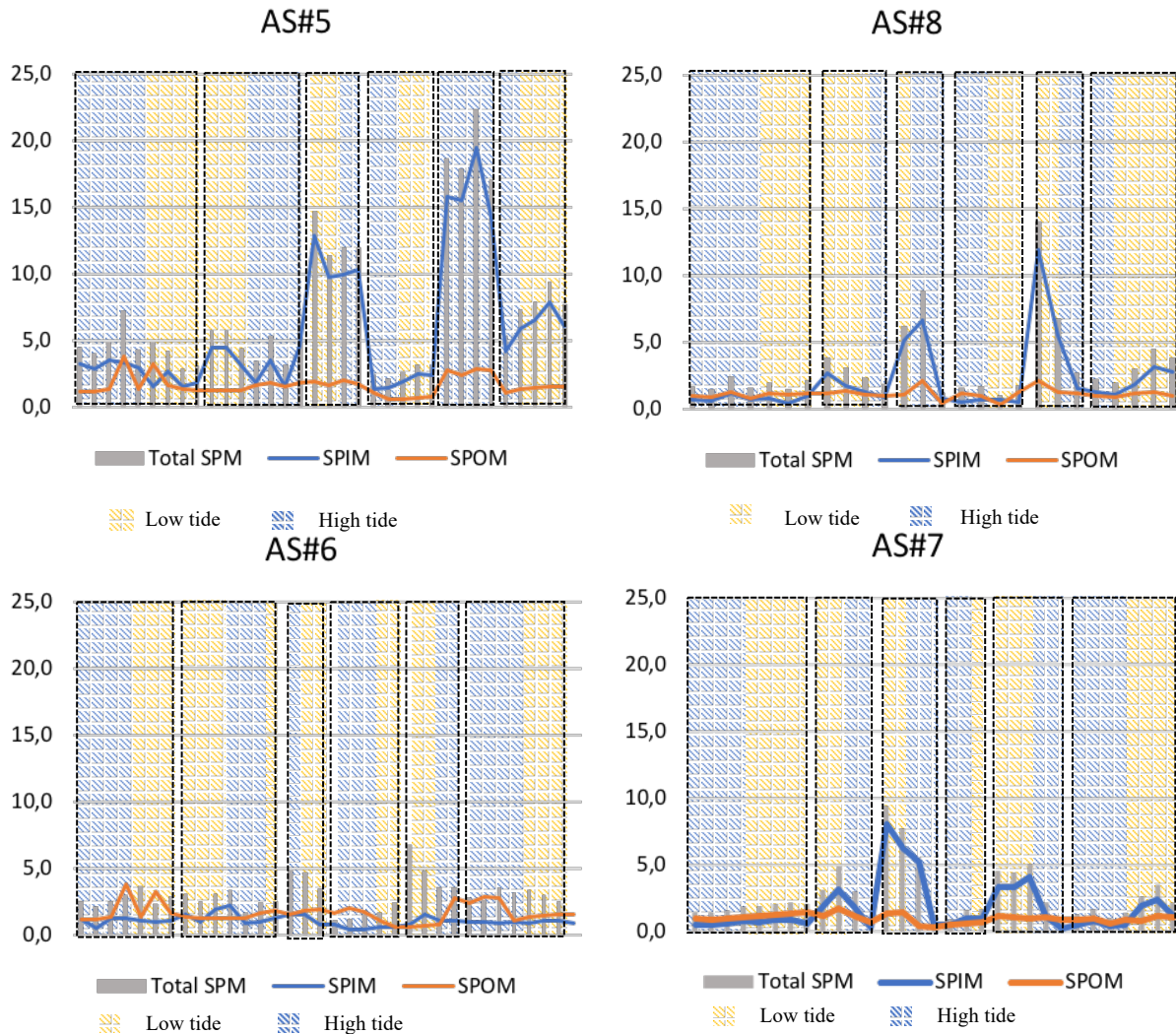


Figure 5.10 - Organic and inorganic fractions obtained for each station. The level of inorganic matter reflects the tide level of the station, with higher values on low tide conditions (yellow background) and lower values with high tide (blue background). The black dashed lines separate the sampling dates.

INLAND WATERS

Regarding the inland waters, a very little number of turbidity measurements were available, which includes 10 measurements for the P1 reservoir and 1 for both P3 and P5 reservoirs. No turbidity data are available for P2 and P4 reservoirs.

The SPM concentration, as well as the SPIM/SPOM fractions, varied substantially over time and between the individual reservoir, although no high spatial variability have been noticed within each water body (Table 5.7).

Table 5.7 – Sampling period and in situ results of SPM (SPIM and SPOM) for the studied reservoirs.

<i>Reservoir</i>	<i>Sampling period</i>	<i>SPM range</i>		
		SPM(mgL-1)	SPIM (%)	SPOM (%)
<i>Póvoa e Meadas</i>	October 2017	8.4-27	10-14	86-90
	January 2018	2.0-2.4	3-48	52-97
	February 2018	2.0-3.8	4-7	93-96
	April 2018	1.8-2.4	9-52	48-91
	May 2018	5.4-5.6	25-31	69-75
	June 2018	5.1-6.5	-	-
	July 2018	5.7-8.3	-	-
	October 2018	5.8-8.7	6-54	46-94
	January 2019	4.6-4.9	47-49	51-53
	20 May 2019	4.7-19	7-27	73-93
<i>Penedrão</i>	October 2017	4.0-7.1	43-69	31-57
	January 2018	3.3-4.2	4-48	52-96
	February 2018	2.2-2.9	31-42	58-69
	April 2018	2.5-3.0	49-52	48-50
	June 2018	1.3-2.5	-	-
<i>Serpa</i>	October 2017	4.4-6.1	27-42	58-73
	January 2018	2.4-2.7	11-25	75-89
	February 2018	4.4-4.8	48-49	51-52
	April 2018	3.6-3.8	14	85
	June 2018	7.5-8.2	-	-
	May 2019	4.4	24	76
<i>Tourega</i>	October 2017	42.1-50.2	1-7	93-99
	December 2017	35.2-36	-	-
	February 2018	44.1-55.9	16-19	81-84
	April 2018	11.7-39.7	-	-
	June 2018	9.4-10.6	-	-
<i>Divor</i>	October 2017	60,1-121,1	14-50	50-86
	December 2017	60,0-72	17-26	74-83
	February 2018	70.2-86.3	18-34	66-82
	April 2018	8.8-9.4	-	-
	June 2018	3.1-9.2	-	-
	May 2019	19.1	27	73

The SPOM ranges suggested an overall higher concentration of OM compared to the estuaries. In all the reservoirs, the maximum peak of SPM was observed in October 2017 with a decrease trend until April 2018, when the minimum SPM values are found. Serpa reservoir was an exception to this trend, indeed it showed a low variability and no decreasing trend over the sampling period.

Despite the small amount of data, a preliminary SPM:T analysis for the inland waters has been attempted. First, considering all the water bodies as a whole (Figure 5.11a), and sequentially, considering only P1 reservoir (Figure 5.11b) which is the water body with more available data.

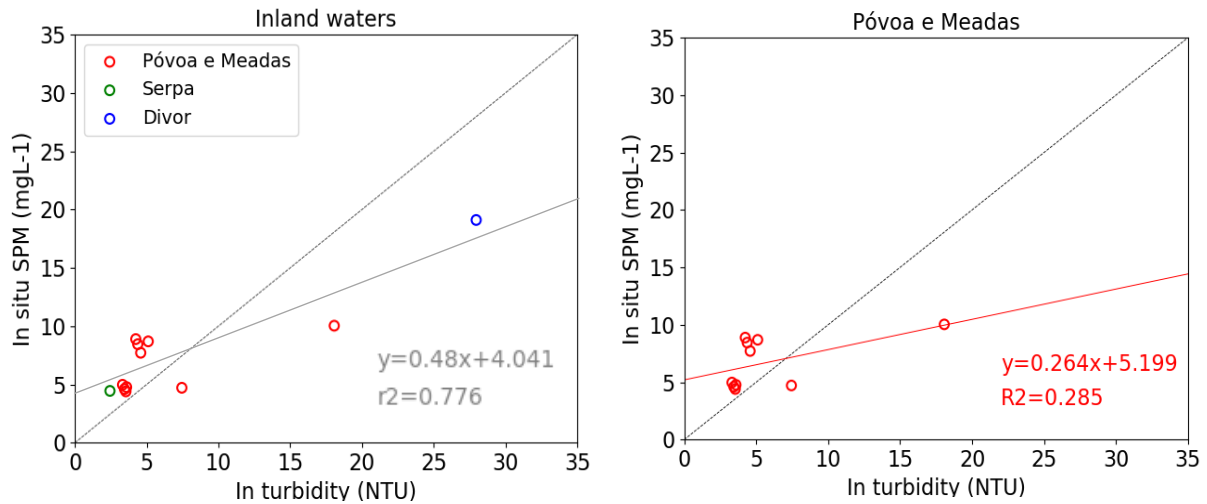


Figure 5.11. - Scatterplot representing the turbidity versus SPM for the inland waters. (a) shows the scatterplot when considering all the data available. In (b) only the Póvoa e Meadas reservoir (P1) has been considered.

Examining Figure 5.11, the scatterplots of the SPM:T ratio show controversial results. In fact, a higher correlation was expected between data from the same waterbody respect to data coming from different reservoirs. However, it is noticeable that the scatterplots show a significant higher correlation when using all data available from the different waterbodies respect to when considering only one reservoir.

Should be remarked that results presented here are preliminary and more data from all the reservoirs is needed for a better understanding of the SPM:T variability in inland waters.

5.1.2 Radiometry

In order to test different AC processors, *in situ* radiometric measurements have been conducted within the context of PLATAGUS project in the Tagus estuary. The two campaigns presented marked differences, being the first campaign conducted at the mouth of the estuary and the second campaign in the inner basin. Radiometric measurements depict the tidal variability at both stations, with spectra having mainly two distinct shapes (Figure 5.12).

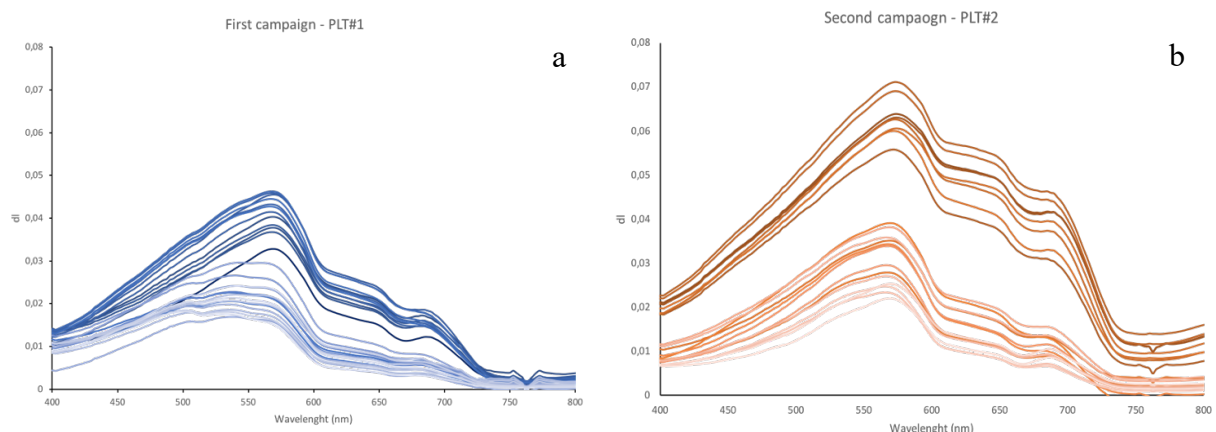


Figure 5.12 - Average *in situ* water reflectance (R_{how}) for each sampling station. On the left (a) the stations collected during the first campaign (blue lines) and on the right (b) the second campaign (orange lines). In both plots, the intensity of the line color reflects the tidal conditions, with darker colors for samples collected during low tide (higher reflectance) and lighter colors for samples collected during high tide (lower reflectance).

The spectrum amplitude in Figure 5.12 reflects the tidal conditions of each station. The highest values of reflectance corresponding to low tide conditions. These stations, with higher turbidity, appear more reflective, particularly in the region ~570nm (and in the NIR), where sediments are expected to produce more signal in reflectance.

The radiometric measurements conducted at the PLT#2 station presented overall higher values that can be explained by the location of the two stations. As showed before, PLT#2 is located in the inner basin of the estuary presenting higher ranges of SPM and turbidity. Moreover, in Figure 5.12 it can be noticed that the two plots differ on the spectral shape between high and low tide conditions. While in PLT#1 it is possible to see a difference in the shape and amplitude between tides, in PLT#2 there is a difference in amplitude but the shape is maintained, suggesting a bigger difference in the characteristics of the water between tides at the mouth of the estuary with respect to the inner basin where the type of water is maintained similar.

5.2 Remote sensing algorithms test

Regarding the satellite imagery for the sampling period, several stations had coincident clear sky conditions and satellite overpass. The analysis of the spectra of the valid water pixels closer to the sampling locations have been compared with the *in situ* radiometric measurements in order to test different AC and choose the best performing processors/wavelengths to test SPM and turbidity retrieval algorithms.

Regarding Sado estuary and the inland water bodies, no *in situ* radiometric measurements are available. Results for all processors and wavelengths will be presented considering the PLATAGUS sampling in Tagus estuary.

For a more comprehensive evaluation of the SPM and turbidity algorithms retrieval, *in situ* radiometric measurements have also been used to estimate SPM and turbidity through the algorithms equations and compared to the *in situ* SPM and turbidity values for the Tagus estuary.

5.2.1 Atmospheric correction comparison

Despite the small amount of available match-ups, the performance of the S2-MSI and S3-OLCI Rrs were evaluated by comparison to the *in situ* data. Results and statistics are presented per wavelength.

Figure 5.13 shows the scatterplots with the spectral performance of each AC processor at different wavelengths for the two sensors. Each processor is depicted by a specific color and the wavelength by a symbol. For interpretation of the references to symbols see Figure 5.13 legend.

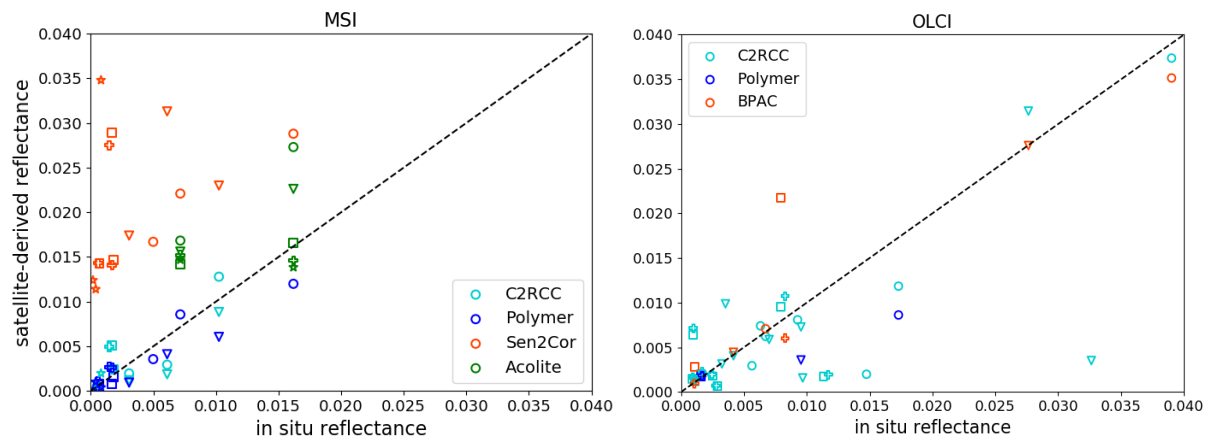


Figure 5.13 - Atmospheric correction performance per sensor, S2-MSI (a) and S3_OLCI (b). Symbols are referred to the different wavelengths. Circles for 665nm (MSI and OLCI); triangles for 705nm (MSI) and 709nm (OLCI); squares for 740nm (MSI) and 754 (OLCI); pluses for 783nm (MSI) and 779nm (OLCI); stars for 865nm (MSI) and 620nm (OLCI). The black dashed lines represent the 1:1 relationship.

Despite the small amount of available S2-MSI (*i.e.*, 2 for Acolite and 3 for C2RCC, Sen2Cor and Polymer) and S3-OLCI match-ups (*i.e.*, 8 for C2RCC, 2 for BPAC and 1 for Polymer), statistical results are shown in Table 5.8 and Table 5.9.

Regarding S2-MSI, Polymer and C2RCC performed best producing higher R^2 and low RMSE (Table 5.8). Sen2Cor showed low R^2 values and APD > 100% for all wavelengths. Since only 2 data points were available for Acolite processors, statistics are not presented here. However, examining Figure 5.13a, a general overestimation, when compared to the *in situ* data, is noticeable for both Acolite and Sen2Cor processors. Nevertheless, such results cannot be considered statistically significant due to the small amount of datapoints used.

S2-MSI statistical results are shown in Table 5.8.

Table 5.8 - Summary of statistics of S2-MSI reflectance match-up analysis processed using different AC processors. Numbers in bold represent the best value for that statistics.

Processor	Wavelength (nm)	N	R^2	Slope	Intercept	STDERR	RPD (%)	APD (%)	RMSE
C2RCC	665	3	0.989	1.002	-0.003	0.103	-46.83	46.83	0.004
	705	3	0.878	1.101	-0.003	0.410	-48.02	48.02	0.003
	740	3	0.590	2.914	-0.001	2.426	60.37	95.15	0.002
	783	3	0.516	2.833	-0.001	2.743	76.24	107.48	0.002
	865	3	0.987	2.824	-0.000	0.315	83.47	102.64	0.001
Sen2Cor	665	3	0.924	0.981	0.013	0.280	173.801	173.80	0.013
	705	3	0.101	0.618	0.019	1.840	335.07	335.07	0.018
	740	3	0.178	5.592	0.011	12.016	1426.96	1426.96	0.019
	783	3	0.097	4.107	0.013	12.411	1601.82	1601.82	0.018
	865	3	0.861	37.537	0.002	15.085	4616.17	4616.17	0.022
Polymer	665	3	0.812	0.643	0.002	0.309	-11.56	24.75	0.002
	705	3	0.949	0.699	-0.001	0.161	-47.66	47.66	0.003
	740	3	0.345	0.409	0.0005	0.563	-14.48	28.72	0.002
	783	3	0.949	1.539	0.0001	0.355	70.65	70.65	0.001
	865	3	0.040	0.315	0.0003	1.535	4.64	101.14	0.000

The dataset available for the S3-OLCI is inadequate for statistical comparison between the different processors. However, the 8 match-ups available for the C2RCC processor revealed a poor correlation ($R^2=0.26$ at 665 nm) between the data retrieved with this processor and the *in situ* data, with a significant dispersion of measurements to the 1:1 line. Statistical results are presented in Table 5.9. Statistics regarding BPAC and Polymer are not presented since not enough data were available for a statistical analysis.

Table 5.9 - Summary of statistics of S3-OLCI reflectance match-up analysis Rrs processed with C2RCC. Results from BPAC and Polymer didn't allow to perform any statistical analysis, therefore results are not presented.

PROCESSOR	WAVELENGTH	N	R ²	SLOPE	INTERCEPT	STDERR	RPD (%)	APD (%)	RMSE
C2RCC	620	8	0.245	0.437	0.003	0.313	-34.42	35.27	0.025
	665	8	0.256	0.391	0.002	0.272	-33.13	37.44	0.021
	709	8	0.213	0.391	0.003	0.307	-3.14	51.52	0.015
	754	8	0.073	0.220	0.002	0.320	60.66	108.71	0.005
	779	8	0.081	0.251	0.002	0.344	78.03	122.80	0.006

5.2.2 Water-quality algorithms comparison: SPM

TAGUS ESTUARY

From the AC test of S2-MSI, two processors have been selected, C2RCC and Polymer, for testing the SPM and turbidity retrieval algorithms. Figure 5.14 shows the performance of the SPM derived with Nechad et al. 2010 when compared to the *in situ* measurements. For a better understanding of the Nechad et al. (2010) algorithm performance, it has been applied also to the *in situ* radiometric measurements (brown symbols). The corresponding statistics are shown in Table 5.10.

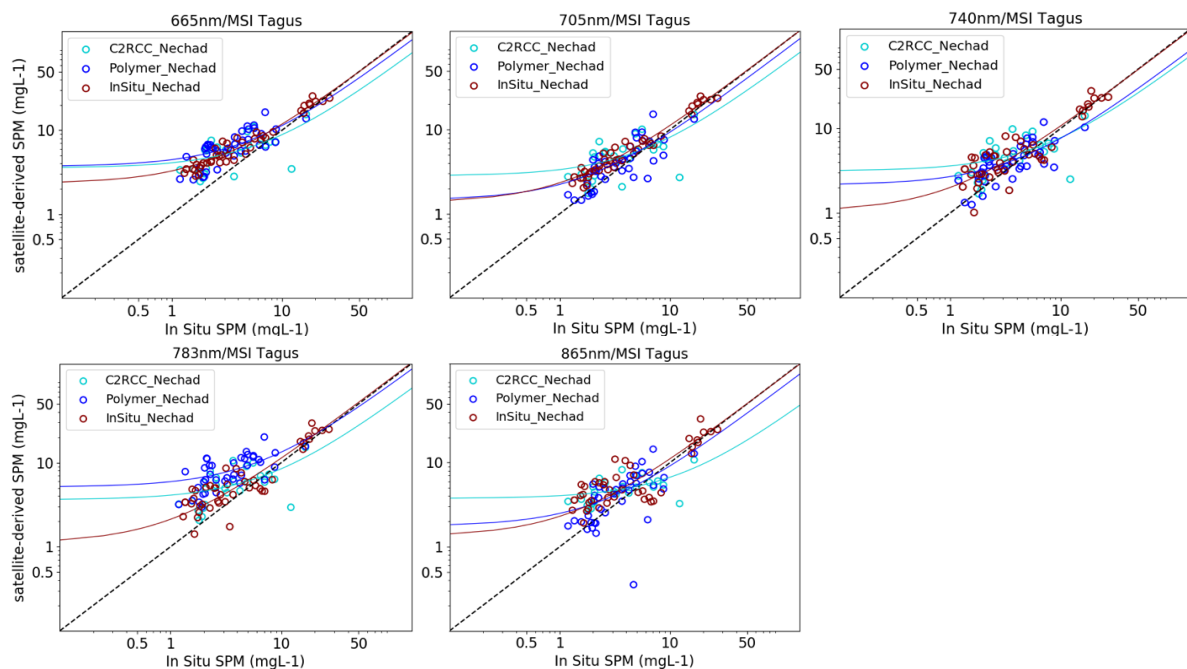


Figure 5.14 - Comparison of *in situ* and S2-MSI-derived SPM estimates at different wavelengths for the Tagus estuary in log space. Data represent match-ups for the concurrent satellite and field measurements collected during several research projects. The dashed black lines show 1:1 relationship, the solid lines are the best linear fit to the data in a log space.

Data displayed in Figure 5.14 are separated by wavelengths. For the C2RCC processor none of the wavelengths showed a good correlation with the *in situ* data, being the highest R^2 equal to 0.42 at 665 nm

and 705 nm. Regarding Polymer, a better correlation has been found comparing to C2RCC, with the highest correlation at 705 nm with R^2 equal to 0.54, slope closer to 1, but higher APD, RPD and RMSE compared to C2RCC for the same band. C2RCC presented in general APD errors greater than 50% at all wavelengths (Table 5.10), while Polymer showed APD smaller than 50% at 740 and 865 nm. Table 5.10 also show the statistical results of the SPM product derived from the Neural Network. Statistical results and scatterplots from all the processors analyzed in the present study are shown in Figure A.1. Considering the Nechad algorithm applied to *in situ* reflectance (ρ_w), the statistical results showed that 665 nm and 705 nm present the highest R^2 with small errors associated which reinforces the significance of the satellite-derived results. However, the relative and absolute percentage errors, around 66% and 40% for 665 and 705nm bands respectively, already indicate some scatter and overestimation of measured values by the algorithm itself.

Table 5.10 - Summary of statistics for SPM S2-MSI match-ups results for the Tagus estuary. Bolded number show the best value of each statistics for all processors.

Processor	Algorithm	Wavelength (nm)	N	R^2	Slope	Intercept	STDERR	RPD (%)	APD (%)	RMSE
<i>in situ</i> ρ_w	Nechad et al., 2010	665	45	0.955	0.951	2.315	0.03	66.69	67.40	2.47
	Nechad et al., 2010	705	45	0.956	0.989	1.345	0.03	40.52	41.77	1.90
	Nechad et al., 2010	740	45	0.892	0.967	1.038	0.05	35.00	53.25	2.43
	Nechad et al., 2010	783	45	0.890	1.022	1.096	0.05	43.33	59.51	2.73
	Nechad et al., 2010	865	45	0.766	0.980	1.32	0.08	50.26	83.99	3.87
C2RCC	NN	-	26	0.284	1.0138	5.504	0.328	182.68	190.63	7.97
	Nechad et al., 2010	665	26	0.423	0.529	3.553	0.126	69.79	79.86	3.12
	Nechad et al., 2010	705	26	0.419	0.531	2.815	0.127	47.77	61.62	3.05
	Nechad et al., 2010	740	26	0.346	0.462	3.139	0.129	45.76	60.58	2.86
	Nechad et al., 2010	783	26	0.343	0.483	3.617	0.136	66.20	76.60	3.274
	Nechad et al., 2010	865	26	0.325	0.296	3.748	0.086	54.41	70.26	2.98
Polymer	Nechad et al., 2010	665	39	0.502	0.768	3.687	0.1265	96.669	99.04	3.61
	Nechad et al., 2010	705	39	0.539	0.790	1.441	0.1213	-75.318	75.32	4.27
	Nechad et al., 2010	740	39	0.482	0.551	2.143	0.0938	24.408	39.45	2.27
	Nechad et al., 2010	783	39	0.398	0.823	5.111	0.1676	51.911	52.92	5.33
	Nechad et al., 2010	865	39	0.475	0.741	1.750	0.1294	29.348	47.75	2.47

Regarding the S3-OLCI, no particular processor or wavelength have been chosen from the AC test. Because of this, in Figure 5.15 are presented the results for the three processors for all the wavelengths under investigation with the corresponding statistics in Table 5.11. *In situ* reflectance have been used to test the Nechad et al. 2010 using the same wavelengths used to test the OLCI sensor reflectance values.

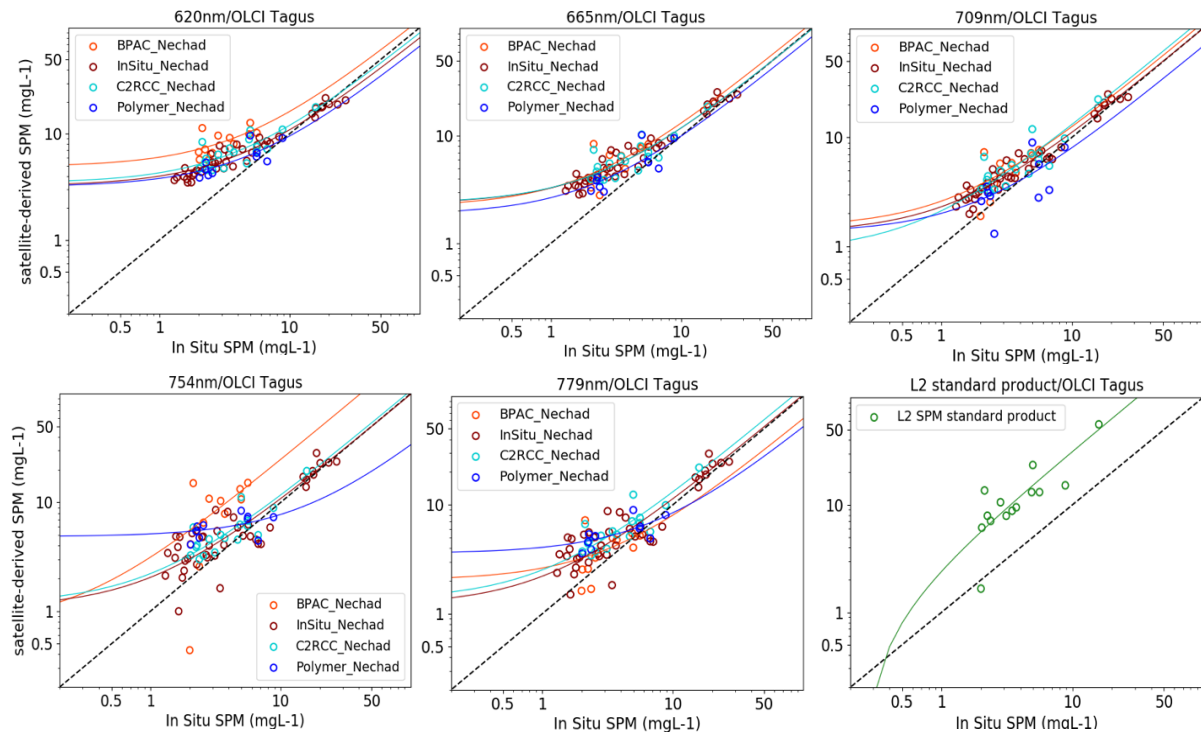


Figure 5.15 - Comparison of in situ and S3-OLCI-derived SPM estimates at different wavelengths. Data represent match-ups for the concurrent satellite and field measurements collected during several research projects. The dashed black lines show 1:1 relationship, the solid lines are the best linear fit to the data in log space.

Table 5.11 gives a summary on the correlation, coefficients of the regression (intercept and slope) and associated errors between the investigated variables. It is observed from this table that the highest correlation from S3-OLCI is obtained with the standard L2 SPM product ($R^2=0.84$), but it shows high RPD and APD errors and slope. Just as a reminder, this L2 product is directly derived from the neural network inversion instead of an equation applied to a reflectance value (Fig. 4.5). C2RCC processor showed a good correlation by applying the Nechad algorithm at 709 nm ($R^2=0.82$; $RMSE=4.90$). This processor resulted to be the best performing overall, obtaining all the wavelengths with $R^2 > 0.7$. Polymer resulted to be the least performing processor for the OLCI sensor presenting $R^2 < 0.6$ at all the wavelength with, however, smaller errors associated errors.

The best performing wavelength resulted to be the 709 nm with all the processors. This result is reinforced by the application of the Nechad algorithm to *in situ* ρ_w which also showed the best relationship with *in situ* SPM at 709 nm.

Table 5.11 – Summary of statistics for SPM S3-OLCI match-ups for the Tagus estuary. Numbers in bold show the best value of each statistics for all processors.

Processor	Algorithm	Wavelength (nm)	N	R ²	Slope	Intercept	STDERR	RPD (%)	APD (%)	RMSE
<i>in situ</i> ρ_w	Nechad et al., 2010	620	44	0.942	0.769	3.222	0.03	76.82	79.49	2.62
	Nechad et al., 2010	665	44	0.954	0.951	2.322	0.03	67.30	68.03	2.48
	Nechad et al., 2010	709	44	0.957	1.226	0.884	0.14	40.16	41.92	1.86
	Nechad et al., 2010	754	44	0.878	0.977	1.07	0.05	39.50	59.69	2.66
	Nechad et al., 2010	779	44	0.887	1.188	1.193	0.05	47.98	63.84	2.82
BPAC	Neural Network	-	12	0.840	3.203	-0.804	0.403	207.81	210.23	13.25
	Nechad et al., 2010	620	12	0.412	1.135	4.884	0.428	187.58	187.58	5.70
	Nechad et al., 2010	665	12	0.464	1.097	2.181	0.372	87.94	87.94	2.97
	Nechad et al., 2010	709	12	0.519	1.108	1.483	0.336	36.65	58.83	5.07
	Nechad et al., 2010	754	12	0.415	2.414	0.725	0.907	29.31	51.59	4.62
	Nechad et al., 2010	779	12	0.211	0.601	2.027	0.367	30.90	44.10	1.75
C2RCC	Nechad et al., 2010	620	18	0.789	0.858	3.431	0.110	294.70	294.70	15.26
	Nechad et al., 2010	665	18	0.816	0.953	2.342	0.112	67.68	86.10	5.07
	Nechad et al., 2010	709	18	0.816	1.226	0.884	0.145	48.73	68.94	4.90
	Nechad et al., 2010	754	18	0.809	1.054	1.161	0.127	36.65	58.83	5.07
	Nechad et al., 2010	779	18	0.813	1.183	1.344	0.141	29.31	51.59	4.62
Polymer	Nechad et al., 2010	620	10	0.1686	0.3227	4.1650	0.238	61.78	63.93	2.13
	Nechad et al., 2010	665	10	0.556	0.810	1.847	0.255	16.34	31.84	1.58
	Nechad et al., 2010	709	10	0.392	0.670	0.670	0.294	-20.37	48.38	2.03
	Nechad et al., 2010	754	10	0.231	0.290	4.846	0.187	109.85	115.83	3.69
	Nechad et al., 2010	779	10	0.445	0.487	3.587	0.192	74.19	78.35	2.56

SADO ESTUARY

For the Sado estuary, no *in situ* radiometric measurements were available to test the different AC processors. Because of this, the SPM and turbidity algorithms under investigation have been tested on satellite data with all the AC processors. Scatterplots showing the estimated (S2-MSI) and observed SPM values for each match-ups is presented in Figure 5.16 and the summary statistics are tabulated in Table 5.12.

The four processors can be divided into 2 classes, one includes Acolite and Sen2Cor and the second one C2RCC and Polymer. There are clear differences between the two groups of processors, with C2RCC and Polymer outperforming Acolite and Sen2Cor at all wavelengths. Sen2Cor resulted to be the least performing processor presenting high RMSEs and APDs > 270% at all wavelengths and the highest R²

equal to 0.33 at 740 nm. Acolite showed a better correlation at 665 nm ($R^2 = 0.46$) presenting however high APD (283%) and RMSE values.

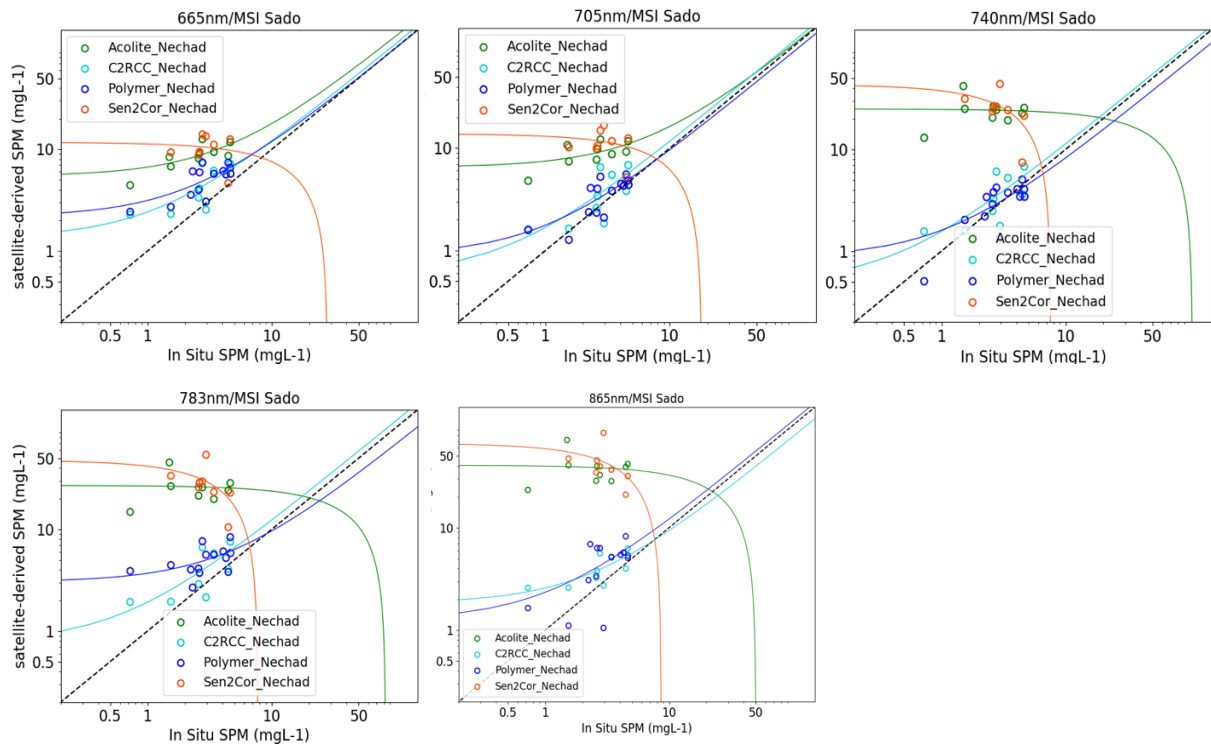


Figure 5.16 - Comparison of *in situ* and S2-MSI-derived SPM estimates at different wavelengths For the Sado estuary. The dashed black lines show the 1:1 relationship, the solid lines are the best linear fit to the data in log space.

C2RCC and Polymer had RMSEs close to 1 at all wavelengths, except for 665 nm and 783 nm wavebands for both processors with slightly higher RMSEs, suggesting a significant degree of similarity with the *in situ* data. C2RCC performed similarly to Polymer but with lower R^2 . However, as demonstrated with the Tagus estuary case-study, the satellite-derived SPM shows a poor correlation with the *in situ* data when using the Sentinel-2 imagery, being the highest R^2 equal to 0.58 when processed with Polymer and Nechad et al. (2009) at 705 nm. The number of match-ups ranged between 8 (Sen2Cor) and 14 (Polymer). Statistics are summarized in Table 5.12.

Table 5.12 - Summary of statistics for SPM S2-MSI match-ups for the Sado estuary. Numbers in bold show the best value of each statistics for all processors.

Processor	Algorithm	Wavelength (nm)	N	R ²	Slope	Intercept	stderr	RPD (%)	APD (%)	RMSE
Acolite	Nechad et al., 2010	665	9	0.463	1.246	5.439	0.506	283.25	283.25	6.34
	Nechad et al., 2010	705	9	0.318	0.982	6.493	0.542	309.37	309.37	6.69
	Nechad et al., 2010	740	9	0.001	-0.238	24.904	2.211	1066.40	1066.40	22.83
	Nechad et al., 2010	783	9	0.002	-0.327	27.003	2.421	1164.99	1164.99	24.82
	Nechad et al., 2010	865	9	0.005	-0.809	40.610	3.987	1793.55	1793.55	38.16
C2RCC	Neural Network	-	9	0.005	-0.474	28.576	1.567	1078.27	1078.27	25.34
	Nechad et al., 2010	665	9	0.446	1.083	1.338	0.455	71.18	74.24	2.12
	Nechad et al., 2010	705	9	0.452	1.111	0.571	0.462	38.67	50.26	1.70
	Nechad et al., 2010	740	9	0.466	1.087	0.473	0.439	32.59	46.75	1.55
	Nechad et al., 2010	783	9	0.467	1.158	0.763	0.467	53.52	61.62	1.91
	Nechad et al., 2010	865	9	0.474	0.756	1.821	0.301	62.45	66.56	1.49
Sen2Cor	Nechad et al., 2010	665	8	0.019	-0.415	11.710	1.201	270.84	270.84	7.93
	Nechad et al., 2010	705	8	0.051	-0.766	13.840	1.347	309.73	309.73	9.07
	Nechad et al., 2010	740	8	0.335	-5.716	43.300	3.283	860.79	860.79	24.49
	Nechad et al., 2010	783	8	0.264	-6.189	47.891	4.212	973.11	973.11	28.16
	Nechad et al., 2010	865	8	0.181	-7.715	66.569	6.697	1477.11	1477.11	43.21
Polymer	Nechad et al., 2010	665	14	0.487	0.971	2.171	0.287	83.45	83.45	2.39
	Nechad et al., 2010	705	14	0.582	0.875	0.892	0.213	23.73	32.59	1.01
	Nechad et al., 2010	740	14	0.532	0.739	0.861	0.200	4.47	25.34	0.87
	Nechad et al., 2010	783	14	0.256	0.660	3.035	0.324	93.97	96.07	2.42
	Nechad et al., 2010	865	14	0.352	1.090	1.250	0.426	56.78	70.04	2.31

Regarding the S3-OLCI derived SPM for the Sado estuary, scatterplots are presented in Figure 5.17. Statistics are reported in Table 5.13. The number of match-ups ranged between 14 when processing the images with BPAC and 32 for C2RCC and Polymer. It can be seen (Figure 5.15) that the algorithms performed differently from the Tagus estuary. Processing the scenes for the Sado estuary, Polymer and C2RCC resulted to outperform the Level 2 standard processor (BPAC), attaining higher R² at all wavelengths being the highest R² = 0.7 at 779 nm waveband for both processors. Despite the lower R² values, BPAC processor showed overall smaller errors associated.

As expected, a general better correlation is found when deriving SPM from S3-OLCI sensor respect to S2-MSI sensor.

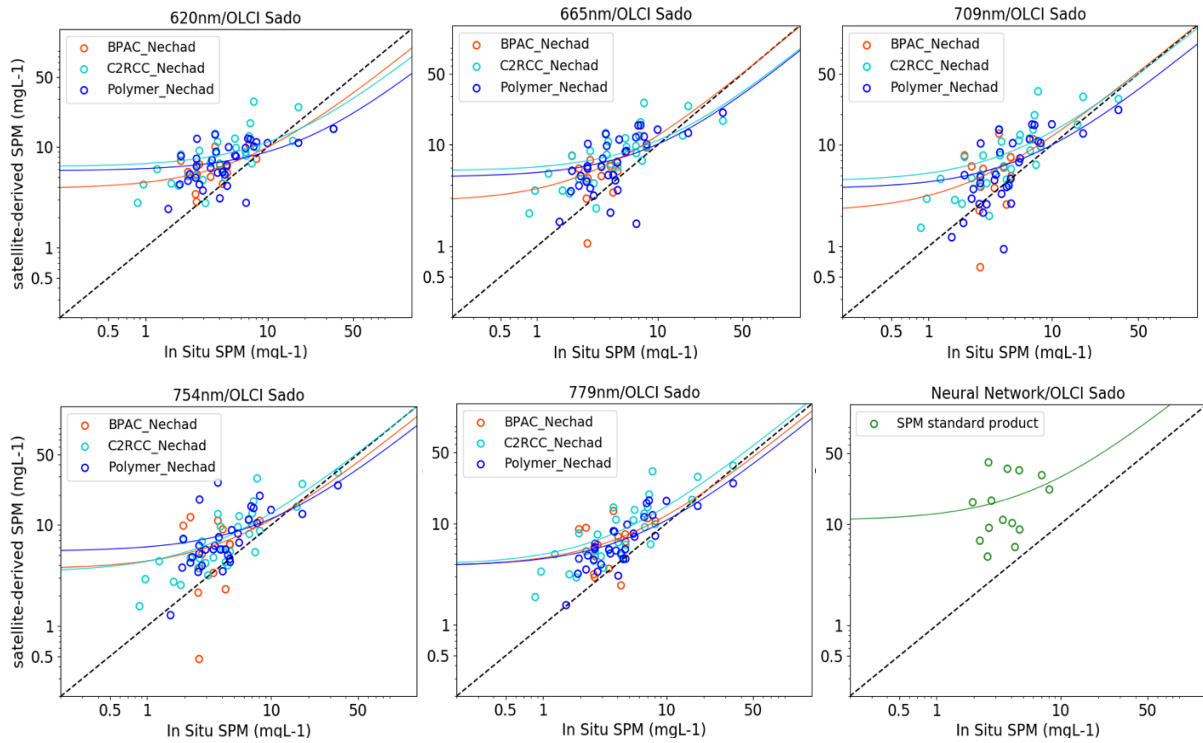


Figure 5.17 - Comparison of in situ and S3-OLCI-derived SPM estimates at different wavelengths for the Sado estuary in log space. The dashed black lines show the 1:1 relationship, the solid lines are the best linear fit to the data in log space.

Comparison of R^2 values among all methods shows that the lowest and most diverse values are found processing the scenes with BPAC, with values between 0.06 and 0.26.

Table 5.13 - Summary of statistics for SPM S3-OLCI match-ups for the Sado estuary. Numbers in bold show the best value of each statistics for all processors.

Processor	Algorithm	Wavelength (nm)	N	R^2	Slope	Intercept	stdErr	RPD (%)	APD (%)	RMSE
BPAC	Neuchad et al., 2010	-	14	0.07	1.825	10.784	1.885	396.59	396.59	17.84
	Neuchad et al., 2010	620	14	0.056	-0.164	6.854	0.179	74.98	75.73	2.98
	Neuchad et al., 2010	665	14	0.265	0.961	2.741	0.462	78.38	89.04	3.72
	Neuchad et al., 2010	709	14	0.260	1.002	2.168	0.487	65.53	82.67	3.54
	Neuchad et al., 2010	754	14	0.127	0.766	3.636	0.578	87.46	107.11	4.29
	Neuchad et al., 2010	779	14	0.194	0.824	3.751	0.484	94.59	100.29	4.11
C2RCC	Neuchad et al., 2010	620	32	0.289	0.483	6.377	0.138	676.45	680.57	59.78
	Neuchad et al., 2010	665	32	0.387	0.553	5.517	0.127	118.58	124.97	6.74
	Neuchad et al., 2010	709	32	0.525	0.911	4.358	0.158	98.69	105.10	6.01
	Neuchad et al., 2010	754	32	0.667	0.971	3.403	0.125	96.86	101.63	6.74
	Neuchad et al., 2010	779	32	0.668	1.082	3.879	0.139	108.43	109.46	6.54
Polymer	Neuchad et al., 2010	620	32	0.329	0.321	5.799	0.082	77.17	88.42	4.79
	Neuchad et al., 2010	665	32	0.477	0.535	4.809	0.101	56.66	73.65	4.49
	Neuchad et al., 2010	709	32	0.521	0.629	3.696	0.110	27.32	66.67	4.31
	Neuchad et al., 2010	754	32	0.355	0.607	5.473	0.129	113.94	118.87	6.07
	Neuchad et al., 2010	779	32	0.684	0.694	3.785	0.078	66.54	70.75	3.80

INLAND WATERS

For the inland waters no *in situ* radiometric data were available for the AC processors test. The same approach conducted for the Sado estuary has been applied for the reservoirs and thus all the processors and algorithms have been tested.

Despite the small amount of coincident S2-MSI overpasses to *in situ* samplings, a preliminary match-up exercise has been attempted considering the 5 reservoirs as a whole water body due to the small amount of data available when considering each reservoir separately. Scatterplots of the *in situ* versus satellite-derived SPM for the inland waters are presented in Figure 5.18 with the corresponding statistics in Table 5.14.

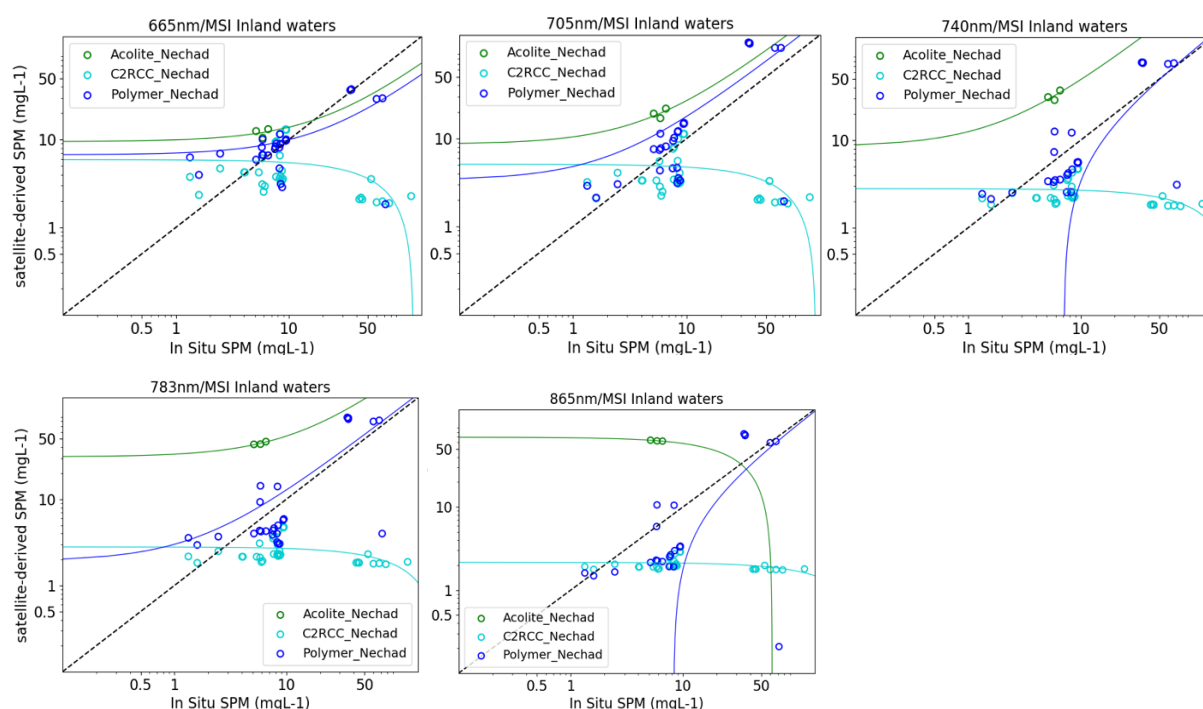


Figure 5.18 - Comparison of *in situ* and S2-MSI derived SPM at different wavelengths for inland waters. The black dashed lines show the 1:1 relationship. The solid lines represent the best fit to the data in log space. All the data available from the different reservoirs have been used. The corresponding error statistics are shown in Table 5.14.

Analysing the statistical results in Table 5.14, it can be noted that C2RCC is the least performing processor achieving the lowest R^2 values and highest errors associated. Acolite processor achieved the highest R^2 values especially at 783 nm and 865 nm ($R^2_{865nm}=0.9$). However, such results should not be considered statistically significant since only three datapoints were available for the statistics, and it can be seen in the graphs that the values for these particular wavelengths are in fact far off and overestimating the *in situ* results.

Results from Polymer processor suggest similar performances compared to the other study areas under investigation, with similar R^2 values and errors. The highest correlations have been found at 783 nm ($R^2_{783nm}=0.5$) unlike the estuaries where the highest R^2 values have been found at smaller wavelengths (705 nm). Again, such results should be interpreted carefully since all the waterbodies have been considered as a whole due to the lack of data points per single reservoirs.

Table 5.14 - Summary of statistics for SPM S2-MSI match-ups for the inland waters. All the water bodies have been considered as a whole. Numbers in bold show the best value of each statistics for all processors.

Processor	Algorithm	Wavelength (nm)	N	R ²	Slope	Intercept	StdErr	RPD (%)	APD (%)	RMSE
Acolite	Nechad et al., 2010	665	3	0.049	0.435	9.535	1.903	108.11	108.11	6.333
	Nechad et al., 2010	705	3	0.293	1.830	8.601	2.838	231.61	231.61	13.573
	Nechad et al., 2010	740	3	0.472	4.081	8.451	4.316	454.28	454.28	26.678
	Nechad et al., 2010	783	3	0.795	2.295	31.037	1.162	665.11	665.11	38.639
	Nechad et al., 2010	865	3	0.929	-1.110	69.241	0.304	983.52	983.52	56.899
C2RCC	Neural Network	-	32	0.121	-0.165	16.410	0.081	75.68	134.50	35.419
	Nechad et al., 2010	665	32	0.139	-0.046	5.935	0.035	-25.77	59.09	33.250
	Nechad et al., 2010	705	32	0.126	-0.037	5.108	0.017	-36.11	55.83	33.290
	Nechad et al., 2010	740	32	0.125	-0.011	2.796	0.005	-61.69	66.61	33.522
	Nechad et al., 2010	783	32	0.122	-0.011	2.798	0.005	-61.70	66.61	33.519
	Nechad et al., 2010	865	32	0.125	-0.004	2.156	0.002	-68.68	72.10	33.625
Polymer	Nechad et al., 2010	665	27	0.359	0.325	6.725	0.086	21.41	49.54	16.614
	Nechad et al., 2010	705	27	0.470	1.446	3.366	0.303	43.60	72.29	33.666
	Nechad et al., 2010	740	27	0.376	1.142	-8.082	0.294	-87.91	139.26	30.051
	Nechad et al., 2010	783	27	0.494	1.090	1.913	0.220	12.16	66.58	22.365
	Nechad et al., 2010	865	27	0.328	1.003	-8.254	0.286	-107.12	139.39	29.240

5.2.3 Water-quality algorithms comparison: turbidity

The same approach used for the SPM algorithms test have been adopted for the turbidity retrieval. C2RCC and Polymer have been chosen from the AC test as the two best performing processors to evaluate turbidity retrieval algorithms from S2-MSI imagery in the Tagus area. For Sado estuary and the inland water bodies, all the processors have been tested since no *in situ* radiometric data are available for AC test.

Regarding the S3-OLCI, all the three processors have been used for the turbidity retrieval test.

The turbidity retrieval algorithms tested here are the Nechad et al., 2010 applied to several bands and Dogliotti et al., 2015 applied to 665 nm band. For a more exhaustive evaluation of the above-mentioned turbidity algorithms, the *in situ* radiometric measurements performed in the Tagus estuary allowed to directly test the above-mentioned algorithms with *in situ* ρ_w .

TAGUS ESTUARY

In Figure 5.19 are presented the results of comparison between the *in situ* and the S2-MSI estimates. Table 5.15 summarizes the error statistic for the data sets presented in Figure 5.19.

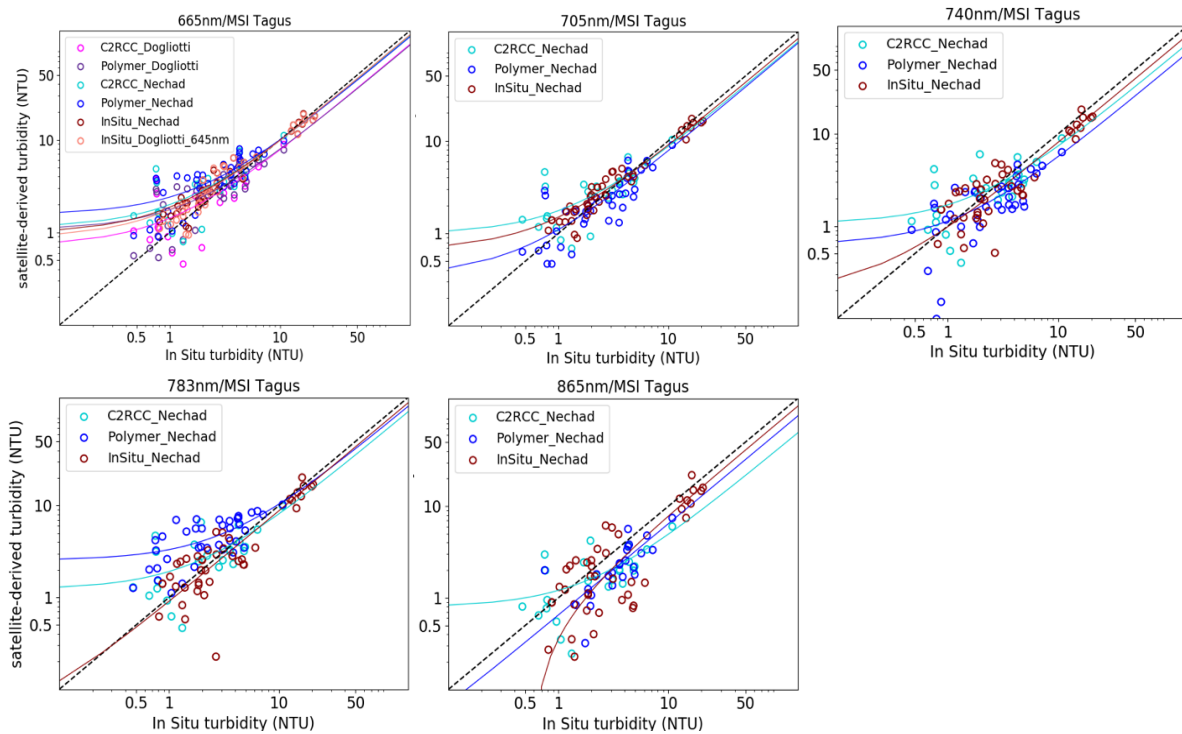


Figure 5.19 - Comparison of *in situ* and S2-MSI derived turbidity at different wavelengths. The black dashed lines show the 1:1 relationship. The solid lines represent the best fit to the data in log space. The corresponding error statistics are shown in Table 5.15.

From the scatterplots in Figure 5.19 the highest correlation with *in situ* measurements have been found processing the satellite data with Polymer and Nechad et. Al., 2010 at 705 nm ($R^2=0.76$; APD=24.023%; RMSE=12,073 NTU). Similar results were found applying the same turbidity algorithm to C2RCC processor at 665 nm ($R^2=0.75$; APD=83%; RMSE=1,43 NTU).

Dogliotti et al. 2015, algorithm also showed similar results and a good correlation with both processors ($R^2_{C2RCC}=0.75$; $R^2_{Polymer}=0,72$) with smaller errors associated (RMSE_{C2RCC}=1.18 NTU; RMSE_{Polymer}=1.17 NTU).

As well as the SPM product, turbidity results are reinforced by the application of such algorithms to *in situ* ρ_w . The best relationships are found at 665 nm and 705 nm. The *in situ* ρ_w allowed to test the Dogliotti et. al. (2015) algorithm at its original wavelength (645 nm) showing significantly high correlation with *in situ* turbidity ($R^2=0.96$) and small errors associated (RMSE=1.30 NTU). The algorithm have also been tested with the *in situ* 665 nm band presenting similar R^2 despite higher errors.

Summary of the statistics for the turbidity match-ups for the Tagus area are presented in Table 5.15. Results from all the processors including Acolite and C2RCC are shown in Table A 2.

Table 5.15 - Summary of statistics for turbidity S2-MSI match-ups for the Tagus estuary. Numbers in bold show the best value of each statistics for all processors.

Processor	Algorithm	Wavelength (nm)	N	R ²	Slope	Intercept	stdErr	RPD (%)	APD (%)	RMSE
In situ ρ_w	Dogliotti et al., 2015	645	45	0.958	0.734	0.584	0.023	20.108	27.439	1.30
	Dogliotti et al., 2015	665	45	0.956	0.892	0.886	0.029	-28.72	31.33	5.20
	Nechad et al., 2009	665	45	0.959	0.839	0.978	0.028	26.421	31.978	1.31
	Nechad et al., 2009	705	45	0.965	0.839	0.66	0.02	9.582	22.322	1.32
	Nechad et al., 2009	740	45	0.902	0.792	0.19	0.04	-8.243	41.986	2.11
	Nechad et al., 2009	783	45	0.901	0.873	0.03	0.04	-6.029	42.166	1.93
	Nechad et al., 2009	865	45	0.778	0.826	-0.47	0.07	-28.567	60.107	3.06
C2RCC	Dogliotti et al., 2015	665	24	0.751	0.708	0.716	0.088	26.594	58.852	1.18
	Nechad et al., 2009	665	24	0.750	0.869	1.129	0.106	72.039	83.020	1.43
	Nechad et al., 2009	705	24	0.723	0.774	0.985	0.102	55.438	74.994	1.29
	Nechad et al., 2009	740	24	0.573	0.633	1.067	0.116	40.152	74.129	1.54
	Nechad et al., 2009	783	24	0.566	0.689	1.225	0.128	57.380	82.903	1.62
	Nechad et al., 2009	865	24	0.541	0.416	0.789	0.081	-1.950	60.650	1.85
Polymer	Dogliotti et al., 2015	665	38	0.717	0.689	1.067	0.072	27.662	47.895	1.170
	Nechad et al., 2009	665	38	0.717	0.846	1.558	0.088	71.424	47.096	1.643
	Nechad et al., 2009	705	38	0.766	0.751	0.346	0.069	0.935	24.023	12.073
	Nechad et al., 2009	740	38	0.666	0.505	0.627	0.059	-11.036	46.549	1.563
	Nechad et al., 2009	783	38	0.522	0.783	2.534	0.124	119.773	122.655	2.550
	Nechad et al., 2009	865	25	0.694	0.643	0.005	0.089	-31.094	47.538	1.814

Regarding the comparison between S3-OLCI and *in situ* measurements, scatterplots are presented in Figure 5.20. Compared to S2-MSI turbidity results, the OLCI sensor shows an overall higher correlation with all processors (Table 5.16). The highest R² value correspond to Nechad algorithm applied to Polymer processor at 620 nm (R²=0.887; APD=13%; RMSE=0.66 NTU). However, different wavelengths showed similar correlation (Table 5.16) despite higher errors.

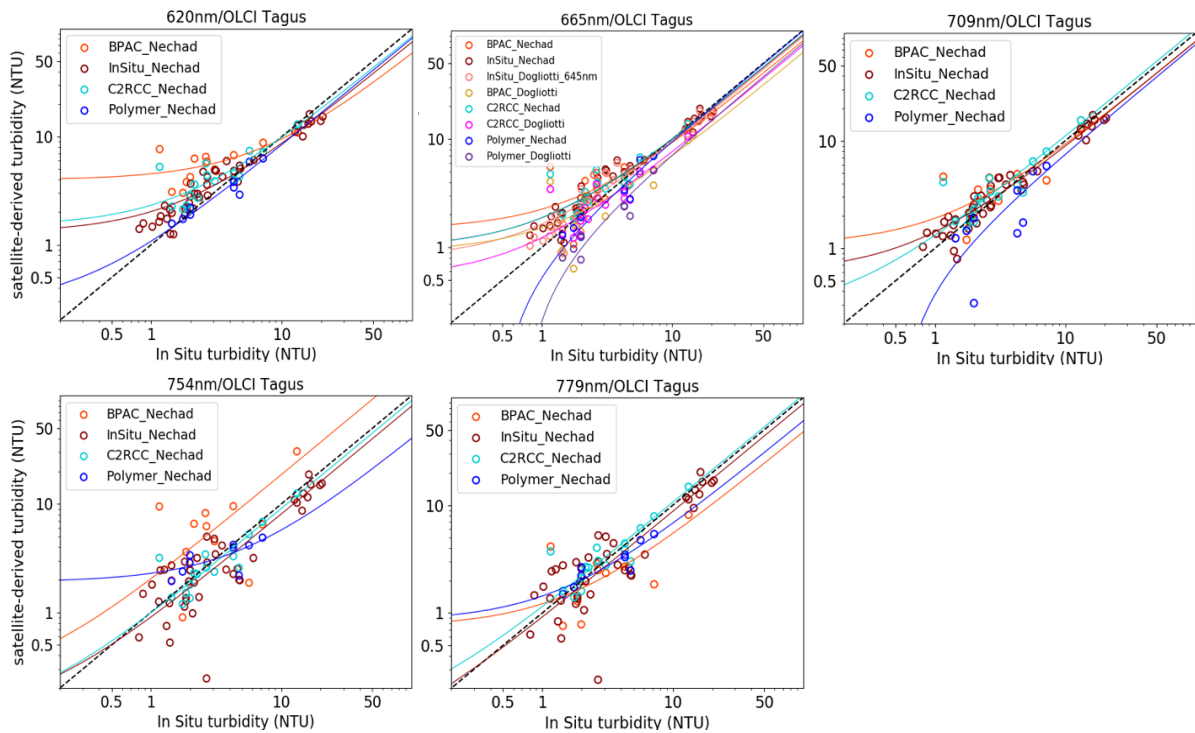


Figure 5.20 - Comparison of in situ and S3-OLCI-derived turbidity at different wavelengths. The dashed black lines show 1:1 relationship, the solid lines are the best linear fit to the data in log space. The corresponding error statistics are shown in Table 5.16.

Comparing the three processors at different wavelengths (Figure 5.20), all the processors performed quite well. In Table 5.16 it can be seen that BPAC can be considered as the least performing processor with the lower R^2 values. C2RCC and Polymer show 4 out of the 6 wavelengths under investigation with $R^2 > 0.85$. The best performing wavelengths resulted to be the 665 nm and 709 nm which is also confirmed by the application of the two semi-analytical algorithms (Nechad (2010) and Dogliotti (2015)) to *in situ* ρ_w . The two turbidity algorithms performed similarly as expected.

C2RCC presented general higher values of RMSE when compared to the other two processors.

It can also be noticed that the 754 nm wavelength resulted to be in general the least performing overall for all the three processors including the *in situ* ρ_w . Unlike BPAC and C2RCC, Polymer seems to have good performances at higher wavelengths for both sensors, S2-MSI (865 nm) and S3-OLCI (779 nm).

Summary of statistics for turbidity S3-OLCI match-ups for the Tagus estuary are presented in Table 5.16.

Table 5.16 - Summary of statistics for turbidity S3-OLCI match-ups for the Tagus estuary. Numbers in bold show the best value of each statistics for all processors.

Processor	Algorithm	Wavelength (nm)	N	R ²	Slope	Intercept	stdErr	RPD (%)	APD (%)	RMSE
<i>In situ</i> pw	Dogliotti et al., 2015	645	44	0.957	0.865	0.781	0.03	20.108	27.439	1.30
	Dogliotti et al., 2015	665	44	0.956	0.892	0.886	0.029	-28.72	31.33	5.20
	Nechad et al., 2009	620	44	0.954	0.742	1.286	0.02	22.287	31.345	1.76
	Nechad et al., 2009	665	44	0.958	0.893	0.985	0.03	25.555	31.238	1.29
	Nechad et al., 2009	709	44	0.964	0.345	0.590	0.02	6.145	21.764	1.35
	Nechad et al., 2009	754	44	0.889	0.797	0.108	0.04	-9.964	46.027	2.23
	Nechad et al., 2009	779	44	0.897	0.873	0.04	0.04	-4.856	44.222	1.96
BPAC	Dogliotti et al., 2015	665	12	0.764	0.614	0.903	0.107	6,033	49,429	1,76
	Nechad et al., 2009	620	12	0.645	0.557	3.972	0.130	128,897	131,759	3,09
	Nechad et al., 2009	665	12	0.760	0.783	1.468	0.139	48,755	62,226	1,75
	Nechad et al., 2009	709	12	0.803	0.825	1.078	0.129	37,551	51,145	1,53
	Nechad et al., 2009	754	12	0.651	1.845	0.198	0.407	125,339	144,602	6,12
	Nechad et al., 2009	779	12	0.601	0.474	0.743	0.122	-12,615	57,137	2,43
C2RCC	Dogliotti et al., 2015	665	18	0.869	0.714	0.519	0.069	-37,031	53,951	4,23
	Nechad et al., 2009	620	18	0.821	0.834	1.434	0.097	-6,968	53,188	4,08
	Nechad et al., 2009	665	18	0.867	0.911	0.985	0.088	-9,282	50,428	3,99
	Nechad et al., 2009	709	18	0.856	1.096	0.387	0.112	-1,296	51,389	3,88
	Nechad et al., 2009	754	18	0.572	0.932	0.486	0.201	7,753	66,368	4,32
	Nechad et al., 2009	779	18	0.581	1.096	0.539	0.232	25,707	72,316	4,58
Polymer	Dogliotti et al., 2015	665	9	0.874	0.762	-0.554	0.108	-55,321	55,321	1,83
	Nechad et al., 2009	620	9	0.887	0.817	0.261	0.110	-7,386	13,165	0,66
	Nechad et al., 2009	665	9	0.876	0.991	-0.467	0.140	-29,820	31,728	1,16
	Nechad et al., 2009	709	9	0.697	0.788	-0.417	0.196	-45,557	45,557	1,89
	Nechad et al., 2009	754	9	0.554	0.384	1.908	0.130	29,827	48,856	1,66
	Nechad et al., 2009	779	9	0.835	0.598	0.836	0.100	1,332	25,484	1,06

SADO ESTUARY

For the turbidity algorithms test in the Sado estuary, the same approach used for the SPM has been applied. The AC processors Acolite, C2RCC, Polymer and Sen2Cor have been tested in combination with the Nechad algorithm at different wavelengths and Dogliotti using the 665 nm waveband.

The number of match-ups ranged between 6 and 8 depending on the AC processor applied. Acolite and Sen2Cor yielded 6 match-ups while C2RCC resulted to attain the most match-ups for this region (*i.e.* 8) (Table 5.17).

Scatterplots between MSI-derived turbidity values for the different algorithms and wavelengths and *in situ* turbidity values for the Sado estuary are presented in Figure 5.9. Corresponding statistics are reported in Table 5.17.

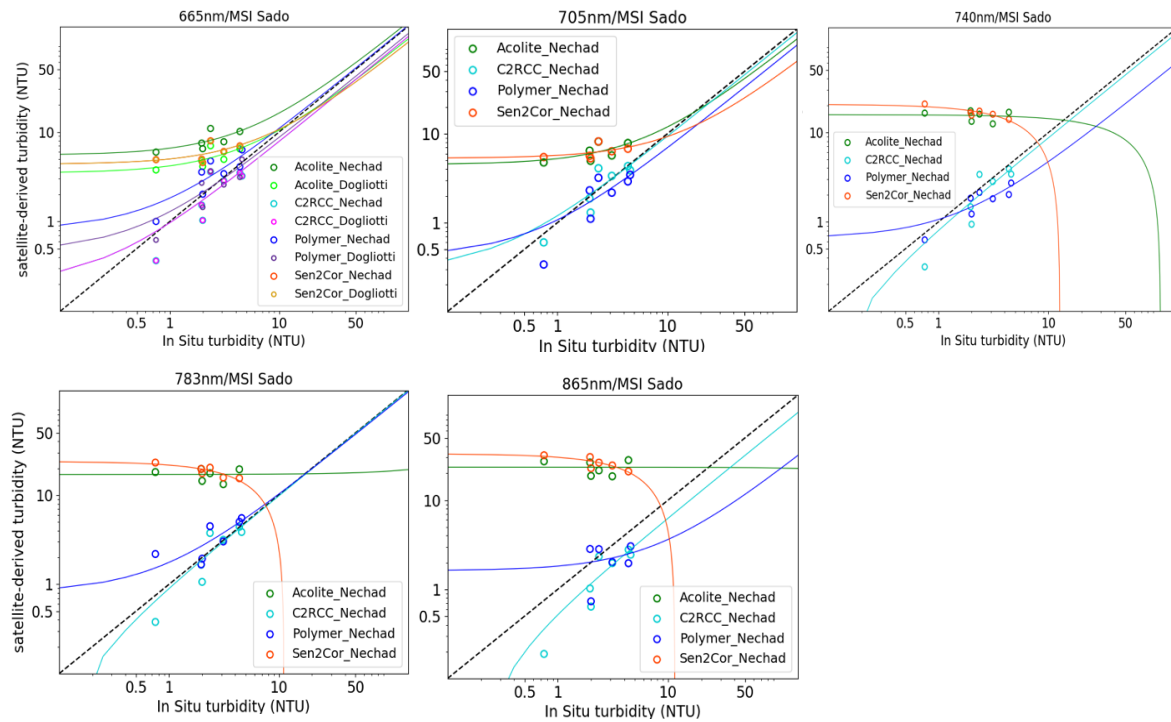


Figure 5.21 - Comparison of *in situ* and S2-MSI-derived turbidity estimates at different wavelengths. Data represent matchups for the concurrent satellite and field measurements collected during several research projects. The dashed black lines show 1:1 relationship, the solid lines represent the best linear fit to the data in log space. The corresponding error statistics are shown in Table 5.17.

Examining Figure 5.21, which shows the estimated (S2-MSI) and measured (*in situ*) turbidity, it can be seen that, again, the processors can be divided into two groups, one includes Acolite and Sen2Cor and the other one with C2RCC and Polymer. As demonstrated with the SPM results and with the Tagus estuary case-study, there are clear differences between the two groups, with the latter one (C2RCC and Polymer) outperforming the Acolite and Sen2Cor processors. Comparison of the estimated and observed turbidity for each processor and algorithm (Figure 5.21), shows that Acolite and Sen2Cor generally overestimate turbidity at all wavelengths, with a progressive increase of the overestimation at higher wavelengths (740, 783, 865 nm). This is further supported by the RMSEs and APDs (APD > 100% for both processors at all wavelengths).

When comparing the Nechad and Dogliotti algorithms, very similar results have been found, but with general lower errors values (APD, RMSE) when processing with Dogliotti et al, 2015. It should be noticed however, that the comparison of these two algorithms has been performed solely at 665 nm waveband.

Examining Table 5.17 which shows the statistics of MSI-derived turbidity for the Sado estuary, it can be seen that C2RCC and Polymer had the highest R^2 for all bands except the Polymer 865 nm which gave low R^2 . Polymer performed similarly to C2RCC but with general lower R^2 values.

Table 5.17 - Summary of statistics for turbidity S2-MSI match-ups for the Sado estuary. Bolded numbers show the best value of each statistics for all processors.

Processor	Algorithm	Wavelength (nm)	N	R ²	Slope	Intercept	stderr	RPD (%)	APD (%)	RMSE
Acolite	Dogliotti et al., 2015	665	6	0.437	0.699	3.482	0.396	159.22	159.22	2.91
	Nechad et al., 2009	665	6	0.440	1.075	5.514	0.606	307.37	307.37	5.86
	Nechad et al., 2009	705	6	0.396	0.741	4.506	0.457	219.57	219.57	4.02
	Nechad et al., 2009	740	6	0.008	-0.151	15.825	0.829	770.89	770.89	13.23
	Nechad et al., 2009	783	6	0.0005	0.015	17.052	1.084	859.68	859.68	14.90
	Nechad et al., 2009	865	6	0.0004	-0.005	23.415	1.784	1243.14	1243.14	21.38
C2RCC	Dogliotti et al., 2015	665	8	0.659	0.766	0.202	0.246	-18.29	33.09	0.88
	Nechad et al., 2009	665	8	0.659	0.766	0.202	0.246	-18.29	33.09	0.88
	Nechad et al., 2009	705	8	0.706	0.909	0.287	0.262	0.674	22.38	0.76
	Nechad et al., 2009	740	8	0.751	0.880	-0.080	0.226	-19.53	32.09	0.78
	Nechad et al., 2009	783	8	0.762	0.988	-0.091	0.246	-9.48	26.97	0.72
	Nechad et al., 2009	865	8	0.775	0.638	-0.121	0.153	-44.59	44.59	1.28
Sen2Cor	Dogliotti et al., 2015	665	6	0.329	0.635	4.358	0.453	204.21	204.21	3.64
	Nechad et al., 2009	665	6	0.329	0.635	4.358	0.453	204.21	204.21	3.64
	Nechad et al., 2009	705	6	0.198	0.398	5.3155	0.400	230.87	230.87	4.01
	Nechad et al., 2009	740	6	0.751	-1.625	20.704	0.466	897.00	897.00	14.67
	Nechad et al., 2009	783	6	0.776	-2.133	23.838	0.571	1015.24	1015.25	16.66
	Nechad et al., 2009	865	6	0.669	-2.861	33.080	-0.818	1452.94	1452.94	24.20
Polymer	Dogliotti et al., 2015	665	7	0.651	0.826	0.463	0.270	1.44	27.29	0.80
	Nechad et al., 2009	665	7	0.651	1.018	0.809	0.332	36.95	38.78	1.28
	Nechad et al., 2009	705	7	0.635	0.655	0.419	0.221	-19.29	34.44	0.93
	Nechad et al., 2009	740	7	0.700	0.407	0.657	0.119	-29.43	29.43	1.27
	Nechad et al., 2009	783	7	0.682	0.946	0.816	0.288	42.21	48.22	1.07
	Nechad et al., 2009	865	7	0.073	0.200	1.619	0.354	-20.60	41.92	1.41

Regarding the S3-OLCI derived turbidity, scatterplots of the correlations with the *in situ* data are presented in Figure 5.22, with the corresponding statistics in Table 5.18.

Analyzing the Table 5.18, it is noticeable that all the processors and algorithms gave contrasting results for the Sado estuary region returning overall lower R² values compared to S2-MSI retrieved data. All the three processors performed similarly, with the highest R² value achieved by Polymer and Nechad algorithm at 779 nm waveband.

The 754 nm waveband turned out to be the least performing waveband for all the processors (as noticed for the Tagus estuary) except for C2RCC. It is interesting to notice that the 779 nm waveband performed significantly good for all the processors except for BPAC, which presented the worse correlations and errors at 754 nm and 779 nm. However, more data are needed for more meaningful results, as well as the test of all the available wavelengths.

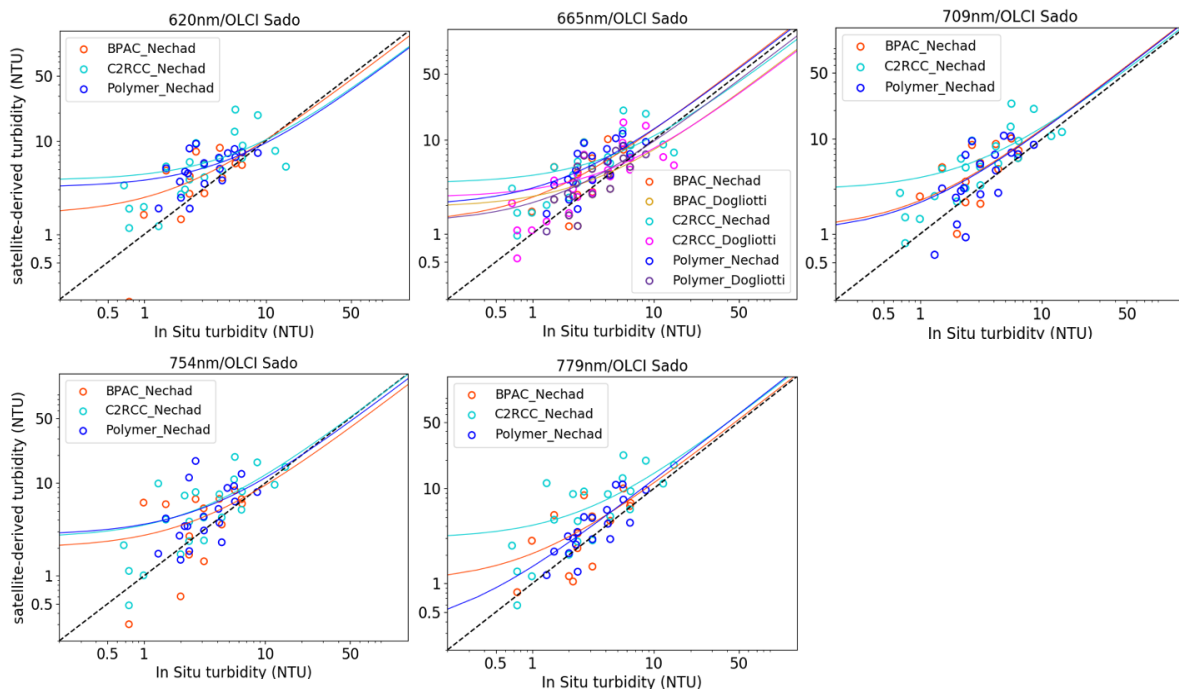


Figure 5.22 - Comparison of in situ and S3-OLCI-derived turbidity estimates at different wavelengths. Data represent matchups for the concurrent satellite and field measurements collected during several research projects. The dashed black lines show 1:1 relationship, the solid lines is the best linear fit to the data in log space. The corresponding error statistics are shown in Table 5.18.

Comparing the Turbidity retrieval algorithms for the different processors, again not significant differences have been found between Dogliotti et al, 2015 and Nechad et al., 2010. As demonstrated with results derived from S2-MSI data, Dogliotti algorithm resulted to be the best performing when considering the errors, indeed, data derived with such algorithm showed the lowest RMSE values with all the AC processors (RMSE values highlighted in bold in Table 5.18).

Table 5.18 - Summary of statistics for turbidity S3-OLCI match-ups for the Sado estuary. Numbers in bold show the best value of each statistics for all processors.

Processor	Algorithm	Wavelength (nm)	N	R ²	Slope	Intercept	stderr	RPD (%)	APD (%)	RMSE
BPAC	Dogliotti et al., 2015	665	14	0.367	0.773	1.255	0.281	3.50	48.90	2.01
	Nechad et al., 2009	620	14	0.426	0.927	1.229	0.298	34.84	60.82	2.08
	Nechad et al., 2009	665	14	0.445	1.156	1.285	0.372	54.05	78.82	2.85
	Nechad et al., 2009	709	14	0.492	1.194	0.877	0.336	47.85	72.05	2.56
	Nechad et al., 2009	754	14	0.0002	0.017	6.280	1.180	151.77	184.86	8.08
	Nechad et al., 2009	779	14	0.004	-0.831	12.401	3.300	309.42	329.71	21.6
C2RCC	Dogliotti et al., 2015	665	24	0.308	0.611	1.966	0.195	-2.11	59.54	3.33
	Nechad et al., 2009	620	24	0.225	0.708	3.148	0.280	42.84	82.59	4.44
	Nechad et al., 2009	665	24	0.308	0.810	2.835	0.259	40.85	79.07	4.12
	Nechad et al., 2009	709	24	0.410	1.088	2.325	0.278	47.03	77.84	4.47
	Nechad et al., 2009	754	24	0.472	1.01	2.101	0.227	51.88	88.33	4.13
	Nechad et al., 2009	779	24	0.478	1.194	2.424	0.265	77.70	106.09	4.92
Polymer	Dogliotti et al., 2015	665	19	0.493	0.835	1.300	0.205	3.50	48.90	1.83
	Nechad et al., 2009	620	19	0.291	0.635	3.161	0.240	51.15	64.72	2.42
	Nechad et al., 2009	665	19	0.493	1.107	1.953	0.272	40.34	70.42	2.79
	Nechad et al., 2009	709	19	0.434	1.133	1.013	0.313	34.80	64.05	2.74
	Nechad et al., 2009	754	19	0.147	0.865	2.729	0.503	80.10	90.82	4.01
	Nechad et al., 2009	779	19	0.577	1.211	0.293	0.251	25.09	40.38	1.99

INLAND WATERS

Regarding the inland waters, turbidity measurements have been performed only in two campaigns (Table 4.1) and unfortunately no turbidity match-ups are available for the sampling period.

Chapter 6: Discussion

6.1 *In situ* data

6.1.1 Suspended Particulate Matter and Turbidity

Both the estuaries and inland waters under investigation in the present study have been characterized by their *in situ* SPM and turbidity ranges and the fraction of organic matter that composes the SPM samples.

The estuaries under investigation are both characterized by a significant spatial variability of SPM and turbidity Figure 6.1. The mouth of both estuaries is characterized by clear oceanic waters that enters the estuaries through the inlet carrying a type of water with low ranges of turbidity and SPM and with samples characterized by a high percentage in SPOM and low fraction of mineral sediments. The percentage in SPOM in those areas showed to increase with the rising tide, suggesting that a significant fraction of the SPOM at the inlet of the estuaries comes from the ocean and it is carried by the tides. In turn, the inner basins are depicted by a type of water more loaded in suspended sediment due to a stronger influence of the rivers discharges, which results in higher values of turbidity and SPM. Also, the concentration of SPOM (mgL^{-1}) tends to increase moving towards from the inlet towards to the inner region of both estuaries, even if the organic component relative to the inorganic is higher in the outer stations Figure 6.2. The SPOM distribution in the estuaries under investigation may be mainly associated to phytoplankton cells distribution (Alt-Epping *et al.*, 2007) due to the river discharge of nutrient-rich waters (Milliman and Meade, 1983), with higher values close to the input source. This assumption is also reinforced by the analysis of the tidal influence on the SPOM concentration, demonstrating that while the inorganic fraction varies significantly with the tides, the organic part remains substantially constant within a tidal cycle with higher values in the inner bay.

Because of this variability, three different regions have been defined within the estuaries according to their SPM and turbidity spatial variability: the mouth (outer region), the middle region (mid) and the inner region (inn). It should be here referred that the spatial distribution of the sampling stations may not be representative of each region of the estuaries.

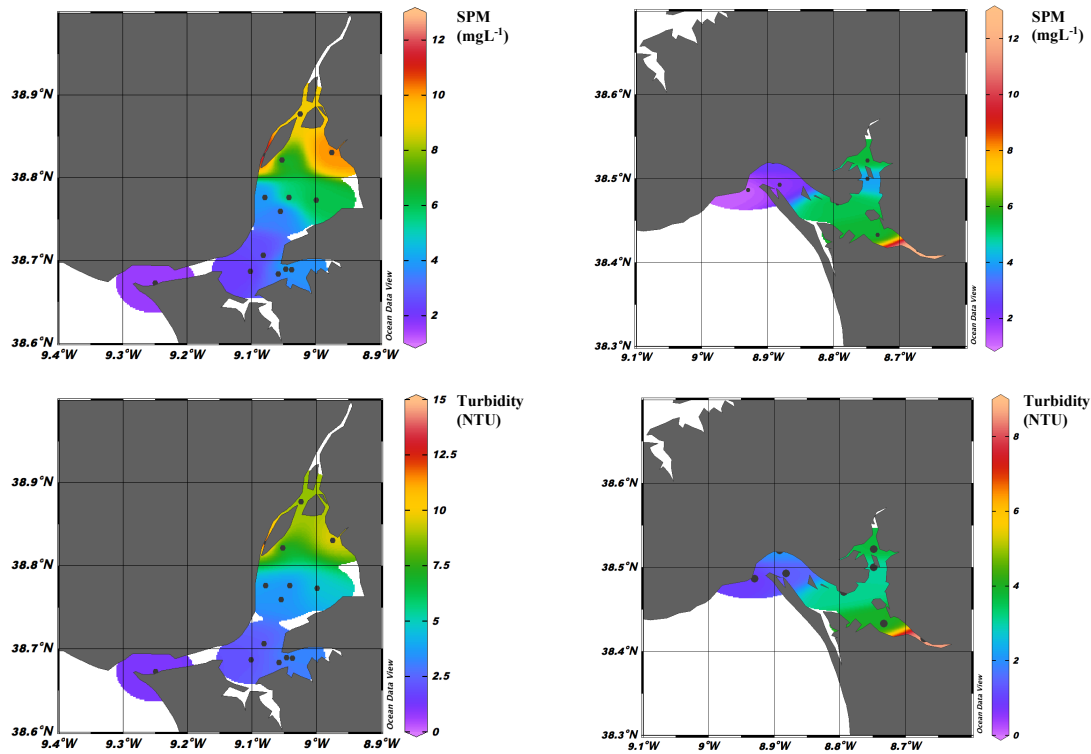


Figure 6.1 - In situ SPM and turbidity spatial variability for the two estuaries under investigation (Tagus estuary on the left and Sado estuary on the right). Maps produced using the mean values of samples collected at similar tide conditions for each sampling point.

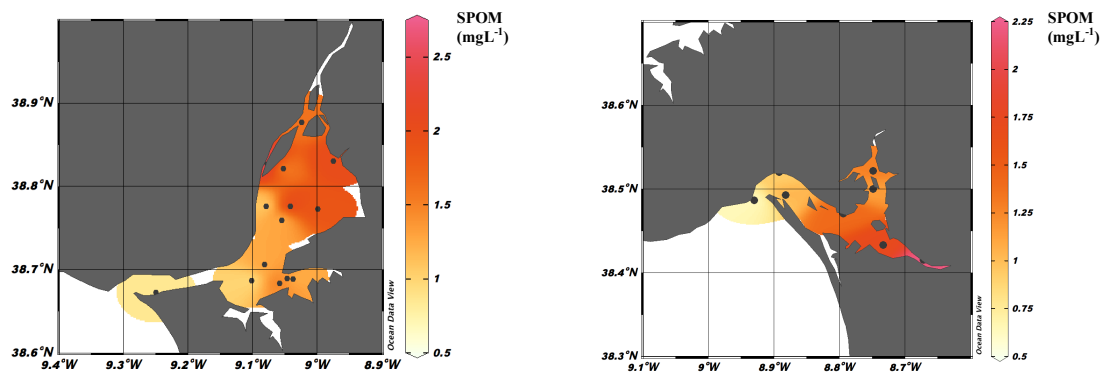


Figure 6.2 - In situ Suspended Organic Particulate Matter (SPOM) spatial variability for the two estuaries under investigation (Tagus estuary on the left and Sado estuary on the right). Maps produced using the mean values of samples collected at similar tide conditions for each sampling point.

Different approaches based on the SPM and turbidity parameters, as well as the content of organic matter, have been applied separately for each region for a better understanding of the main drivers for the variability in the relationship between these two parameters.

The SPM:T ratio variability have been studied spatially (by comparing the general results of the three regions), temporally (samples have been separated in 4 classes corresponding to the seasons), by analysing the tidal influence (just at mid and outer stations), and the fraction of organic matter (just at mid and outer stations).

For both estuaries, the highest correlations between SPM and T are found at mid and outer stations, suggesting a better correlation where there is a stronger influence of oceanic water respect to riverine

waters, which also showed higher range of variability. This might be explained by the distribution of the SPOM concentration, which is significantly higher in the inner bay of the estuary respect to the mouth Figure 6.2. If we assume that most of the organic fraction in the SPM samples is due to phytoplankton cells, our results on the SPOM distribution can be reinforced by previous works on the phytoplankton distribution in the Tagus estuary where the highest concentrations of Chl-*a* were also found in the inner bay (Gameiro *et al.*, 2004; Gameiro, Cartaxana and Brotas, 2007).

However, for the Sado estuary the SPM:T ratio difference between the three regions is almost negligible. More information about the variable composition of suspended matter in the samples (*i.e.* clay minerals, detritus, phytoplankton and other organic compounds) and the dissolved fraction in the water samples might help to understand what the main causes of the ratio variability are.

Regarding the seasonal variation of the relationship between SPM and turbidity, results provide no conclusive evidence for a seasonal pattern on the ratio variability. In fact, the relationship was expected to vary seasonally due to the seasonal variability in the nature of the particles, from small mineral particles during winter to phytoplankton cells, aggregates and flocs in summer (Jafar-Sidik *et al.*, 2017). However, in both estuaries a higher correlation has been found during spring and summer respect to fall and winter seasons. Nevertheless, the small amount of data available and the limited information on biogeochemistry of the areas do not allow to draw further conclusions about the seasonality and spatial variability of this ratio.

Regarding the inland waters, a very small amount of turbidity data was available for a thorough analysis. However, a preliminary evaluation of the SPM:T ratio over inland waterbodies have been attempted showing significantly lower correlations compared to the transitional waters. That may be explained by the percentage in suspended organic matter which is significantly higher in all the 5 reservoirs under investigation respect to the estuaries Figure 6.3.

A more comprehensive dataset and more information about the biogeochemistry and optical types of the waters under study is needed to perform a more in-depth analysis.

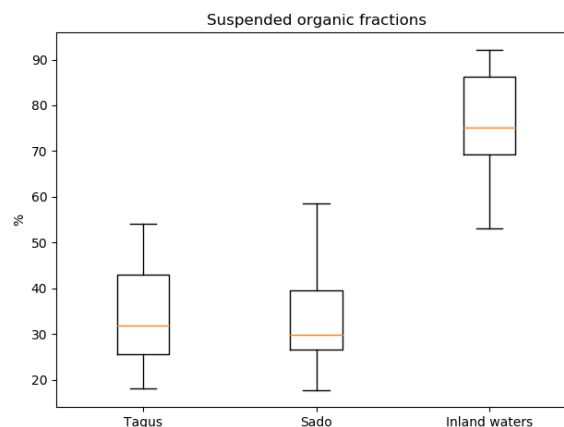


Figure 6.3 - Boxplot representing the suspended organic percentages for each study area.

Comparing the three study areas (Tagus and Sado estuaries and inland waters) a pattern related to the SPOM concentration has been noticed. The R^2 of the SPM:T ratios seems to decrease with higher concentrations of organic matter in all the study areas. In the estuaries, a higher correlation is found at outer and mid stations, where the SPOM concentration is lower, and the inland waterbodies (with significantly higher SPOM) showed a worse correlation respect to the transitional waters. However, in order to test this hypothesis a larger dataset is needed, comprising samples collected during different

years to study a possible seasonal variation, and the biogeochemical dynamics in the study areas, such as characterization of the algal particles in the SPM samples, backscattering (which is highly correlated to turbidity and particle size (Dogliotti *et al.*, 2015; Jafar-Sidik *et al.*, 2017) and type of sediment distribution.

6.1.2 *Radiometric measurements*

Regarding the radiometric measurements performed in the Tagus estuary, marked differences have been noticed between the two campaigns (Figure 5.12), being the first one conducted at the mouth of the estuary and the second one in the middle region. Spectra showed mainly two distinct shapes at both stations, related to the tide conditions at the sampling time. In both cases, lower reflectance corresponds to high tide conditions, where the water is characterized by low ranges of turbidity and suspended sediments that result in a smaller reflectance signal.

In the spectra corresponding to the second campaign (middle basin), a higher amplitude in the reflectance signal has been noticed related to the tidal condition, but with similar spectral shape. Also, the spectra measured at the mid region have clearly depicted the higher levels of turbidity and suspended solids as indicates the significantly higher values in the NIR region.

On the other hand, the spectra measured at mouth of the estuary (first campaign) showed a smaller variability but two distinct shapes depending on the tidal state. This can be explained by the dissimilarities in the characteristics of the water between the two tides. At the mouth of the estuary this discrepancy is more evident, especially in the region ~ 670 nm (where a trough in the reflectance due to chlorophyll absorption characteristic of phytoplankton is expected; a detailed description of bio-optical properties of phytoplankton is available in Matthews, 2017) where the high tide spectra are flatter due to lower organic matter in the water that can be associated to lower Chl-*a* concentrations. Spectra corresponding to low tide conditions at the mouth of the estuary present similar shape to the spectra measured at the mid region (at both tide conditions). In the middle region of the estuary, the above-mentioned trough at ~ 670 nm is evident with both tide conditions (explained by a higher concentration of SPOM and probably more phytoplankton signal). To reinforce these results, OLCI-derived spectra from L2 standard processing at three different points in the Tagus estuary have been compared, with one pixel chosen at the inner bay, one at the mid region and one outside the estuary, respectively. Spectra corresponding to each pixel is presented in Figure 6.4.

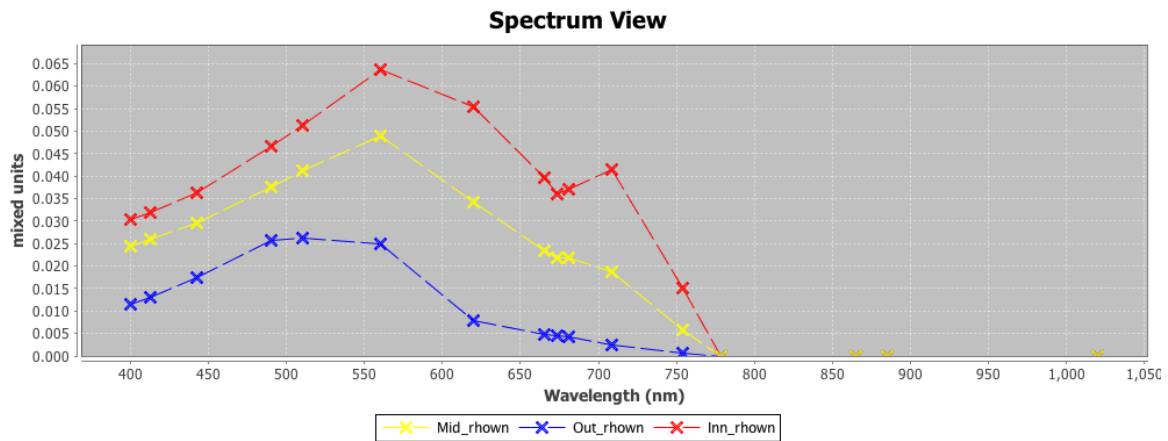


Figure 6.4 - OLCI-derived spectra corresponding to three different locations in the estuary. Inn (red dashed line) correspond to a pixel located in the inner basin, mid (yellow dashed line) is located in the middle region and out (blue dashed line) is located just outside the mouth of the estuary. Spectra derived from L2 S3A-OLCI image acquired on 31/08/2018, same day of in situ sampling.

In the spectra presented in Figure 6.4, the above-mentioned bump at ~ 670 nm is clearly visible in the spectrum corresponding to the inner region (red dashed line) and it gradually disappears when moving towards to the mouth of the estuary (yellow and blue dashed lines).

More information about the hydrodynamics (Neves, 2010; Dias and Valentim, 2011), water mixing processes (Neves, 2010) and phytoplankton (Gameiro *et al.*, 2004; Gameiro, Cartaxana and Brotas, 2007) in the Tagus estuary might help to draw more solid conclusions.

6.2 Remote sensing algorithms evaluation

6.2.1 Atmospheric correction comparison

Since about 90% of the signal measured by the satellite-sensors comes from the atmosphere, the application of a good atmospheric correction is crucial before applying algorithms for water-quality parameters retrieval. The challenges in performing atmospheric corrections over coastal and inland waters is well known (Giardino *et al.*, 2019) and it is mainly due to their optical complexity and the proximity of to land.

Here five different processors were compared (considering both S2-MSI and S3-OLCI data) that use significantly different methodologies and the preliminary results of the present work shows that two out of the five AC schemes tested performed better, namely C2RCC and Polymer, for both sensors. However, such results cannot be considered statistically significant due to the small amount of match-ups available for each processor. For the S2-MSI, C2RCC, Sen2Cor and Polymer had 3 match-ups, while processing with Acolite only 2 match-ups were available. All the processors that produced 3 match-ups showed at least two wavebands with correlation > 0.9 , although no specific waveband performed well with all processors. It should be remarked here, that even if the R^2 returned significantly high values, these results should be carefully interpreted and no generalizations considered due to the small amount of data used. Regarding the S3-OLCI data, only C2RCC had enough match-ups (8 total match-ups) for statistical analysis, not allowing comparison between the different processors. Only 2 match-ups were available for BPAC and Polymer.

Even if the AC comparison performed in the present work is not statistically significant, similar results have been found in previous studies considering a significant larger dataset. Warren *et al.* (2019), tested six different AC processors on S2-MSI imagery in two optically diverse coastal regions and 13 inland

water bodies with a total number of match-ups ranging between 1059 to 1668. Results showed that C2RCC and Polymer achieved the lowest errors across the different datasets. Pereira-Sandoval et al. (2019), also tested 5 different AC algorithms applied to S2-MSI over several types of inland waters resulting C2RCC and Polymer as the best performing processors with high coefficient of determination and low errors associated. Regarding the S3-OLCI, again Polymer and C2RCC seems to be the best performing processors for a better removal of the atmospheric signal. Mograne et al. (2019), tested five AC processors applied to S3-OLCI imagery over coastal waters with results showing the good performances of Polymer and C2RXX (the alternative net of C2RCC trained for high backscatter waters).

Compared with S2 data, S3 showed significantly lower R^2 values at all wavelengths being the highest R^2 equal to 0.26 at 665 nm wavelength. This might be explained by the coarse spatial resolution of the OLCI sensor compared to the sampling stations. In fact, a spatial resolution of 300 m might lead to high uncertainties when sampling in estuaries close to the shore (as was the case of the present study) due to typical high spatial and temporal variability in these areas. A single pixel must be chosen for the *in situ* comparison due to the OLCI spatial resolution and if the sampling station is close to the shore, that pixel might also be contaminated by the land. On the other hand, choosing an adjacent pixel risks the comparison with a different state of the system due to the already mentioned dynamics of the estuary, where 300 m difference might result in significant *in situ* discrepancies.

6.2.2 Water-quality algorithms test

Even with a reduced dataset, 2 out of the 5 AC processors resulted to better perform the removal of the atmospheric signal for a better retrieval of the optically active parameters in the water, C2RCC and Polymer. It is interesting that these two processors performed very similarly in both transitional and inland waters, presenting similar correlations and errors even when using default settings as is the case of the present work. Similar results have also been discussed by Warren et al., 2019, where different atmospheric processors have been tested on S2 data in a much larger dataset of *in situ* radiometric measurements over coastal and inland waters.

This is particularly true when retrieving information using data from S2-MSI instrument. However, with S3-OLCI data, none of the processors showed to outperform in all the study areas, presenting contrasting patterns for the two estuaries. On the Tagus estuary, the Sentinel-3 retrieved data gave significantly better correlations (for both SPM and turbidity products) respect to the Sentinel-2 data, showing the good capabilities of the S3-ocean colour sensor for the retrieval of such products in transitional waters. However, the Sado estuary case study showed that there are some limitations on the use of such sensor in smaller estuaries. In fact, the SPM and turbidity products derived from S3-OLCI instrument in the Sado estuary showed poorer correlations with respect to the Tagus estuary. This result might be due to the smaller size of the Sado estuary compared to the Tagus. In fact, in the Tagus estuary it has been noticed that removing data corresponding to the sampling points closest to the shore from the match-ups dataset, the correlations improved drastically. This was not possible to do with the Sado estuary dataset because of the geographical distribution of the sampling stations. Most of the stations are located less than 300 m from the shore and couldn't be removed from the database due to the small number of sampling stations distributed along the estuary. On the other hand, choosing an adjacent pixel would have led to the comparison of a different state of the water.

However, it can be concluded that even if the correlations are worse in the Sado estuary, results concord about the best performing processors. For both estuaries the combination of Polymer atmospheric correction with Nechad et al. (2010) algorithm at 705 nm applied to S2-MSI data resulted to be the best

processing choice for both SPM and turbidity retrieval. The good performances of the 705 nm (MSI) and 709 nm (OLCI) wavelengths for SPM and turbidity retrieval in the Tagus estuary are reinforced by the statistical results of the application of the algorithms under test to *in situ* ρ_w . In fact, results from this analysis showed the best relationships with *in situ* values at 705 nm and 709 nm. The overall results showed that such algorithms performed very well when compared to *in situ* SPM at all wavelengths suggesting the good suitability of such algorithms for the Tagus estuary.

An example of turbidity maps obtained using Polymer AC and Nechad algorithm at 705 nm and 709 nm for a S2-MSI and S3-OLCI images are shown in Figure 6.5.

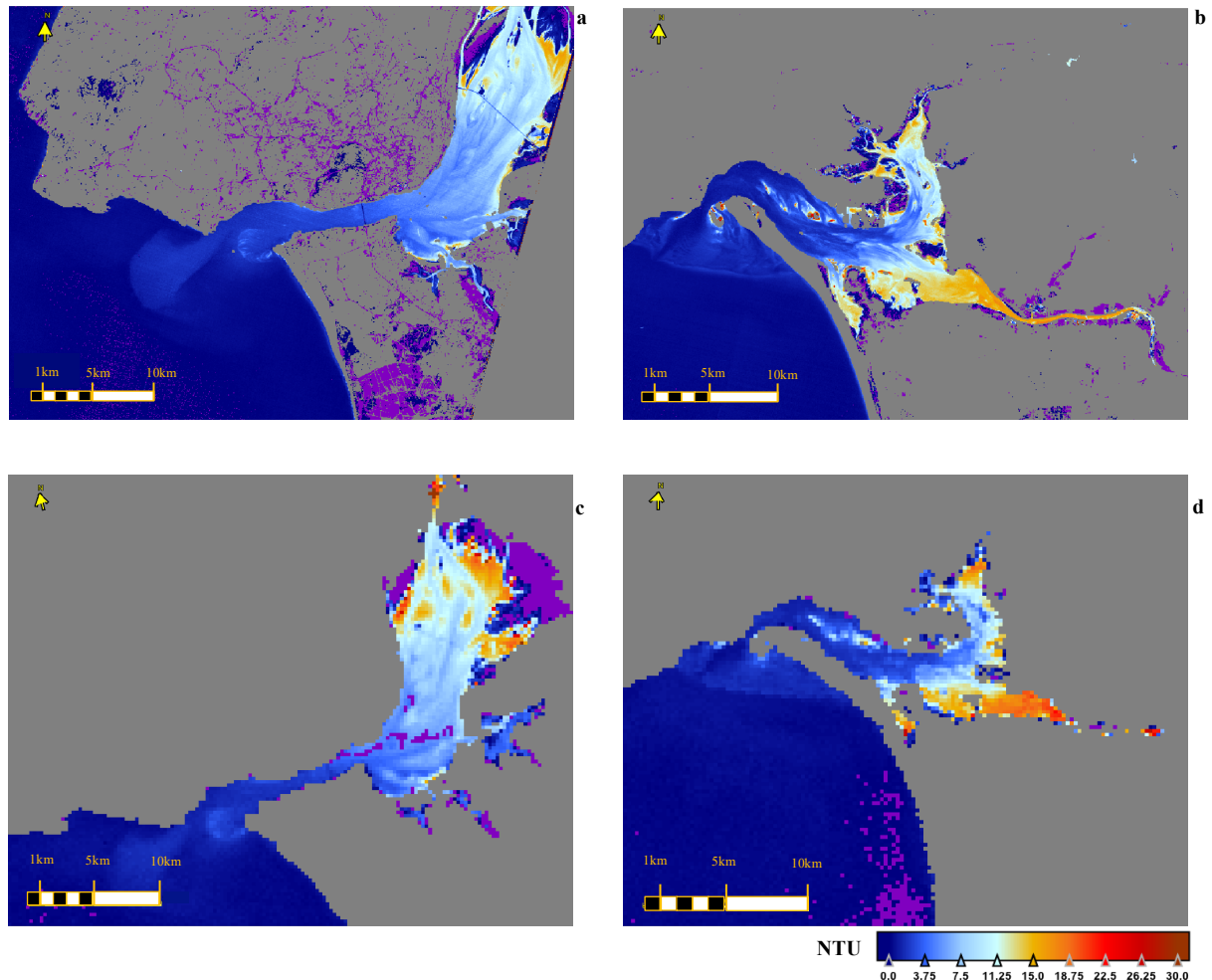


Figure 6.5 – Examples of turbidity maps processed using Polymer AC and Nechad et. al. (2009) turbidity algorithm. (a) and (b) represent images processed from S2-MSI imagery (60m spatial resolution). (c) and (d) shows S3-OLCI processed images (300 m spatial resolution). On the left side (a and c) the Tagus estuary (both images sensed on the 31/08/2018 from S2A and S3A respectively). On the right side (b and d) the Sado estuary (both images sensed on the 15/05/2018 from S2B and S3A respectively). Purple color on images represent negative (invalid) values.

Regarding the inland waters, the available data from the present work showed that statistics are not significant to determine which processor is more suitable for the SPM retrieval in such environments. The lack of match-ups for the comparison with *in situ* data did not permit to explore in depth the capability of this satellite (S2-MSI) to monitor reservoirs. However, despite the small amount of available data, results indicated that there is a relationship that responds to changes in SPM concentrations, which may be promising. If considering all the water bodies as a whole, C2RCC processor performed poorly suggesting that the Neural Network method still needs training in such water

types. Unlike the estuaries, the highest correlations have been found at higher wavelengths (*i.e.* 783 nm) from all the AC processors. In this type of waters, Polymer processor is the one giving the better estimates for the SPM retrieval showing similar correlations and errors to the transitional waters.

Because of this and thanks to the temporal resolution of the S2-MSI of 5 days, the S2-MSI could be a powerful tool for monitoring short-time variability of water quality parameters within a reservoir (example in Figure 6.6).

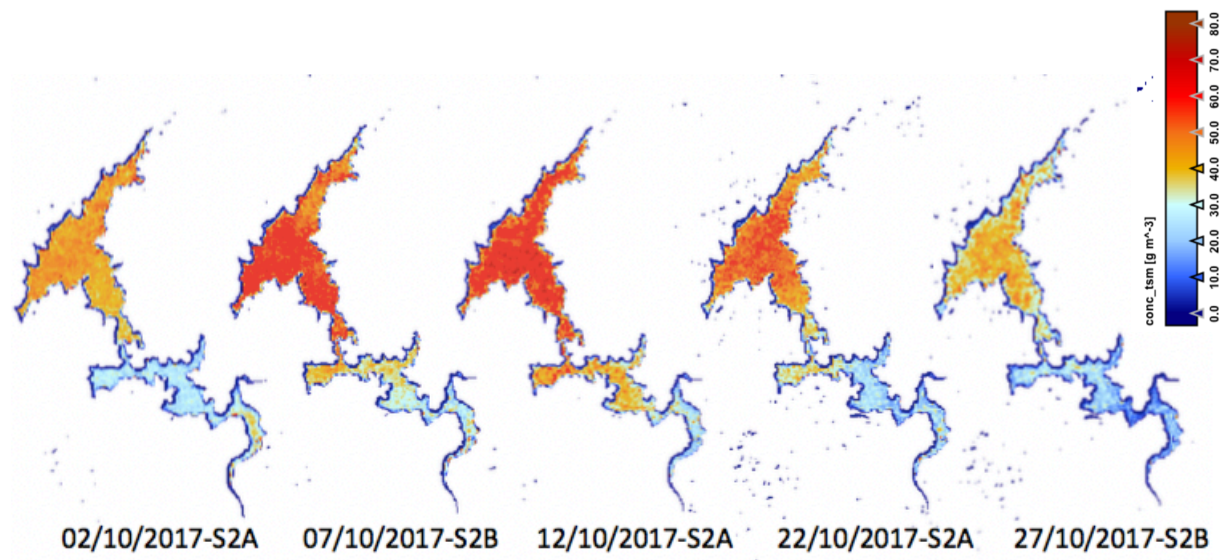


Figure 6.6 - Example of C2RCC processed SPM data: Sequence obtained for Póvoa e Meadas reservoir (P1).

More data is needed to understand the algorithms performance and the impact of sediment type and organic matter content in its accuracy. The results of the *in situ* SPM analysis, however, showed a high variability between the different reservoirs that could make them good test sites for the future work on evaluating the applicability of SPM and turbidity algorithms.

When using data from S3-OLCI, results are discordant for the two estuaries. For the Tagus estuary, the standard L2 SPM product resulted to produce the highest correlation with *in situ* SPM measurements. However, also C2RCC processor with Nechad et al. (2010) algorithm at 665 nm showed very satisfactory correlation ($R^2=0.8$) with significantly smaller errors associated. On the Sado estuary, neither the standard L2 SPM product nor any band of the C2RCC processors performed well. The best processing choice have been found with Polymer AC and Nechad et al. (2010) at 779 nm. A bigger dataset is however crucial for a more significant validation exercise.

At both transitional and inland waters, Sen2Cor and Acolite resulted to be the least performing processor for the SPM and turbidity retrieval in all the study areas.

C2RCC and Polymer are the best choice, mainly when retrieving information with the S2-MSI sensor and applying a semi-analytical algorithm (*i.e.* Nechad et al 2009, 2010, or Dogliotti et al., 2015). The SPM standard product estimated by the C2RCC Neural Network from S2-MSI data, did not present satisfactory results in any of the study areas. However, the tested semi-analytical algorithms performed well in retrieving both SPM and turbidity from the C2RCC reflectance. This suggests that the atmospheric correction part of the processor performs relatively well compared to the water-parameters retrieval part of the Neural Network that might still needs training to include the regional optical

characteristics of the studied areas. However, when using data from S3-OLCI, besides the application of a semi-analytical algorithm to C2RCC and Polymer reflectance, which produced satisfactory correlations with the *in situ* data, also the SPM standard product from the L2 OLCI imagery also gave good results. This can be explained by the nature of the two sensors, being the OLCI specifically designed for water quality monitoring with many narrow bands and higher Signal-To-Noise (SNR) ratios due to the lower spatial resolution (Arabi *et al.*, 2020). In fact, a multispectral sensor such as OLCI present higher SNR because of the smaller number of photons captured by each detector due to the narrower width of the spectral channels (Moses *et al.*, 2012). The photon noise has a significant impact on the retrieved reflectance, and therefore, the estimated biophysical parameters. This is especially the case for data acquired over water bodies which are highly absorptive. In the case of sensors designed for land monitoring (as S2-MSI) the SNR is lower since the magnitude of the signal from the land is larger. In IOCCG, (2000) a higher sensitivity and SNR is suggested for sensors used for water applications. In turn, Moses *et al.*, (2012) demonstrated that different magnitudes and spectral shapes of SNR affect the performance of spectral algorithms. Depending on the spectral regions in which the algorithms operate.

Comparing the SPM and turbidity retrieved products, in all the study areas the turbidity retrieval gave general better correlations with respect to the SPM retrieval. This have been found for both sensors although was much clearer with Sentinel-2 data and confirmed when retrieving both turbidity and SPM using *in situ* reflectance values. This might be caused by different factors. First, the turbidity parameter is less subject to measurement errors than *in situ* SPM. Röttgers *et al.* (Röttgers, Heymann and Krasemann, 2014) demonstrated that very large uncertainties can be associated with most of the SPM samples. Their results showed that these errors were mainly associated to salt retention and loss of filter material during washing and drying procedures. This error varied with salinity and would be significant at lower concentrations of SPM (Röttgers, Heymann and Krasemann, 2014). Also, turbidity is an optical parameter highly related to backscattering (Dogliotti *et al.*, 2015) and thus to reflectance. It should be remarked here, that the Dogliotti *et al.* (2015) algorithm requires the 645 nm waveband for low *in situ* turbidity ranges. However, neither the MSI or the OLCI sensors have the 645 nm band and the 665 nm has been used instead. Errors might be associated to the selection of such waveband due to the influence of the Chl-*a* signal at this wavelength.

Given the non-linearity of SPM optics properties in estuarine environment (Mobley, 1994) and the presence and interaction of different optically active constituents such as CDOM and phytoplankton pigments, an algorithm calibrated regionally based on the optical characteristics of the type of waters under investigation is therefore needed to accurately quantify SPM from satellite data.

To explain the poorer retrieval of SPM through a global algorithm respect to turbidity, the differences between the SPM and turbidity retrieval algorithms should be noted as suggested by Dogliotti *et al.* (2015). In fact, since turbidity (a measure of side-scattering) is an IOP, it is not necessary to consider the potential variability of mass specific optical properties. On the other hand, SPM retrieval algorithms will be also sensitive to particle size, density and refractive index which can be important sources of regional variability for retrieval of SPM concentration.

In the present study, the turbidity product has been demonstrated to be easier and better to be retrieved from satellite imagery with smaller uncertainties associated. This was clearer when retrieving SPM and turbidity from S2-MSI sensor respect to the S3-OLCI. This might be related to the fact that the OLCI sensor is a specific Ocean Colour instrument (as already mentioned before) while the S2-MSI has been developed for land applications.

This has also been demonstrated by the turbidity results derived from S2 and S3 in the Tagus estuary where the S3-OLCI standard algorithm also showed interesting capabilities. However, such results are not applicable for both estuaries, where no significant correlation has been found from this sensor in the Sado estuary due to the coarse spatial resolution of the OLCI sensor compared to the geographical distribution of the sampling stations in the Sado estuary as already discussed before in this chapter.

The results presented here showed that there is a strong need of more *in situ* information and to develop a regionally calibrated algorithm for SPM retrieval, since none of the approaches tested returned satisfactory correlation with the *in situ* data. Regarding the turbidity retrieval, different approaches tested on the present study showed that, even using default parameters for the processing, the correlation with the *in situ* data can be considered good enough to use the satellite-derived turbidity for water quality studies.

6.2.3 Number of match-ups: limitations

When performing satellite validation/test exercises the number of total match-ups is crucial for statistically significant results. In the present work, three main factors have contributed for the reduction of the total number of match-ups: coincident time of *in situ* sampling with satellite passage, clear sky conditions and sun-glint effect.

Regarding the coincident sampling time with satellite passage, for the present work, different *in situ* measurements could not be used because sampling occurred at more than 2h difference from the satellite passage due to the specific objectives of the various project (*i.e.* collecting water samples at a particular tide condition which is not necessarily the same time of the satellite passage).

The campaigns performed within the PLATAGUS project in the Tagus estuary, whose main objective was the validation of satellite products, allowed to choose only measurements performed within ± 30 minutes time window between *in situ* sampling and satellite passage. A type of estuary like the Tagus or Sado are highly dynamic systems where one-hour difference may result in changes in the type of water being sampled as shown by the *in situ* measurements. Longer time windows may produce more match-ups but risks the comparison of different state of the system due to its dynamic nature. However, sampling at different stations within 30 minutes of time constraint is not always feasible. Because of this, for water-quality algorithms test only match-ups with $\pm 2h$ difference have been used, otherwise very few data would be available for the algorithms test. This is not true when sampling in more static environments like inland waters, where the processes occurring in the water take longer time with respect to estuaries. Because of this, a time window of $\pm 24h$ has been used for the inland waters.

In the present work the small amount of total number of match-ups was also caused by the sun-glint effect that occurs especially in the Tagus estuary region during summer months (Figure 6.7). Some of the AC processors, like Polymer, have been specifically designed to take into account the presence of sun-glint and correct it. However, when the sun-glint is significantly strong, as may occur in the Tagus estuary (Figure 6.8), even these types of processors are not able to correct this phenomenon and no reflectance output can be obtained. This type of processors should be the best option in areas where the sun-glint effect is important. It is interesting to note that the sun-glint phenomenon has only been detected from S2 images and it results to be stronger when the tile is composed with a bigger fraction of water pixels with respect to land pixels. Further investigation is needed, however, in order to understand the main drivers of the sun-glint effect and its intensity.

A bar chart showing the percentage of sun-glint events on S2 images over the past 3 years is presented in Figure 6.7.

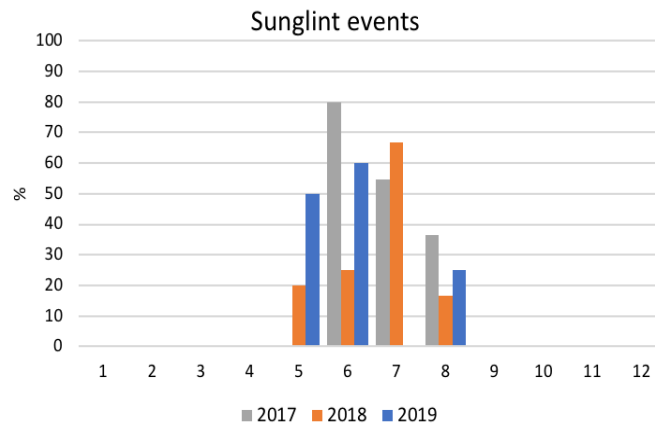


Figure 6.7 - Percentage of sun-glint contaminated images over the Tagus estuary. Both Sentinel-2A and Sentinel-2B have been considered.

It is noticeable in Figure 6.7 that the sun-glint events only occurred between May and August on the past three years. This suggests that sampling in the Tagus estuary with the scope of satellite products validation might improve the match-ups probability if sampling at different time of the year. Sun-glint occurrences have also been noticed in all the 5 reservoirs under investigation in the same period of the year with, however, a significantly smaller intensity. In the Sado estuary no sun-glint events have been observed. However, the analysis of the sun-glint phenomena and its intensity is only a preliminary study on the study areas under investigation. Further and in-deeper depth analysis needs to be performed including the analysis and comparison of the geometry of observation for the different tiles that cover the study areas.



Figure 6.8 - Example of RGB S2-B image contaminated by a strong sun-glint. On the right, the Tagus estuary is completely covered by the reflection of sun which masks the water features. RGB image captured by S2-B satellite on the 28-05-2019.

Chapter 7: Conclusions

This chapter presents an overview of the main conclusions of the present study and closes with few suggestions for future research in estuaries and inland waters through remote sensing techniques.

The work presented here was carried out with the main objectives of testing different atmospheric correction approaches and SPM and turbidity algorithms in optically complex waters, namely estuaries and water reservoirs, for a better understanding of the potentiality of remote sensing techniques to study such highly dynamic and optically complex waters in the Portuguese territory. Firstly, an *in situ* characterization of the study areas has been performed in terms of spatial and temporal distribution of SPM and turbidity, as well as the relationship between these two parameters. Sequentially, the *in situ* data have been used for testing the performance of different AC processors and SPM and turbidity retrieval algorithms using S3-OLCI and S2-MSI imagery.

With these objectives in mind, a set of observations collected between 2017 and 2019, in the frame of several research projects, was gathered, analysed and compared to satellite data.

The Tagus estuary resulted to be the region with the largest data set, constituted by SPM, turbidity, suspended organic matter data and radiometric measurements. This allowed to perform a statistical study on the area, however still preliminary. Regarding the Sado estuary and inland waters, no *in situ* radiometric data were available for a direct test of the ACs algorithms which is crucial for a relevant validation exercise. Moreover, the available data set for the inland waters didn't permit to make any statistically significant conclusion due to the very low number of total match-ups and turbidity data.

The analyses conducted for inland waters shall be considered as a first and preliminary effort to understand the potentiality of satellite imagery for monitoring water quality parameters in Portuguese reservoirs. Besides the poor correlations found between *in situ* and satellite-derive SPM, the preliminary results indicated that there is a relationship that responds to changes in SPM concentrations. More data is needed in order to understand algorithms performance and the impact of sediment type and organic matter presence (both dissolved and particulate) in its accuracy. Moreover, the different performance obtained for the various reservoirs and processors reinforces that validation and optimization of products are needed before any routine use of this satellite data for monitoring.

Even so, the *in situ* data analysed on the present work showed the good potentiality of the selected inland waters for future remote sensing validation exercises due to large ranges of SPM, turbidity and organic matter content within the different water bodies.

The results presented in this work indicate that the performance of S2-MSI and S3-OLCI sensors for the retrieval of turbidity in optically complex waters is acceptable even using default settings for the data processing and a global semi-analytical algorithm such as Nechad (2009) and Dogliotti (2015) which do not need to be calibrated regionally. Regarding the SPM retrieval, the results from the present work suggested that there is still a strong need of validation/calibration exercises for the selected study areas mainly from S2-MSI data. S3-OLCI showed better correlations for the SPM retrieval with, however some discrepancies between the two estuaries.

It can be concluded that turbidity data are easier to retrieve with higher accuracy and smaller errors than SPM. The best processing option for transitional waters resulted to be Polymer Atmospheric Correction with Nechad (2009 for SPM, 2010 for turbidity) algorithms at 705 nm when using S2-MSI derived data. Regarding the S3-OLCI data significant discrepancies have been found between the two estuaries.

Future work will focus on the understanding the reasons of such dissimilarities. However, it can be concluded that for the Tagus estuary the L2 standard SPM product gave satisfactory results with high correlations and small errors. The best choice for turbidity retrieval resulted to be Polymer with Nechad (2010) at 620 nm for the Tagus estuary and at 779 nm for the Sado estuary. Should be remarked here that correlations and errors found for the Sado estuary with this sensor cannot be considered satisfactory.

All the satellite data used for this work have been processed with default parameters as is the best option for a general user when the optical properties of the water body or the atmospheric conditions are unknown. Regarding the SPM retrieval from S2-MSI and S3-OLCI data, the associated correlations and errors indicate that there is still a strong need of algorithms development perhaps with a regional calibration specific for the optical characteristics of the study areas or finding a local relationship between SPM and turbidity as was previously suggested by Dogliotti et al (2015).

Remote sensing techniques for water monitoring in Portuguese territory is already in use but it mostly concerns coastal applications (Cristina *et al.*, 2009; Goela *et al.*, 2013; Brito *et al.*, 2015; Sá *et al.*, 2015) and the Alqueva reservoir as inland waters (Potes *et al.*, 2011, 2018; Potes, Costa and Salgado, 2011; Rodrigues *et al.*, 2020). From the literature review performed in the present work, has emerged the lack of ocean colour remote sensing products validation works in Portuguese waters, especially in transitional and inland water bodies, and particularly on SPM and turbidity. Given the well-known importance of such ecosystems and the crucial role of products validation for reliable monitoring activities through remote sensing techniques we consider that bigger efforts should be put on validation and calibration exercises for these types of ecosystem on Portuguese territory in the future. The advantages of a reliable tool to monitor water quality or a specific parameter with high accuracy and small effort (remote sensing monitoring activities are inexpensive and requires very small labour work compared to *in situ* monitoring and can provide information on large geographical regions) might interest different kind of users, not only the research field. Both institutional and private users might take advantages of a valid instrument to monitor turbidity, for example, as is listed as a mandatory parameter to be measured by EU member state in Marine Strategy Framework Directive (European Union, 2008). Institutional users might include environment agencies, water management authorities and port authorities. Private users can include agriculture, forestry, aquaculture and drinking water companies. Fishery and recreation industries are also interested, from the water quality and, clarity as well as benthic habitat point of view.

From my personal point of view, the potential of remote sensing techniques is enormous for many different fields. From oceanography studies to agriculture, forestry, weather monitoring, surface changes, aquaculture, oil spills, microplastic detection, climate change and much more. The use of sensors on board of satellites as a monitoring tool has started relatively recently. The first satellite ever, the Sputnik (Soviet Union) have only been launched in 1957 (Tatem, Goetz and Hay, 2008). Since then, hundreds of Earth-observing satellites have followed, including the recent Sentinel-2 and Sentinel-3 from the Copernicus program (ESA) studied in the present work. Considering the incrementing rate of technology development, I personally consider that more efforts should be put on the understanding of the remote sensing capabilities and applications. Every year, new satellite-retrievable products are presented, offering new tools to different type of users. It is sufficient to think about the advantages that remote sensing techniques brought to marine studies. Before the use of satellite imagery, monitoring could only be performed through *in situ* sampling, which can be expensive, time consuming, laborious and the samples may not be representative of the total area under interest. With the advent of Ocean Colour Remote Sensing, highly detailed maps of specific water parameters (*i.e.* Chl-*a*) for a large geographical area can be produced with very small effort. However, the comparison with the *in situ* data

remains crucial for understanding the reliability and the uncertainties associated of such satellite-derived data.

All these reasons drove the motivations of the above-presented work and made me realise about the needs that still exist in this research field particularly in the Portuguese territory and that carrying on this preliminary research could make a great contribution for transitional and inland water monitoring in Portugal.

References

- (ISO), I. O. S. (1999) *Water quality - Determination of turbidity*.
- Almeida, P. *et al.* (2017) *Gestão e Promoção da Pesca Recreativa em Albufeiras na Região Mediterrânica - Relatório intercalar*.
- Alt-Epping, U. *et al.* (2007) 'Provenance of organic matter and nutrient conditions on a river- and upwelling influenced shelf: A case study from the Portuguese Margin', *Marine Geology*, 243(1–4), pp. 169–179. doi: 10.1016/j.margeo.2007.04.016.
- Althuis, I. J. A. and Shimwell, S. (1995) 'Modelling of remote sensing reflectance spectra for suspended matter concentration detection in coastal waters.', *EARSEL Advances in Remote Sensing*, 4, pp. 53–59.
- Antoine, D. and Morel, A. (1999) 'A multiple scattering algorithm for atmospheric correction of remotely sensed ocean color (MERIS instrument): Principle and implementation for atmospheres carrying various aerosols including absorbing ones.', *Int. J. Remote Sensing*, 20, pp. 1875–1916.
- APA (2016) 'Parte 6_Anexos - Região hidrográfica do tejo e ribeiras do oeste (rh5)'. doi: 10.1179/1743132814Y.0000000460.
- Arabi, B. *et al.* (2020) 'Integration of in-situ and multi-sensor satellite observations for long-term water quality monitoring in coastal areas', *Remote Sensing of Environment*. Elsevier, 239(April 2019), p. 111632. doi: 10.1016/j.rse.2020.111632.
- Babin, M. *et al.* (2003) 'Light scattering properties of marine particles in coastal and open ocean waters as related to the particle mass concentration', *Limnology and Oceanography*. doi: 10.4319/lo.2003.48.2.0843.
- Beltrán-Abaunza, J. M. (2015) *Remote Sensing in optically complex waters*.
- Berthon, J. F. *et al.* (2007) 'Measurements and modeling of the volume scattering function in the coastal northern Adriatic Sea', *Applied Optics*. doi: 10.1364/AO.46.005189.
- Bettencourt, A. *et al.* (2003) 'Typology and Reference Conditions for Portuguese Transitional and Coastal Waters. Development of guidelines for the application of the European Union Water Framework Directive.', *INAG, IMAR*.
- Binding, C. E., Bowers, D. G. and Mitchelson-Jacob, E. G. (2003) 'An algorithm for the retrieval of suspended sediment concentrations in the Irish Sea from SeaWiFS ocean colour satellite imagery', *International Journal of Remote Sensing*, 24(19), pp. 3791–3806. doi: 10.1080/0143116021000024131.
- Bowers, D. G. and Binding, C. E. (2006) 'The optical properties of mineral suspended particles: A review and synthesis', *Estuarine, Coastal and Shelf Science*. doi: 10.1016/j.ecss.2005.11.010.
- Brito, A. C. *et al.* (2015) 'Effect of phytoplankton size classes on bio-optical properties of phytoplankton in the Western Iberian coast: Application of models', *Remote Sensing of Environment*. doi: 10.1016/j.rse.2014.10.020.
- Brockmann, C. *et al.* (2016) 'Evolution of the C2RCC neural network for Sentinel 2 and 3 for the retrieval of ocean colour products in normal and extreme optically complex waters', *European Space Agency, (Special Publication) ESA SP, SP-740(May)*, pp. 9–13.

- Bukata, R. P. *et al.* (2018) *Optical properties and remote sensing of inland and coastal waters, Optical Properties and Remote Sensing of Inland and Coastal Waters*. doi: 10.1201/9780203744956.
- Caeiro, S. S. F. D. S. (2004) *Environmental Data Management in the Sado Estuary : Weight of Evidence To Assess Sediment Quality*.
- Campbell, J. B. and Wynne., R. H. (2011) *Introduction to Remote Sensing FIFTH EDITION, Cartography*. doi: 10.1007/s13398-014-0173-7.2.
- Cristina, S. V. *et al.* (2009) ‘Assessment of water-leaving reflectances of oceanic and coastal waters using MERIS satellite products off the southwest coast of Portugal’, *Journal of Coastal Research*.
- Dias, J. M. and Valentim, J. M. (2011) ‘Numerical modeling of Tagus estuary tidal dynamics’, *Journal of Coastal Research*.
- Doerffer, R. and Schiller, H. (2007) ‘The MERIS case 2 water algorithm’, *International Journal of Remote Sensing*. doi: 10.1080/01431160600821127.
- Dogliotti, A. I. *et al.* (2015) ‘A single algorithm to retrieve turbidity from remotely-sensed data in all coastal and estuarine waters’, *Remote Sensing of Environment*. Elsevier B.V., 156, pp. 157–168. doi: 10.1016/j.rse.2014.09.020.
- Eleveld, M. A. *et al.* (2008) ‘Remotely sensed seasonality in the spatial distribution of sea-surface suspended particulate matter in the southern North Sea’, *Estuarine, Coastal and Shelf Science*, 80(1), pp. 103–113. doi: 10.1016/j.ecss.2008.07.015.
- ESA (2015) ‘SENTINEL-2 User Handbook’, (1), p. 64. doi: GMES-S1OP-EOPG-TN-13-0001.
- ESA (no date) *Sentinel-3 OLCI User Handbook*.
- European Commission (2003) *Common Implementation Strategy for the Water Framework Directive (2000/60/EC). Guidance Document No. 5. Transitional and Coastal Waters - typology, reference conditions and classification systems.*, *Official Journal of the European Union*. Available at: <http://www.waterframeworkdirective.wdd.moa.gov.cy/guidance.html>.
- European Union (2008) ‘Directive 2008/56/EC of the European Parliament and of the Council of 17 June 2008 establishing a framework for community action in the field of marine environmental policy (Marine Strategy Framework Directive).’, *Official Journal of the European Union*, 164, pp. 19–40.
- Ferreira, J. G. *et al.* (2005) ‘MONAE - Water Framework Directive – Transitional and Coastal Waters Proposal for the definition of water bodies’, p. 38.
- Fettweis, M. P. and Nechad, B. (2011) ‘Evaluation of in situ and remote sensing sampling methods for SPM concentrations, Belgian continental shelf (southern North Sea)’, *Ocean Dynamics*, 61(2), pp. 157–171. doi: 10.1007/s10236-010-0310-6.
- Gameiro, C. *et al.* (2004) ‘Variability in chlorophyll and phytoplankton composition in an estuarine system’, *Hydrobiologia*. doi: 10.1023/B:HYDR.0000038858.29164.31.
- Gameiro, C., Cartaxana, P. and Brotas, V. (2007) ‘Environmental drivers of phytoplankton distribution and composition in Tagus Estuary, Portugal’, *Estuarine, Coastal and Shelf Science*, 75(1–2), pp. 21–34. doi: 10.1016/j.ecss.2007.05.014.
- Giardino, C. *et al.* (2019) ‘Imaging Spectrometry of Inland and Coastal Waters: State of the Art, Achievements and Perspectives’, *Surveys in Geophysics*. Springer Netherlands, 40(3), pp. 401–429. doi: 10.1007/s10712-018-9476-0.

- Goela, P. C. *et al.* (2013) ‘Specific absorption coefficient of phytoplankton off the Southwest coast of the Iberian Peninsula: A contribution to algorithm development for ocean colour remote sensing’, *Continental Shelf Research*. doi: 10.1016/j.csr.2012.11.009.
- Gohin, F. *et al.* (2005) ‘Satellite-derived parameters for biological modelling in coastal waters: Illustration over the eastern continental shelf of the Bay of Biscay’, *Remote Sensing of Environment*, 95(1), pp. 29–46. doi: 10.1016/j.rse.2004.11.007.
- Gordon, H. R., Brown, O. B. and Jacobs, M. M. (1975) ‘Computed Relationships Between the Inherent and Apparent Optical Properties of a Flat Homogeneous Ocean’, *Applied Optics*. doi: 10.1161/hc4501.098944.
- Han, B. *et al.* (2016) ‘Development of a semi-analytical algorithm for the retrieval of suspended particulate matter from remote sensing over clear to very turbid waters’, *Remote Sensing*, 8(3). doi: 10.3390/rs8030211.
- Hu, C., Carder, K. L. and Muller-Karger, F. E. (2000) ‘Atmospheric correction of SeaWiFS imagery over turbid coastal waters: A practical method’, *Remote Sensing of Environment*. doi: 10.1016/S0034-4257(00)00080-8.
- HYGEOS (no date) *Polymer*.
- IOCCG (2000) *Reports of the International Ocean-Colour Coordinating Group. Remote Sensing of Ocean Colour in Coastal, and Other Optically-Complex, Waters*. Available at: <http://www.vliz.be/imis/imis.php?module=ref&refid=134621&request=147862>.
- IOCCG (2010) *IOCCG Report Number 10: Atmospheric correction for remotely-sensed ocean-colour products, IOCCG web page*. Available at: <http://www.ioccg.org/reports/report10.pdf>.
- IOCCG (2018) *Reports and Monographs of the International Ocean Colour Coordinating Group Earth Observations in Support of Global Water Quality Monitoring*.
- Jafar-Sidik, M. *et al.* (2017) ‘The relationship between Suspended Particulate Matter and Turbidity at a mooring station in a coastal environment: consequences for satellite-derived products’, *Oceanologia*. Institute of Oceanology of the Polish Academy of Sciences, 59(3), pp. 365–378. doi: 10.1016/j.oceano.2017.04.003.
- Jerlov, N. G. (1968) *Optical Oceanography*. New York: Elsevier.
- Jerlov, N. G. (1975) *Marine optics*. New York: Elsevier.
- Kari, E. *et al.* (2017) ‘Retrieval of suspended particulate matter from turbidity–model development, validation, and application to MERIS data over the Baltic Sea’, *International Journal of Remote Sensing*. doi: 10.1080/01431161.2016.1230289.
- Kaufman, Y. J. and Sendra, C. (1988) ‘Algorithm for automatic atmospheric corrections to visible and near-IR satellite imagery’, *International Journal of Remote Sensing*. Taylor & Francis, 9(8), pp. 1357–1381. doi: 10.1080/01431168808954942.
- Knaeps, E. *et al.* (2018) ‘The SeaSWIR dataset’, *Earth System Science Data*, 10(3), pp. 1439–1449. doi: 10.5194/essd-10-1439-2018.
- Kummu, M. *et al.* (2011) ‘How close do we live to water? a global analysis of population distance to freshwater bodies’, *PLoS ONE*. doi: 10.1371/journal.pone.0020578.
- Van Der Linde, D. W. (1998) ‘Protocol for determination of Total Suspended Matter in oceans and

coastal zones.’, *JCR Technical Note*.

Liu, H. *et al.* (2017) ‘Application of Sentinel 2 MSI Images to Retrieve Suspended Particulate Matter Concentrations in Poyang Lake’, *Remote Sensing*, 9(7), p. 761. doi: 10.3390/rs9070761.

Main-Knorn, M. *et al.* (2017) ‘Sen2Cor for Sentinel-2’, (October), p. 3. doi: 10.1117/12.2278218.

Martinez-Vicente, V. *et al.* (2010) ‘Particulate scattering and backscattering related to water constituents and seasonal changes in the Western English Channel’, *Journal of Plankton Research*. doi: 10.1093/plankt/fbq013.

Martins, F. *et al.* (2001) ‘3D modelling in the Sado estuary using a new generic vertical discretization approach’, *Oceanologica Acta*. doi: 10.1016/s0399-1784(01)00092-5.

Martins, M. and Duffiner, M. J. L. (1982) *Estudo Ambiental do Estuário do Tejo, Estudo da qualidade da água: resultados referentes as observações sinópticas em 1980*. Lisboa.

Matthews, M. W. (2011) ‘A current review of empirical procedures of remote sensing in Inland and near-coastal transitional waters’, *International Journal of Remote Sensing*, 32(21), pp. 6855–6899. doi: 10.1080/01431161.2010.512947.

Matthews, M. W. (2017) ‘Bio-optical Modeling of Phytoplankton Chlorophyll-a’, in *Bio-optical Modeling and Remote Sensing of Inland Waters*. doi: 10.1016/B978-0-12-804644-9.00006-9.

Milliman, J. D. and Meade, R. H. (1983) ‘World-wide delivery of sediment to the oceans.’, *Journal of Geology*. doi: 10.1086/628741.

Mobley, C. D. (1994) ‘Mobley CD (1994) Light and water. Academic press, San Diego’, *Academic press*. San Diego.

Mobley, C. D. (1999) ‘Estimation of the remote-sensing reflectance from above-surface measurements’, *Applied Optics*. doi: 10.1364/ao.38.007442.

Mograne, M. *et al.* (2019) ‘Evaluation of Five Atmospheric Correction Algorithms over French Optically-Complex Waters for the Sentinel-3A OLCI Ocean Color Sensor’, *Remote Sensing*, 11(6), p. 668. doi: 10.3390/rs11060668.

Moore, G. F., Aiken, J. and Lavender, S. J. (1999) ‘The atmospheric correction of water colour and the quantitative retrieval of suspended particulate matter in Case II waters: Application to MERIS’, *International Journal of Remote Sensing*. doi: 10.1080/014311699212434.

Morel, A. and Prieur, L. (1977) ‘Analysis of variations in ocean color’, *Limnology and Oceanography*, 22(4), pp. 709–722. doi: 10.1016/j.eururo.2018.01.011.

Moses, W. J. *et al.* (2012) ‘Impact of signal-to-noise ratio in a hyperspectral sensor on the accuracy of biophysical parameter estimation in case II waters’, *Optics Express*. doi: 10.1364/oe.20.004309.

Moses, W. J. *et al.* (2017) ‘Atmospheric Correction for Inland Waters’, in *Bio-optical Modeling and Remote Sensing of Inland Waters*. doi: 10.1016/B978-0-12-804644-9.00003-3.

Myint, S. W. and Walker, N. D. (2002) ‘Quantification of surface suspended sediments along a river dominated coast with NOAA AVHRR and Sea WiFS measurements: Louisiana, USA’, *International Journal of Remote Sensing*, 23(16), pp. 3229–3249. doi: 10.1080/01431160110104700.

Navarro, E. *et al.* (2009) ‘Ecological classification of a set of Mediterranean reservoirs applying the EU Water Framework Directive: A reasonable compromise between science and management’, *Lake and*

Reservoir Management, 25(4), pp. 364–376. doi: 10.1080/07438140903238567.

Nechad, B., Ruddick, K. G. and Park, Y. (2009) ‘Calibration and validation of a generic multisensor algorithm for mapping of turbidity in coastal waters’, *Remote Sensing of the Ocean, Sea ice, and Large Water Regions*, 2009.Vol. 7473, doi: 10.1117/12.830700. The International Society of Optical Engineering, 2009.

Nechad, B., Ruddick, K. G. and Park, Y. (2010) ‘Calibration and validation of a generic multisensor algorithm for mapping of total suspended matter in turbid waters’, *Remote Sensing of Environment*. Elsevier Inc., 114(4), pp. 854–866. doi: 10.1016/j.rse.2009.11.022.

Nekermans, G. *et al.* (2012) ‘In situ variability of mass-specific beam attenuation and backscattering of marine particles with respect to particle size, density, and composition’, *Limnology and Oceanography*. doi: 10.4319/lo.2011.57.1.0124.

Neves, F. J. R. C. dos S. da S. (2010) ‘Dynamics and hydrology of the Tagus Estuary: results from “in situ” observations’, p. 240. Available at: <http://repositorio.ul.pt/handle/10451/2003>.

Nobileau, D. and Antoine, D. (2005) ‘Detection of blue-absorbing aerosols using near infrared and visible (ocean color) remote sensing observations’, *Remote Sensing of Environment*. doi: 10.1016/j.rse.2004.12.020.

Ocean Optics Book (2015). Available at: <http://www.oceanopticsbook.info>.

Ogashawara, I., Mishra, D. R. and Gitelson, A. A. (2017) *Remote Sensing of Inland Waters: Background and Current State-of-the-Art*. Elsevier Inc. doi: <http://dx.doi.org/10.1016/B978-0-12-804644-9.00001-X>.

‘OSPAR Convention for the Protection of the Marine Environment of the North East Atlantic Comprehensive Procedure PORTUGAL Mondego , Tagus and Sado Estuaries’ (2002) *Main*, (December).

Ouaidrari, H. and Vermote, E. F. (1999) ‘Operational Atmospheric Correction of Landsat TM Data based on a simplified formulation of the signal in order’, 15(October 1998), pp. 4–15. doi: 10.1016/S0034-4257(99)00054-1.

Pahlevan, N. *et al.* (2017) ‘Sentinel-2 MultiSpectral Instrument (MSI) data processing for aquatic science applications: Demonstrations and validations’, *Remote Sensing of Environment*. doi: 10.1016/j.rse.2017.08.033.

Pereira-Sandoval, M. *et al.* (2019) ‘Evaluation of Atmospheric Correction Algorithms over Spanish Inland Waters for Sentinel-2 Multi Spectral Imagery Data’, *Remote Sensing*, 11(12), p. 1469. doi: 10.3390/rs11121469.

Potes, M. *et al.* (2011) ‘Remote sensing of water quality parameters over Alqueva reservoir in the south of Portugal’, *International Journal of Remote Sensing*, 32(12), pp. 3373–3388. doi: 10.1080/01431161003747513.

Potes, M. *et al.* (2018) ‘Use of Sentinel 2-MSI for water quality monitoring at Alqueva reservoir, Portugal’, *Proceedings of the International Association of Hydrological Sciences*, 380, pp. 73–79. doi: 10.5194/piahs-380-73-2018.

Potes, M., Costa, M. J. and Salgado, R. (2011) ‘Satellite remote sensing of water turbidity in Alqueva reservoir and implications on lake modelling’, *Hydrology and Earth System Sciences Discussions*, 8(6), pp. 11357–11385. doi: 10.5194/hessd-8-11357-2011.

- Rodrigues, G. *et al.* (2020) ‘Temporal and spatial variations of secchi depth and diffuse attenuation coefficient from sentinel-2 MSI over a large reservoir’, *Remote Sensing*, 12(5), pp. 1–26. doi: 10.3390/rs12050768.
- Rodrigues, M. *et al.* (2017) ‘Characterization of the study areas : Tagus estuary and Ria Formosa’, p. 73.
- Röttgers, R., Heymann, K. and Krasemann, H. (2014) ‘Suspended matter concentrations in coastal waters: Methodological improvements to quantify individual measurement uncertainty’, *Estuarine, Coastal and Shelf Science*. doi: 10.1016/j.ecss.2014.10.010.
- Ruddick, K. *et al.* (2008) ‘Remote Sensing of Suspended Particulate Matter in Turbid Waters : State of the Art and Future Perspectives’, *Ocean Optics XIX conference, 6 - 10 October 2008*, (November 2014), pp. 1–12. Available at: http://www2.mumm.ac.be/downloads/publications/ruddick_oceanoptics_2008.pdf.
- Ruddick, K. G. *et al.* (2006) ‘Data Processing: Scan selection and averaging’, *Limnology and Oceanography*, 51(2), pp. 1167-1179 ST-Data Processing: Scan selection an.
- Sá, C. *et al.* (2015) ‘Remote Sensing of Environment’, *Remote Sensing of Environment*, 168.
- Sathyendranath, S. (1986) ‘Remote sensing of phytoplankton: A review, with special reference to picoplankton.’, *Canadian Bulletin of Fisheries and Aquatic Sciences*, 214, pp. 561–583.
- Silva, C. M., Calvão, T. and Figueiredo, H. (1986) *Estudo Ambiental do Estuário do Tejo, Controlo da qualidade da água, Resultados referentes as observações realizadas em 1982 e 1983*. Lisboa.
- Snyder, W. A. *et al.* (2008) ‘Optical scattering and backscattering by organic and inorganic particulates in U.S. coastal waters’, *Applied Optics*. doi: 10.1364/AO.47.000666.
- Steinmetz, F., Deschamps, P. and Ramon, D. (2009) ‘Atmospheric correction in presence of sun glint : application to MERIS Franc’, *Remote Sensing of Environment*, 220(2003), pp. 571–587.
- Tatem, A. J., Goetz, S. J. and Hay, S. I. (2008) ‘Fifty years of earth-observation satellites’, *American Scientist*. doi: 10.1511/2008.74.390.
- Toming, K. *et al.* (2016) ‘First Experiences in Mapping Lake Water Quality Parameters with Sentinel-2 MSI imagery’.
- UNEP (2002) ‘Global Environment Outlook 3 (GEO-3).’, United Nat.
- UNEP (2007) *United Nations Environment Programme Annual Report*. Nairobi, Kenya.
- Valença, M. *et al.* (2011) *Vigilância da Qualidade do Meio Marinho - 25 anos de estudo*.
- Vanhellemont, Q. (2019) ‘Adaptation of the dark spectrum fitting atmospheric correction for aquatic applications of the Landsat and Sentinel-2 archives’, *Remote Sensing of Environment*. doi: 10.1016/j.rse.2019.03.010.
- Vargas, C. I. C. *et al.* (2008) ‘Análise da vulnerabilidade de uma praia estuarina à inundação: aplicação à restinga do Alfeite (estuário do Tejo)’, *Revista de Gestão Costeira Integrada*, 8, p. 25:43. doi: 10.5894/rgci26.
- Warren, M. A. *et al.* (2019) ‘Assessment of atmospheric correction algorithms for the Sentinel-2A MultiSpectral Imager over coastal and inland waters’, *Remote Sensing of Environment*. Elsevier, 225(September 2018), pp. 267–289. doi: 10.1016/j.rse.2019.03.018.

Wilson, G. W. and Fischetti, T. R. (2010) 'Coastline Population Trends in the United States : 1960 to 2008', *U. S. Census Bureau*.

ANNEX A 1

RESULTS OF S2-MSI SPM MATCH-UPS FOR THE TAGUS ESTUARY

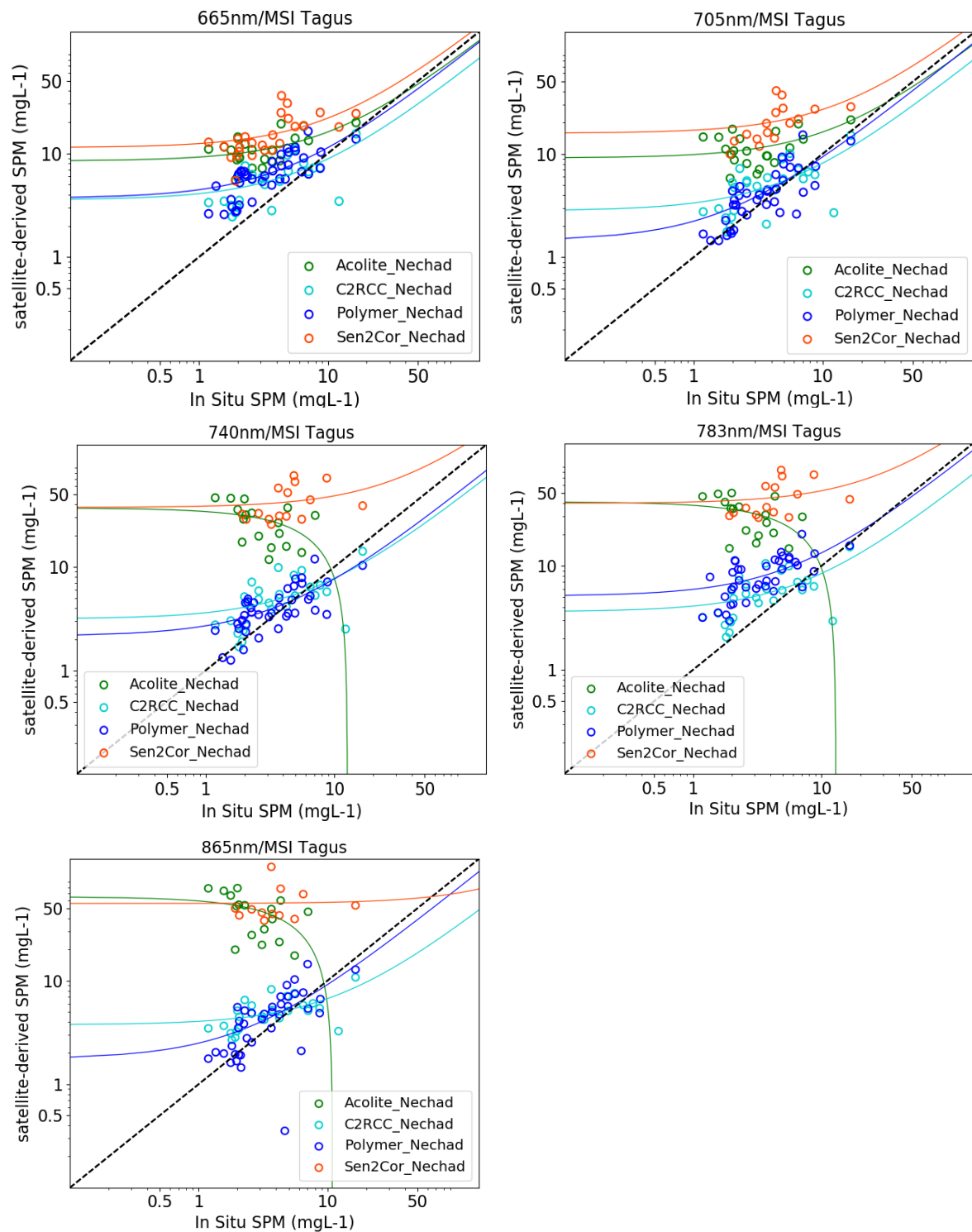


Figure A.1 - Comparison of in situ and S2-MSI-derived SPM estimates at different wavelengths from all the AC processors tested for the Tagus estuary. Data represent match-ups for the concurrent satellite and field measurements collected during several research projects. The dashed black lines show 1:1 relationship, the solid lines are the best linear fit to the data in log space.

Table A 1 - Summary of statistics for SPM S2-MSI match-ups from all AC processors tested results for the Tagus estuary. Numbers in bold show the best value of each statistics for all processors.

Processor	Algorithm	Wavelength (nm)	N	R ²	Slope	Intercept	stderr	RPD (%)	APD (%)	RMSE
Acolite	Nechad et al., 2010	665	21	0.413	0.765	8.441	0.209	305.45	305.45	8.15
	Nechad et al., 2010	705	21	0.309	0.713	9.116	0.244	340.61	340.60	8.79
	Nechad et al., 2010	740	21	0.156	-2.936	37.018	1.758	1222.94	1222.94	27.63
	Nechad et al., 2010	783	21	0.164	-3.195	41.289	1.859	1363.93	1363.92	31.08
	Nechad et al., 2010	865	21	0.201	-5.902	64.87	3.042	2127.69	2127.69	48.32
C2RCC	NN	-	26	0.284	1.0138	5.504	0.328	182.68	190.63	7.972
	Nechad et al., 2010	665	26	0.423	0.529	3.553	0.126	69.79	79.85	3.118
	Nechad et al., 2010	705	26	0.419	0.531	2.815	0.127	47.77	61.62	3.05
	Nechad et al., 2010	740	26	0.346	0.462	3.139	0.129	45.76	60.58	2.86
	Nechad et al., 2010	783	26	0.343	0.483	3.617	0.136	66.20	76.60	3.274
	Nechad et al., 2010	865	26	0.325	0.296	3.748	0.086	54.40	70.26	2.982
Polymer	Nechad et al., 2010	665	39	0.502	0.768	3.687	0.1265	96.66	99.04	3.608
	Nechad et al., 2010	705	39	0.539	0.790	1.441	0.1213	-75.31	75.31	4.275
	Nechad et al., 2010	740	39	0.482	0.551	2.143	0.0938	24.40	39.45	2.273
	Nechad et al., 2010	783	39	0.398	0.823	5.111	0.1676	51.91	52.91	5.329
	Nechad et al., 2010	865	39	0.475	0.741	1.750	0.1294	29.34	47.75	2.473
Sen2Cor	Nechad et al., 2010	665	16	0.257	1.053	11.362	0.373	367.69	367.69	13.16
	Nechad et al., 2010	705	16	0.185	1.105	15.821	0.619	392.89	392.89	18.15
	Nechad et al., 2010	740	16	0.053	1.100	37.387	1.283	935.50	935.50	41.22
	Nechad et al., 2010	783	16	0.063	1.285	39.822	1.374	1010.82	1010.82	44.79
	Nechad et al., 2010	865	16	0.000	0.141	55.761	2.001	1460.40	1460.40	56.98

ANNEX A2

RESULTS OF S2-MSI TURBIDITY MATCH-UPS FOR THE TAGUS ESTUARY

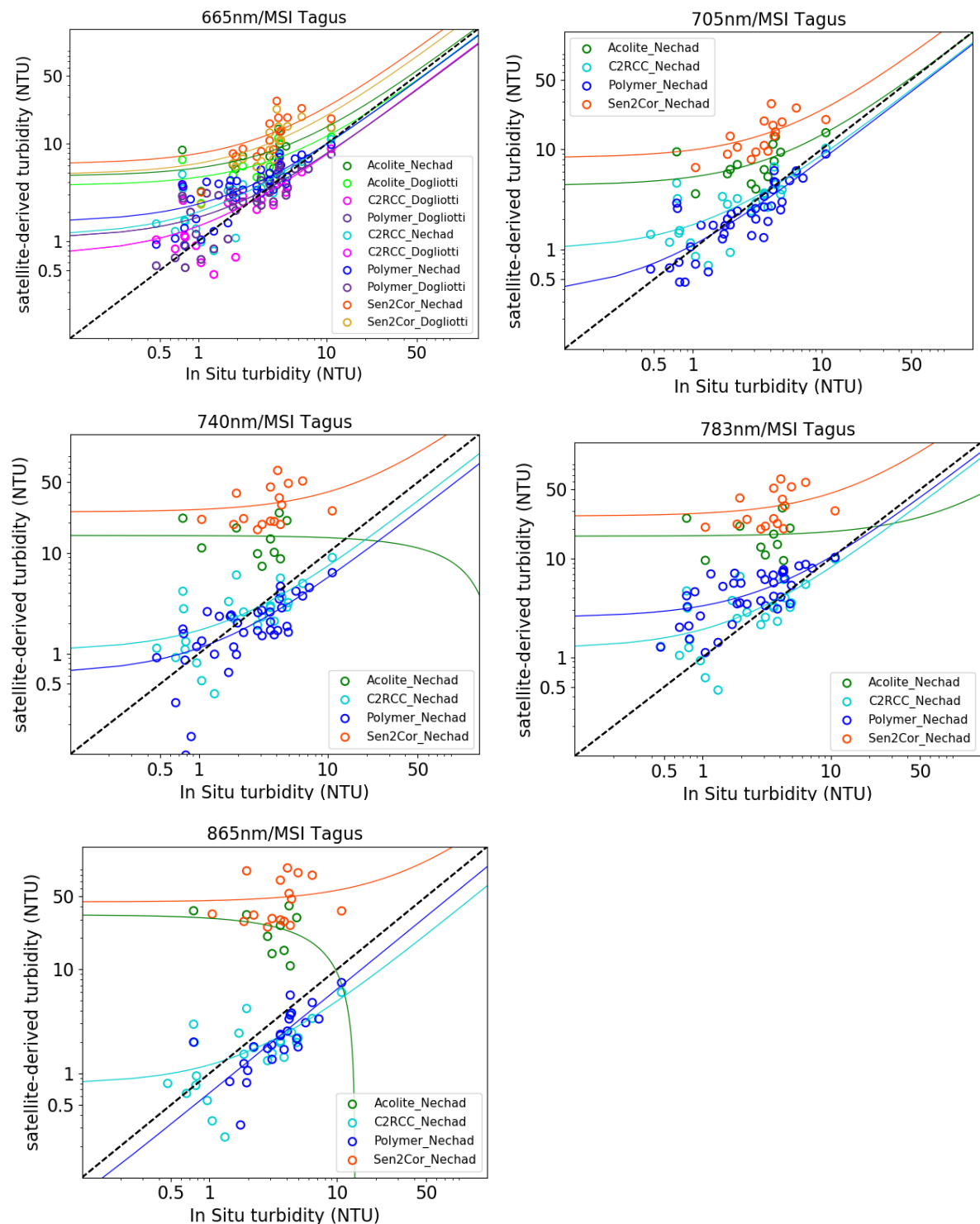


Figure A.2 - Comparison of in situ and S2-MSI-derived SPM estimates at different wavelengths from all the AC processors tested for the Tagus estuary. Data represent match-ups for the concurrent satellite and field measurements collected during several research projects. The dashed black lines show 1:1 relationship, the solid lines are the best linear fit to the data in log space.

Table A 2 - Summary of statistics for turbidity S2-MSI match-ups from all the AC processors for the Tagus estuary. Numbers in bold show the best value of each statistics for all processors.

Processor	Algorithm	Wavelength (nm)	N	R ²	Slope	Intercept	stdErr	RPD (%)	APD (%)	RMSE
Acolite	Dogliotti et al., 2015	665	17	0.461	0.826	3.705	0.307	579.51	579.51	7.80
	Nechad et al., 2009	665	17	0.480	1.025	4.629	0.307	334.80	334.80	4.28
	Nechad et al., 2009	705	17	0.203	0.582	6.369	0.264	422.34	422.34	5.76
	Nechad et al., 2009	740	17	0.253	- 2.623	24.199	1.163	1708.15	1708.15	18.53
	Nechad et al., 2009	783	17	0.217	- 2.691	27.425	1.319	1959.07	1959.07	21.63
	Nechad et al., 2009	865	17	0.082	- 2.406	33.240	3.041	1092.04	1092.04	24.49
C2RCC	Dogliotti et al., 2015	665	24	0.751	0.708	0.716	0.088	26.594	58.852	1.18
	Nechad et al., 2009	665	24	0.750	0.869	1.129	0.106	72.039	83.020	1.43
	Nechad et al., 2009	705	24	0.723	0.774	0.985	0.102	55.438	74.994	1.29
	Nechad et al., 2009	740	24	0.573	0.633	1.067	0.116	40.152	74.129	1.54
	Nechad et al., 2009	783	24	0.566	0.689	1.225	0.128	57.380	82.903	1.62
	Nechad et al., 2009	865	24	0.541	0.416	0.789	0.081	-1.950	60.650	1.85
Polymer	Dogliotti et al., 2015	665	38	0.717	0.689	1.067	0.072	27.662	47.895	1.170
	Nechad et al., 2009	665	38	0.717	0.846	1.558	0.088	71.424	47.096	1.643
	Nechad et al., 2009	705	38	0.766	0.751	0.346	0.069	0.935	24.023	12.073
	Nechad et al., 2009	740	38	0.666	0.505	0.627	0.059	-11.036	46.549	1.563
	Nechad et al., 2009	783	38	0.522	0.783	2.534	0.124	119.773	122.655	2.550
Sen2Cor	Dogliotti et al., 2015	665	16	0.367	1.474	4.813	0.516	368.13	368.14	7.27
	Nechad et al., 2009	665	16	0.371	1.778	6.168	0.618	489.13	489.13	9.67
	Nechad et al., 2009	705	16	0.334	1.656	8.220	0.624	318.64	318.64	12.04
	Nechad et al., 2009	740	16	0.051	1.468	25.383	1.694	850.43	850.43	30.58
	Nechad et al., 2009	783	16	0.079	1.886	26.860	1.716	932.52	932.52	33.51
	Nechad et al., 2009	865	16	0.014	1.302	44.235	2.951	1446.21	1446.21	51.46